Design of a Free Field Blast Simulating Shock Tube

by

Jonathan Armstrong

Thesis submitted to the
Faculty of Graduate and Postdoctoral Studies
In partial fulfillment of the requirements
For the M.A.Sc. degree in
Mechanical Engineering

Ottawa-Carleton Institute for Mechanical and Aerospatial Engineering
Faculty of Graduate and Post-doctoral Studies
University of Ottawa

Abstract

A 30.5 cm diameter, detonation driven shock tube facility has been designed, constructed and tested. The design goals of the shock tube were to reproduce free field blast wave profiles on a laboratory scale using atmospheric gaseous detonation as the energy source. Numerical simulations were utilized to explore the gas dynamic evolution inside detonation driven shock tubes and to select the optimal design parameters for the shock tube. The Friedlander profile was used to evaluate the generated pressure profiles as an approximation of free field blast waves. It has been found that the detonation driver length should be kept below 20% of the total length of the tube in order to produce Friedlander waves. Additionally, it has been found that an annular vent can be added to the shock tube to enhance the negative phase of the blast profile, more accurately reproducing real free field blast waves. The shock tube has been constructed in a modular fashion from 2.54 cm thick steel tubing. An adjustable bag type diaphragm has been employed to allow for a variable driver size and a high voltage ignition system is used to initiate detonation in the driver section. Due to the available location for the shock tube, tests using the vented configuration could not be accomplished for safety reasons. Conducted experiments produced results that agree well with corresponding numerical simulations. Overall, the shock tube design was successful in creating Friedlander blast waves. At the time of writing, a manufacturer error in correctly reporting the specifications of the clamps used on the shock tube resulted in a lower maximum pressure of operation.

Acknowledgements

I would like to thank my thesis supervisor, Matei Radulescu, for his guidance and friendship during my time at the University of Ottawa. I would also like to thank John Perrins and the staff of the Mechanical Engineering Department's machine shop, for their help and for mentoring me during the manufacturing of the shock tube. Finally, I would like to thank the members of the DRDL research group for their support and camaraderie, especially Logan Maley, without whom the completion of this thesis may not have been possible.

Contents

List of Tables

List of Figures

Nomenclature

Abbreviations

CEA	Chemical Equilibrium with Applications, a chemical equilibrium software package developed by NASA.
CFD	Computational fluid dynamics.
CJ	Chapman-Jouget, referring to the gas dynamic state behind a steady state detonation wave.
HLLE	Harten, Lax, Van-Leer and Einfeldt, a positivity preserving Riemann solver.
HVI	High Voltage Ignition, referring to the method of detonation initiation in the shock tube.
TNT	Trinitrotoluene; A chemical compound most notably used as an explosive. Generally regarded as the standard measure of explosive strength.

Physical Properties

ρ	Density, local value unless otherwise indicated by subscript.
$\frac{l}{r}$	The shock tube length normalised by its radius.
D	Detonation velocity.
d	Distance away from the blast center.
E	Sum of the internal and kinetic energies of the fluid.
f_d & f_t	Transmission coefficients for the blast scaling laws.

L_{driver}	The length of the driver section of the shock tube, expressed as a percentage of the overall tube length.
l_{vent}	Length of vent along in the shock tube, expressed as a percentage of the total tube length.
u	Velocity, local value unless otherwise indicated by subscript.
V	Specific volume.
v	Velocity in the y direction.
W_{TNT}	Equivalent weight of TNT charge needed to reproduce a blast wave.
x	Position along x axis.
x_{vent}	Starting position of a vent along the length of the shock tube, expressed as a percentage of the total tube length.

Subscripts

$[\ ]$	(No subscript) Local value.
$[\ ]_{CJ}$	Chapman-Jouget state.
$[\ ]_{Det}$	Detonation property.
$[\ ]_{eq}$	In the context of blast scaling laws, represents the blast wave property generated by the equivalent TNT charge.
$[\ ]_{o}$	Initial, unburned state.
$[\ ]_{pr}$	In the context of blast scaling laws, represents the blast wave property of the profile for which an equivalent charge mass will be found.
$[\ ]_{ref}$	In the context of blast scaling laws, represents the blast wave property generated by the reference TNT charge.

Chapter 1

Introduction

Typically, experimental blast wave studies require costly, large scale, free field testing. Shock waves can be generated on the laboratory scale with the use of shock tubes. However, the gas dynamic evolution of the flow generated by many shock tubes is not representative of free field blast waves, decreasing their usefulness in such studies. The focus of this work is the design and implementation of a shock tube facility capable of producing realistic blast wave profiles on a laboratory scale with a high degree of reproducibility.

The goal of this work has been to design a shock tube capable of withstanding atmospheric detonation pressures and is intended for testing blast interaction with objects with a length scale of 30 cm in diameter. The energy required for generating the blast waves is supplied by a reactive gas detonation driver. An expansion chamber is located at the downstream end of the shock tube to house the test object and to allow the expansion of the high pressure gasses.

1.1 Characteristics of a Blast Wave

Figure 1.1 shows the evolution of a typical free field blast. After ignition, the very high temperature and pressure explosion kernel (shown in frame *b*) of figure 1.1) expands violently. The interface between the expanding explosion products and the surrounding air is denoted by $\vec{c}$. This rapid expansion drives a primary shock wave, S_1, expanding out and away from the growing fireball, shown in frames *c*) through *e*). S_1 propagates, as the air moves away from the blast center. This rapid volumetric expansion causes

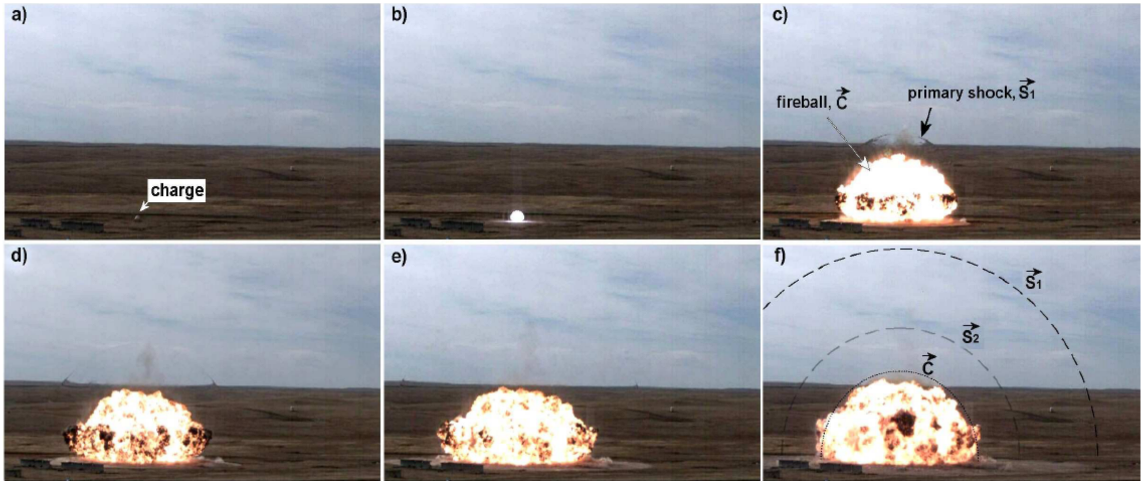

Figure 1.1: Example of a free field blast wave. *Image: Ritzel et. al. [2]*

the local pressure near the center of the blast to drop below ambient conditions. An inward facing recompression shock is formed and propagates toward the center of the blast recompressing the over-expanded gas. Ultimately this shock reaches the center of the blast and reflects outwards as the secondary shock, S_2 [1] . S_2 then begins to propagate outward, as the gas reaccelerates away from the center beginning anew the over-expansion-recompression cycle. This cycle continues until the recompression waves are not strong enough to form a shock and instead, gradually return the pressure to ambient conditions.

Figure 1.2 (a) shows the pressure-time history of a blast wave as measured by a stationary observer at a given distance from the blast. At the arrival of the primary shock (S_1) there is an instantaneous increase in pressure, immediately followed by rapid decay in pressure due to the volumetric expansion of the flow. The pressure continues to drop below ambient conditions and is eventually recompressed by the secondary shock wave (S_2). This cycle may repeat again, depending on the strength of the initial blast. Ultimately, shock waves are no longer observed and the pressure returns to atmospheric conditions.

The Friedlander profile, illustrated in figure 1.2 (b), is an idealized form of a blast wave pressure profile and neglects any auxiliary shocks. It was originally proposed by Friedlander in 1946 [3] and was more recently modified by Dewey [4] to accommodate a larger range of shock strengths, this form is shown in equation (1.1), where P_s is the shock

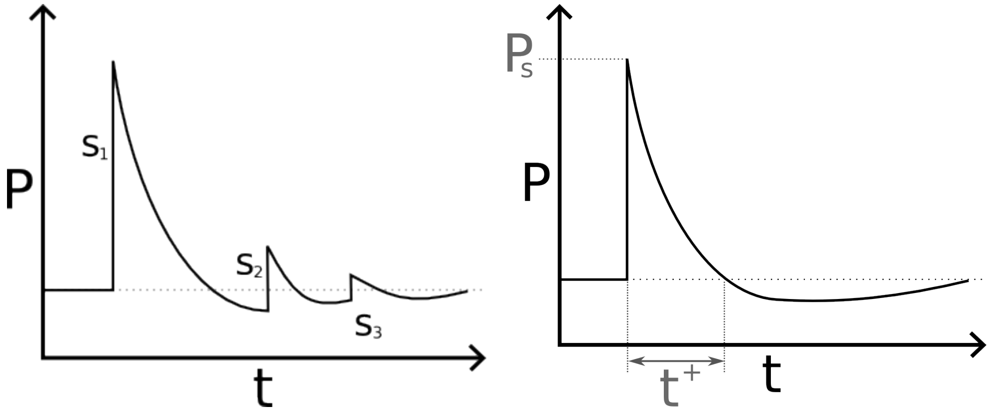

(a) (b)

Figure 1.2: (a) Illustration of a pressure profile of a passing blast wave, measured by a stationary observer. (b) Idealiazed Friedlander profile.

pressure, α is the expansion coefficient and t^+ is the positive pressure phase duration. The Friedlander equation is used in the context of this thesis as the target profile to be generated by the shock tube design discussed herein. The main characteristics of the Friedlander profile are the sharp rise in pressure at the arrival of the shock and the smooth, rapid expansion following it. The presence of these characteristics in the generated pressure profiles will indicate a successful shock tube design.

$$P(t) = P_s e^{-\alpha t}\left(1 - \frac{1}{t^+}\right) \tag{1.1}$$

1.2 Previous Work

All shock tubes operate on a common principle; a high pressure driver gas is isolated from the test gas by a diaphragm. Upon rupture of the diaphragm, the sudden expansion of the driver gas drives a compression shock wave into the test gas.

1.2.1 Compressed Gas Shock Tubes

In compressed gas shock tubes the driver section contains highly pressurized inert gas. When the diaphragm is ruptured, the high pressure in the driver section compresses the gas in the driven section, sustaining a shock wave. The large differential pressure between the driver and driven sections requires the use of robust diaphragms often made of metal. A double diaphragm system is often employed, where the space between the two diaphragms is held at an intermediate pressure, reducing the stress on each diaphragm. When this section is evacuated, the diaphragms are exposed to the full overpressure of the driver section, rupturing both and allowing the shock wave to propagate into the driven section. Note that, when ruptured, metal diaphragms can act as an obstacle to the flow and affect the propagation of the shock wave [5] [6].

Figure 1.3 illustrates the gas dynamic evolution in a compressed gas shock tube. As previously mentioned, the high and low pressure sections are initially separated by a diaphragm. Illustrated in column t_1 of figure 1.3 are the initial pressure, density and velocity profiles in the tube. When the diaphragm is ruptured, a shock wave is propagated into the driven section and, simultaneously, an expansion wave is propagated into the driver section, illustrated in column t_2. As the shock passes it compresses and accelerates the gas downstream in the tube. Likewise, the rarefaction also accelerates the gas toward the driven section. In the general case, a contact surface is present and convected downstream. The contact surface represents the interface between the expanded driver gas and the shocked driven gas. It is characterized by an interface across which velocity and pressure are uniform but density is discontinuous. A more complete description of the evolution of the flow in compressed gas shock tubes can be found in Thompson, 2008 [7].

Early examples of compressed gas driven blast simulating shock tubes have been implemented by Celander et. al. [8] and later, at the Lovelace Foundation for Medical Education and Research, by Richmond et. al. [9] [10]. However the pressure profiles generated by these tubes were characterized by long lived, flat topped positive pressure phases, as is shown in figure 1.5. More recent implementations of compressed gas shock tubes have succeeded in obtaining Friedlander-like profiles [11]. Additionally, techniques for controlling the expansion profile behind the shock have also recently been implemented. Holmberg [12] applied a variable opening on the down stream end of the shock tube, while Ritzel et. al. [2] and Kleinschmit [13] have implemented conically expanding sections in and directly after the driver section. Both of these approaches are similar in the fact that they add volumetric expansion to the flow. Figure 1.6 shows the pressure profiles generated by each approach, illustrating the similarity of their effects on the flow and their ability to produce Friedlander waves.

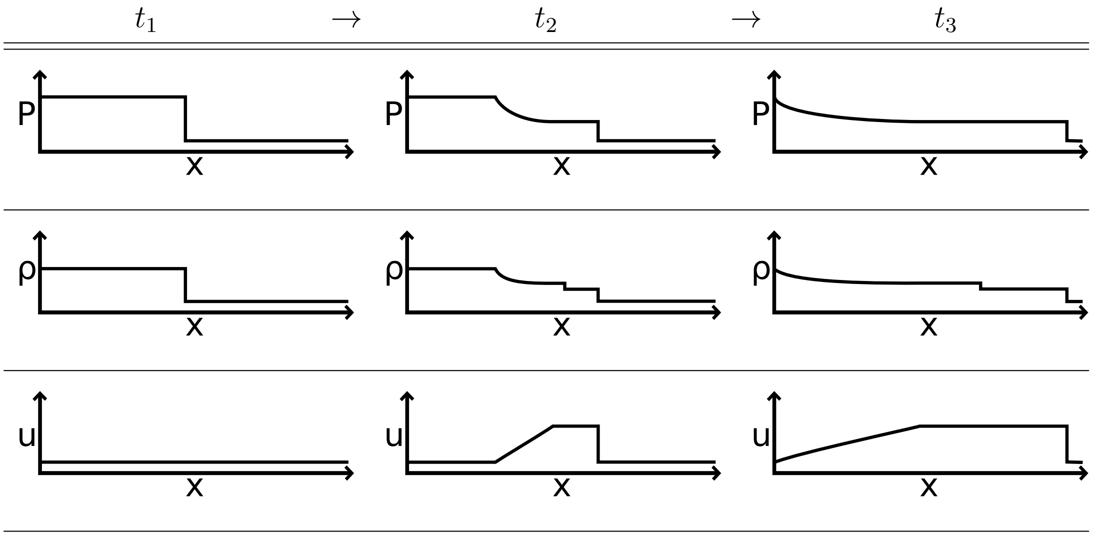

Figure 1.3: Illustration of the evolution of pressure, density and local velocity in a compressed gas shock tube at early times.

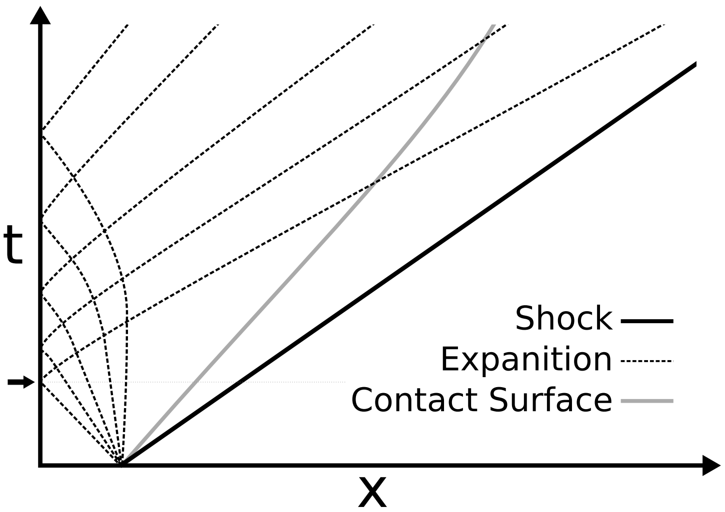

Figure 1.4: Space-time diagram of gas-dynamic evolution in a compressed gas shock tube, illustrating the behaviour of the detonation, resulting shock, expansion waves and contact surface. The arrow on the time axis indicates end of analytically solvable regime.

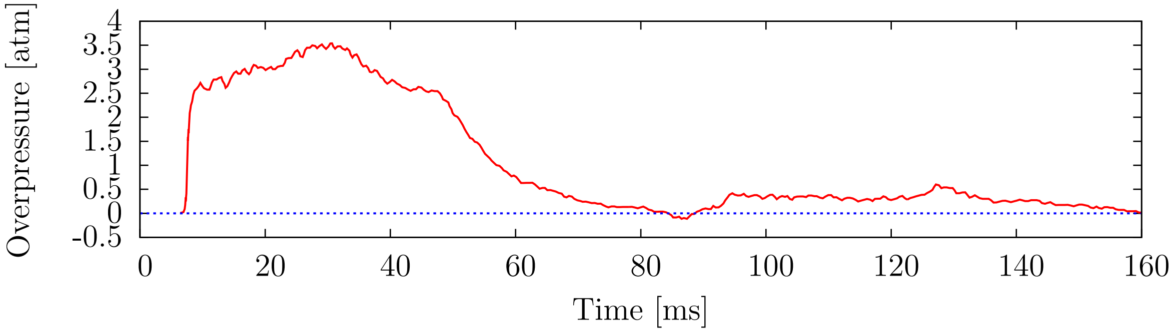

Figure 1.5: Pressure-time history generated by the Lovelace shock tube, illustrating a long lived, flat topped pressure profile. Reproduced from Richmond et. al. [9]

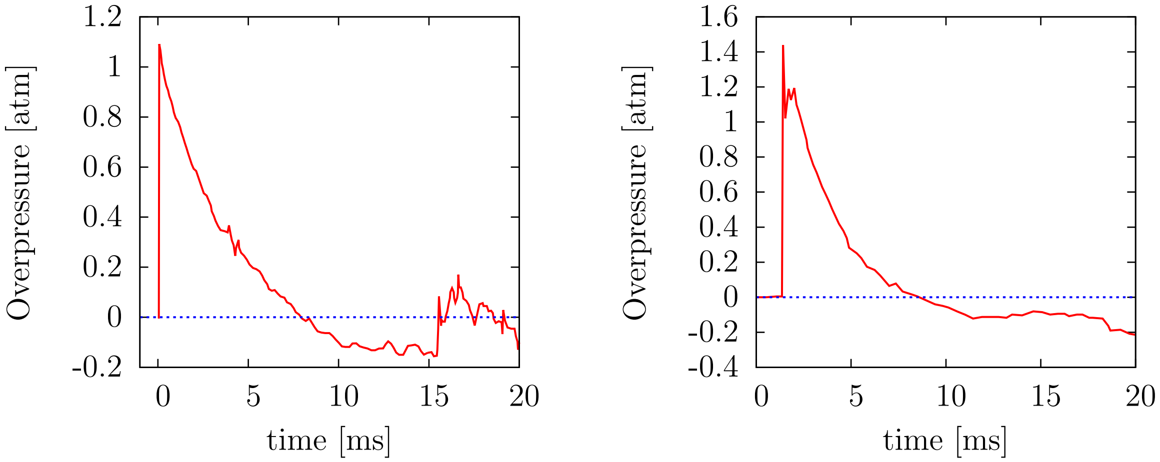

(a) **(b)**

Figure 1.6: (a) Pressure profile generated by shock tube with conically expanding sections, developed by Kleinschmit [13]. (b) Pressure profile generated by shock tube with modulated vent at downstream end of the tube, developed by Holmberg [12].

The *x*-*t* diagram of the general compressed gas shock tube is shown in figure 1.4. It illustrates how shortening the driver section allowed the examples mentioned above to obtain sharp expansion profiles after the shock. Due to the self similarity of the evolution, shortening the driver section reduces the distance the expansion wave must travel before reaching the leading shock, allowing for a sharp expansion profile. However, the shock pressures obtained by these shock tubes remain relatively low, on the order of 1 atm overpressure. Obtaining higher shock pressures at the exit plane of the tube would require very high driver pressures, rendering the compressed gas shock tube an infeasible solution for higher pressure blast studies.

1.2.2 Detonation Driven Shock Tubes

In detonation driven shock tubes, the driver portion of the tube is filled with a highly reactive gas mixture, typically a stoichiometric oxy-fuel mixture. An ignition source is used to ignite the gas and initiate a detonation in the driver section. Note that there is a minimum amount of energy required to directly initiate a detonation in the mixture, which is dependant on the composition of the gas mixture [14]. Alternatively, flame accelerating obstacles can be used to aid in the initiation of a detonation wave [15].

Typically, there is little or no differential pressure between the driver and driven sections in detonation shock tubes before ignition, allowing for the use of thin plastic diaphragms. Thin diaphragms have the advantage of offering no resistance to the passing of the shock wave, thus, not impeding flow in the tube.

Figure 1.7 illustrates the *x*-*t* diagram of the gas dynamic evolution of a detonation driven shock tube. At early times the detonation propagates through the driver section forming a Taylor expansion profile behind it [16]. As it reaches the interface between the combustible mixture and the inert gas (called the contact surface), the supporting chemical reactions are extinguished and an inert shock wave propagates through the tube. Similarly to the compressed gas shock tubes, detonation driven tubes are sensitive to the ratio of the driver and driven section lengths.

Early detonation driven blast simulation tubes made no effort to tailor the shape of the wave [17]. Since then, many gaseous detonation driven shock tubes have been developed with the ability to control the pressure-time evolution, though many of these

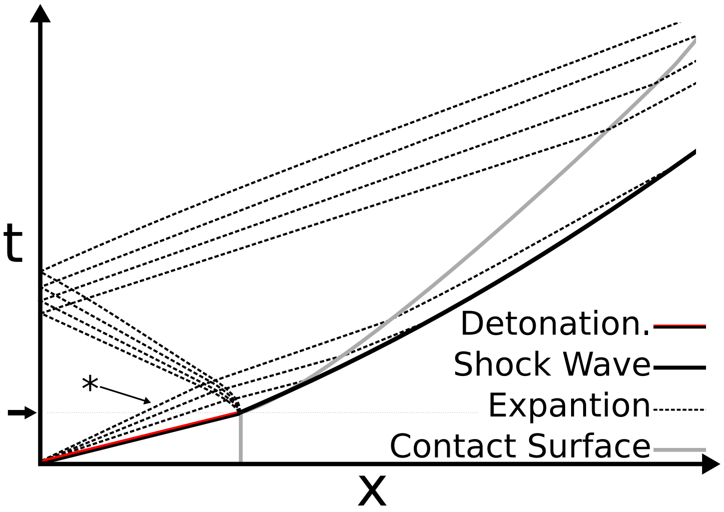

Figure 1.7: Space-time diagram of gas-dynamic evolution in a detonation driven shock tube, illustrating the behaviour of the detonation, shock wave, expansion waves and contact surface. The arrow on the time axis indicates end of analytically solvable regime. Taylor Expansion is labeled with an *.

were developed for hypersonic applications [18] [19] or chemical kinetic studies [20] [21]. Work has also been accomplished in the field of pulse detonation engines, focusing on the effect of the detonation driver size. Partially filled tubes have been investigated for their effects on the generated thrust [22] [23].

Much work has also been done in the past on blast simulating, detonation driven shock tube. Ohyagi et. al. studied the decay of the shock wave as it propagated through the tube [24]. Thibault et. al. have shown that the size of the driver section in proportion to the length of the shock tube can affect its ability to produce, near, mid and far field blast waves [25]. DRDC Suffield operates a large scale blast simulating shock tube with 1.8 m internal diameter [26]. This shock tube implements a conical driver section as well as a small driver to driven section length ratio, allowing it to produce free field blast waves on a very large scale.

1.3 Outline

Due to small driver lengths required to obtain Friedlander profiles, inert gas shock tubes require very high driver pressures. Thus, this thesis will present the design, construction and evaluation of a detonation driven shock tube. The solution provided herein consists of a shock tube, with a variable driver length, allowing for control over the produced pressure profiles. The tube is constructed in multiple segments allowing for the use of cylindrical vents along the length of the tube. The addition of vents to the shock tube will be explored, herein, as a means to further tailor the produced pressure profiles.

This solution will be presented with the following methodology; chapter 2 presents the numerical technique used to identify and evaluate the controlling design parameters. The results of the numerical investigation are presented in chapter 3 along with their effect on the design parameters. Chapter 4 presents the details of the mechanical design of the tube. Experimental results of the constructed shock tube are presented in chapter 5 and serve as the grounds for the evaluation of the design. Concluding remarks and recommendations for further development are presented in chapter 6.

Chapter 2

Numerical Technique

A numerical investigation has been conducted in order to examine the effects of the shock tube parameters on the generated wave profiles. By varying the controlling parameters of a detonation shock tube, their influence on the final wave profile has been investigated. These parameters have then been selected to most accurately replicate free field blast waves. This chapter will outline the numerical methods used to conduct this investigation.

2.1 Mathematical Model

2.1.1 Analytical Solution

Detonation driven shock tubes have a portion of their operation which can be described analytically. Namely, the portion of the evolution preceding the moment that the detonation arrives at the reactive/non-reactive gas interface, as illustrated in figure 1.7. To describe this evolution, the state immediately following the detonation must first be defined. The properties of this state, known as the Chapman-Jouget or CJ state, are computed with the Chemical Equilibrium with Applications software package (CEA) developed by NASA [27].

Once the detonation parameters have been found, the profile of a detonation propagating away from a boundary in an enclosed space can be described. Equations (2.1), (2.2) and (2.3) describe the evolution of the pressure, density and velocity in the flow behind a detonation propagating away from a wall in one dimension in the non-uniform region.

These equation can obtained from the characteristic form of the Euler equations [16]. Once the velocity of the gas falls to zero, the pressure and density also stay constant.

Note that in equations (2.1)-(2.3), variables are normalized by their initial conditions, in the region of unburned gas ahead of the detonation wave. Equations (2.1)-(2.3) are plotted in figure 2.1, using CJ detonation properties of a stoichiometric oxy-acetylene mixture. In equations (2.1)-(2.3), ρ is the density, P is the pressure, u is the velocity, x is the position, C is the sound speed, D is the detonation velocity and γ is the ratio of specific heats. Variables with no subscript are the local values, those with a subscript $_o$ represent the initial unburned state and those with the subscript $_{CJ}$ represent the Chapman-Jouget state values. The special case of x_{Det} refers to the current position of the detonation measured from the end wall.

$$\frac{P}{P_o} = \frac{P_{CJ}}{P_o}\left(\frac{\gamma-1}{\gamma+1}\cdot\frac{D_{CJ}}{C_{CJ}}\cdot\left[\frac{x}{x_{Det}}-1\right]+1\right)^{\frac{2\gamma}{\gamma-1}} \tag{2.1}$$

$$\frac{\rho}{\rho_o} = \frac{\rho_{CJ}}{\rho_o}\left(\frac{\gamma-1}{\gamma+1}\cdot\frac{D_{CJ}}{C_{CJ}}\cdot\left[\frac{x}{x_{Det}}-1\right]+1\right)^{\frac{2}{\gamma-1}} \tag{2.2}$$

$$\frac{u}{\sqrt{\frac{P_o}{\rho_o}}} = \frac{C_{CJ}}{C_o}\sqrt{\gamma}\left(\frac{1}{\gamma+1}\cdot\frac{D_{CJ}}{C_{CJ}}\cdot\left[2\frac{x}{x_{Det}}+(\gamma-1)\right]-1\right) \tag{2.3}$$

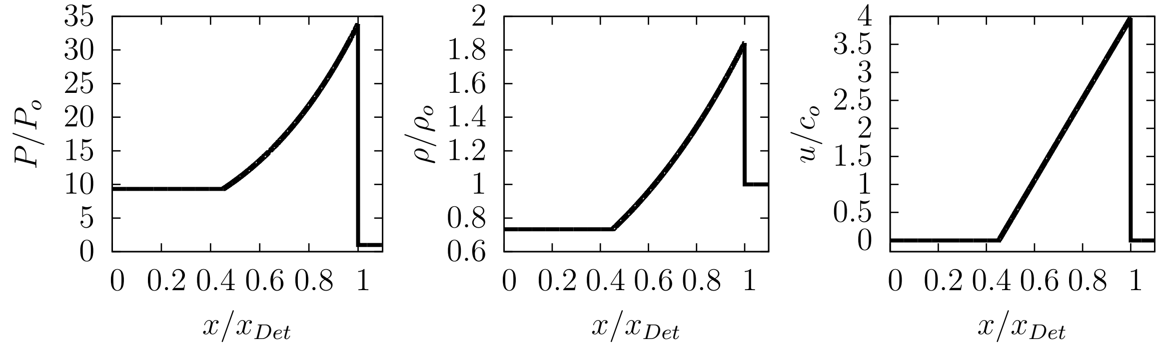

(a) **(b)** **(c)**

Figure 2.1: Profiles of a Taylor expansion wave formed behind detonation propagating away from a wall in a closed volume. Profiles show the evolution of (a) the pressure, (b) the density and (c) the gas velocity, normalized by initial conditions.

2.1.2 Governing Equations

The governing equations of the numerical model are taken to be the non-reactive, two dimensional Euler equations for an axis-symmetric domain, as shown in equations (2.4)-(2.7). All gases in the model are assumed to be calorically perfect. Additionally it is assumed that the ratio of specific heats, remains constant and equal to the detonation product's value, across the entire domain. Note that in equation 2.4, y is a radial coordinate representing the distance away from the axis of symmetry at $y = 0$. Additionally, v represents the flow velocity in the y direction and E is the sum of the internal and kinetic energies of the fluid.

$$\frac{\partial \vec{W}}{\partial t} + \frac{\partial \vec{F}}{\partial x} + \frac{1}{y}\frac{\partial (y\vec{G})}{\partial y} = 0 \tag{2.4}$$

$$\vec{W} = \begin{pmatrix} \rho \\ \rho u \\ \rho v \\ E \end{pmatrix} \tag{2.5}$$

$$\vec{F} = \begin{pmatrix} \rho u \\ \rho u^2 + p \\ \rho u v \\ (E + p)u \end{pmatrix} \tag{2.6}$$

$$\vec{G} = \begin{pmatrix} \rho v \\ \rho v u \\ \rho v^2 + p \\ (E + p)v \end{pmatrix} \tag{2.7}$$

2.1.3 Initial and Boundary Conditions

The initial conditions for the mathematical model of the shock tube are taken to be the instant at which the detonation reaches the driver/driven section interface and the supporting chemical reactions are quenched. The benefits of these initial conditions are two fold. Firstly, they allow the implementation of the analytical solution of Taylor expansion profile, thus removing a source of numerical error. Secondly, they avoid the use of computationally costly reactive gas dynamic simulations. The profiles shown in figure 1.3 are imposed on the domain such that the shock is located at the end of the

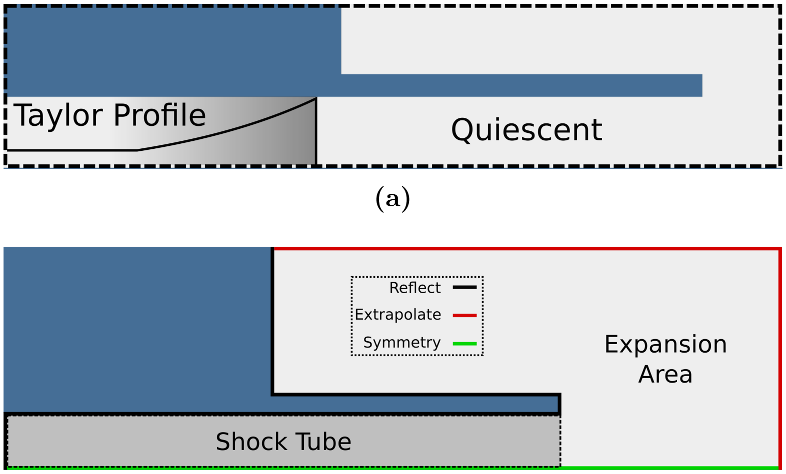

(a)

(b)

Figure 2.2: (a) Illustration of the initial conditions of the numerical model. (b) Illustration of the shape of the computational domain and the boundary conditions of the model.

driver section and the expansion wave extends to the back wall, as illustrated in figure 2.2 (a).

Figure 2.2 (b) shows the computational domain along with the boundary conditions of the model. Due to the axisymmetric nature of the problem, the computational domain represents a radial slice of the physical geometry, with the axis of symmetry located at the bottom boundary. The solid surfaces in the model, such as the shock tube walls, are imposed with a *Reflect* condition, representing a frictionless boundary which the flow cannot cross. Note that the axis of symmetry is also treated as a reflect condition. The *Extrapolate* condition is imposed on the upper and right boundaries. This allows any outward directed momentum to exit the domain. It should also be noted that the expansion area has been shortened on the left side of figures 2.2 (a) and (b). This is solely for reducing the computational requirements of the calculations.

2.2 Numerical Implementation

Numerical calculations have been accomplished using the AMRITA CFD environment, developed by J. J. Quirk [28]. The governing equations have been integrated using a Harten, Lax, Van-Leer and Einfeldt (HLLE) solver. This solver was chosen for its

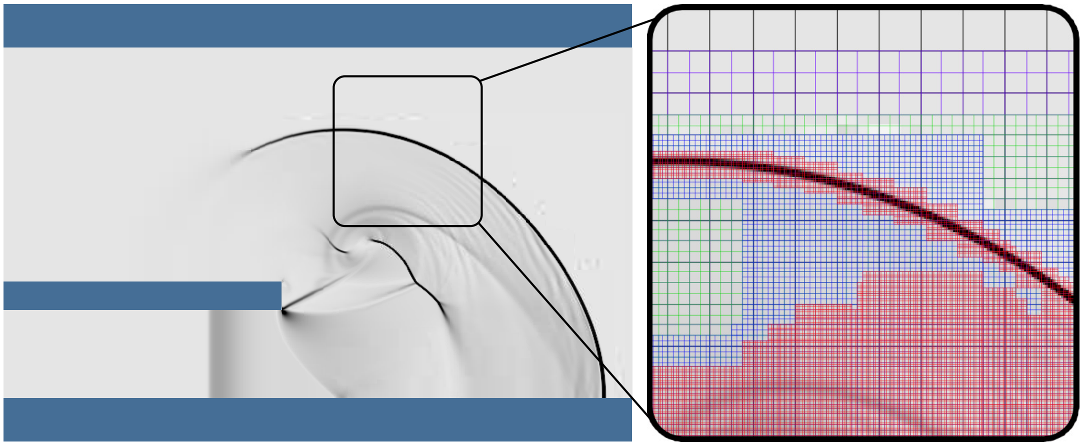

Figure 2.3: [left] Density gradient plot showing the shock wave expanding from the exit of the tube and [right] the resulting mesh, illustrating the adaptive mesh refinement employed by AMRITA.

positivity preserving characteristics, needed due to the strong expansion around the corner of the shock tube exit.

AMRITA employs an adaptive mesh refinement technique in order to sufficiently resolve shock waves and maintain efficient computer memory usage. As illustrated in figure 2.3, the computational grid is refined in and around areas of high density gradients, such as the shock waves and to a lesser extent the region of rapid expansion behind them. Note that the area of highest grid density slightly extends around the shock wave. This ensures that the shock is always propagating into the most highly resolved grid. Domain boundaries in AMRITA are treated with the ghost cell technique [28].

Ghost cells are a extra row of computational cells added to the outside of the domain. These cells always have the same momentum along the direction of the boundary as its neighbouring cell in the domain, while the momentum normal to the boundary in the ghost cell is dependant on the boundary condition imposed on that cell. If a boundary is assigned the *Reflect* condition the momentum perpendicular to the boundary in the ghost cell is equal and opposite to that of its neighbour in the domain. Thus, emulating a solid surface. *Extrapolate* boundary ghost cells are assigned momentum that is equal in magnitude and direction to that of the adjacent domain cell. This allows the flow to exit the domain unimpeded. These two conditions are illustrated in figure 2.4

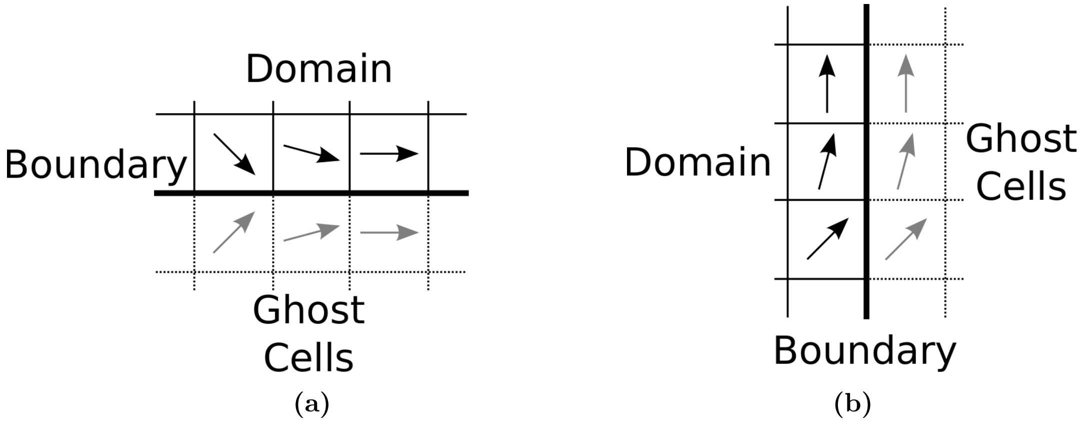

Figure 2.4: Illustration of the ghost cell technique for (a) *Reflect* and (b) *Extrapolate* type boundaries.

2.2.1 Verification and Validation

A grid convergence study has been conducted to verify the numerical framework implemented in this work. For the grid convergence study, the problem of a partially filled detonation tube was examined. The Taylor expansion profile was imposed on the upstream portion of the tube, representing a 20% driver length. The system was allowed to evolve in time and the shock pressure was recorded as it propagated down the tube. This simulation was repeated, varying only the maximum refinement level. Figure 2.5 shows the compiled results of these simulations. Given that the characteristic length scale of the problem is the shock tube radius, the maximum refinement level, n_{max}, is reported as the number of grid cells required to span the radius of the shock tube, at their most refined level.

As is shown in figure 2.5 the maximum refinement level affects not only the value of the shock pressure, but also the shape of the profile it produces as it propagates through the tube. At very low resolutions the shock profile is jagged and uneven; additionally the strength of the shock is significantly underestimated. As the resolution is increased, the shock pressure values begin to converge and the profile becomes smooth. Continuing to increase domain resolution results in no significant change of the recorded shock pressure. Thus, the optimal maximum refinement level is of 96 refined grid cells per tube radius. However, above a resolution of 96 resolved cells per tube radius the profile again begins to oscillate, without any significant change in the average shock pressure

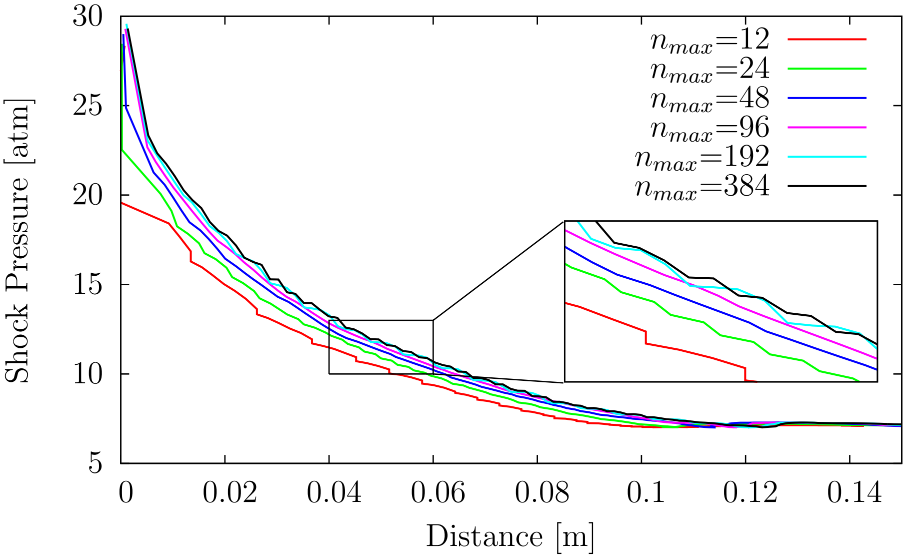

Figure 2.5: Results of numerical verification study; evolution of the shock pressure as it travels down the shock tube for different maximum grid refinement levels. n_{max} indicates the number of most-refined grid cells per tube radius.

values. At these higher refinement levels the start-up errors continue to be resolved due to the adaptive mesh refinement causing the oscillations in the pressure profile. Thus the optimal maximum refinement level is of 96 refined grid cells per tube radius.

In order to validate the computational model, experimental results obtained by Sochet [29] and later by Kato et. al. [30] were compared to numerical results calculated using the current numerical framework. In the experimental studies, an open-ended shock tube was filled with a reactive mixture and ignited. The resulting detonation wave propagated through the tube, ultimately driving a shock wave into the air surrounding the exit of the tube. The strength of this shock wave was measured as a function of distance from the tube's exit. An illustration of experimental apparatus implemented by Kato et. al. is shown in figure 2.6.

The experimental conditions have been recreated numerically using the model described above. The shock tube used in the recreated experiments had a diameter of 27 mm and a length of 1200 mm. The tube was entirely filled with a stoichiometric mixture of ethylene-oxygen at atmospheric temperatures and pressures. The shock wave was allowed to expand into the ambient air of the room. The shock pressure was measured

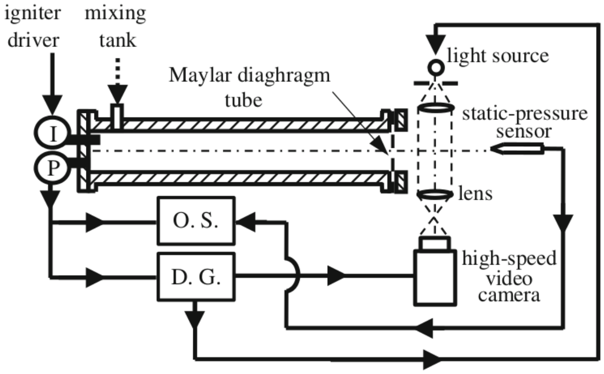

Figure 2.6: Experimental setup implemented by Kato et. al. for the measurement of shock pressures vs. distance generated by detonation tubes. (Figure reproduced from Kato et. al. [30].)

over a wide range of distances from the exit plane of the tube. Since test subjects that will be used with the shock tube designed in this thesis will be placed very close to the exit of the tube, the model has been validated using Kato's measurements up to 0.5 m away from the exit of the tube.

Figure 2.7 shows the comparison between the numerical results and the experimental data taken from Sochet et. al. [29] and Kato et. al. [30]. The numerical results agree well with experiment. However, as the shock propagates further away from the end of the shock tube, the model begins to slightly over-predict its strength. This is due to the constant γ approximation used in the model. A gas with a lower value of γ is more easily compressed, thus imposing the lower, burnt gas value of γ over the entire domain provides less resistance to the propagation of the shock wave. Note that varying the value of γ does not affect the results, since compressibility of the gas is the same everywhere due to the constant γ assumption. Despite this effect, the simulations agree with the experimental results sufficiently for the purposes of selecting the shock tube parameters.

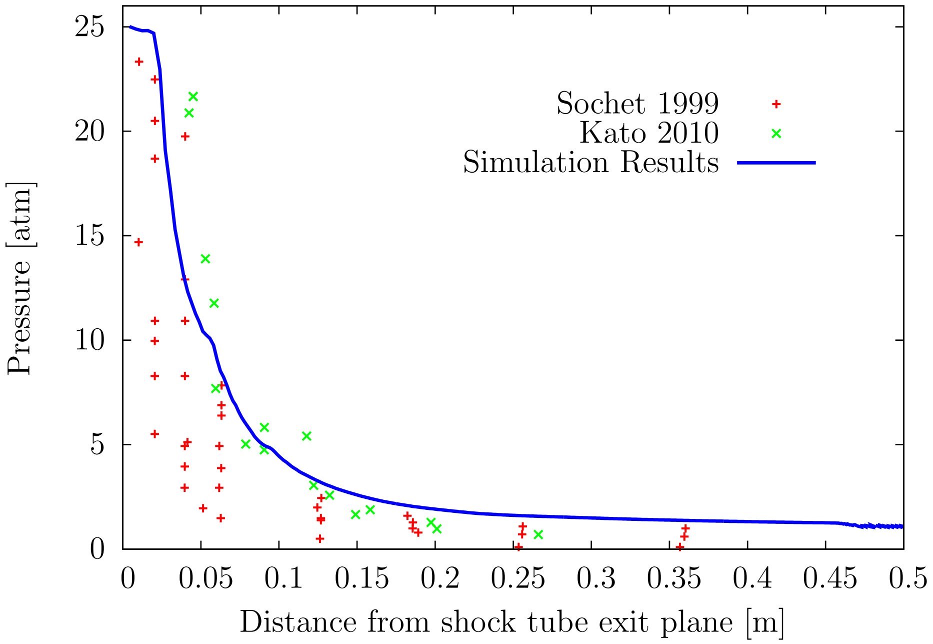

Figure 2.7: Results of validation study. Results from numerical recreations of studies conducted by Kato et. al. [30] and Sochet et. al. [29] plotted against experimental results obtained by these studies.

Chapter 3

Numerical Results

As mentioned in the previous chapter, a series of numerical simulations have been conducted for varying shock tube parameters. This way, the most important shock tube parameters are identified and their effects are observed. All numerical simulations have been conducted with a computational domain as illustrated in figure 3.1, where the length of the domain is varied to evaluate different shock tube configurations. An expansion area, four tube diameters in width and height, is added to the domain at the exit of the tube in addition to the expansion area above the shock tube spanning half of its length. The gas dynamic detonation parameters of a stoichiometric ethylene-oxygen mixture, as calculated with C.E.A., were used for the initial conditions. All simulations were conducted with a maximum mesh refinement level of 96 refined grid cells per tube radius, as described in the previous chapter.

There are three parameters that must be defined for any given shock tube configuration: the shock tube radius, the shock tube length and the length of the driver section. The number of independent variables can be reduced by normalizing the shock tube length by its radius, expressed $\frac{l}{r}$. Given that the evolution of a detonation driven shock tube is self similar in $\frac{x}{t}$, it is beneficial to express the length of the driver section (L_{driver}) as a percentage of the overall tube length. This allows the effect of the driver section length to be better isolated.

In every simulation, the pressure history has been recorded along the inside of the shock tube wall at intervals of two tube radii. These results will later be used in comparison with experimental results. Figure 3.1 indicates the location of these probes with a series of black dots along the top wall of the tube (note that the number of these sensors will

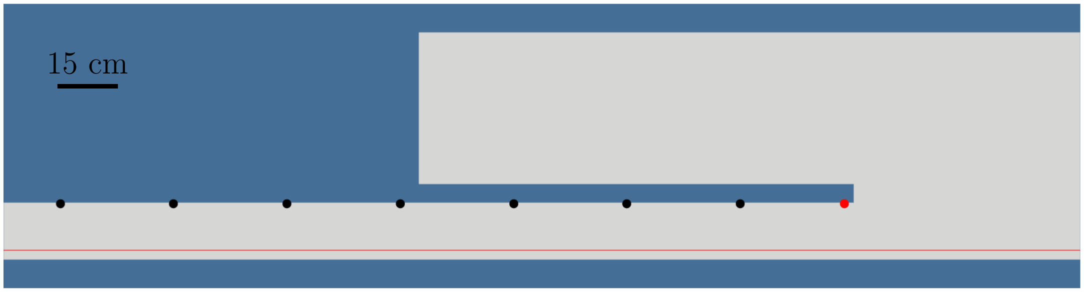

Figure 3.1: Geometry of the computational domain, also illustrating the locations where data was extracted from the numerical simulations.

change with the length of the tube). The red dot in figure 3.1, near the exit of the tube, indicates the location of an additional probe point to obtain the pressure history at the exit of the tube. The evolution of the pressure profile 1 grid cell above the axis of symmetry is also recorded as it changes in time; this is indicated by the red line in figure 3.1. Additionally the position and strength of the leading shock wave is monitored as it propagates through the tube. Schlieren images[1] are also produced, allowing more insight into the behaviour of the flow.

3.1 Case Study

In order to gain an understanding of the evolution of the flow inside the detonation shock tube, a sample case will first be analysed in detail. For this case the shock tube parameters are of a length to radius ratio of $\frac{l}{r} = 15$ and a driver section spanning 50% of the total tube length. As discussed in chapter 2, the Taylor wave profile is imposed spanning the length of the driver section and the system is allowed to evolve.

Figure 3.2 shows the pressure-time history recorded one base grid point in from the exit of the tube on the top wall (indicated by the red dot in figure 3.1). The pressure profile produced by this shock tube configuration has some aspects of a Friedlander profile, such as a sharp pressure rise at the arrival of the shock wave and a slower decline in pressure following the shock. However, the expansion profile following the shock has a stepped profile with three distinct expansion steps, highlighted by the labels *1, *2 and *3 in figure 3.2.

---

[1] Schlieren images show the distribution of the second derivative of density. Dark, sharp lines indicate large density gradients such as shock waves.[31]

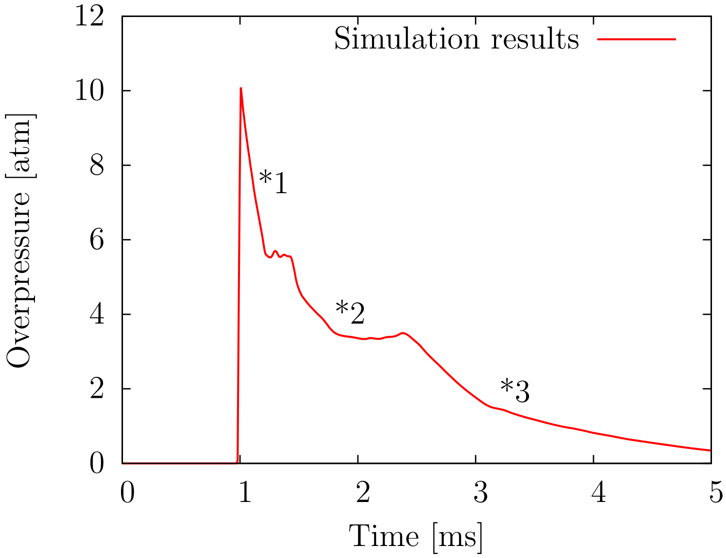

Figure 3.2: Pressure profile recorded at the exit of the tube on the inside of the shock tube wall. $\frac{l}{r} = 15$, $L_{driver} = 50\%$

In order to produce a smoother profile, the source of the expansion 'steps' must be determined. The center-line pressure profiles, shown in figures 3.3 and 3.4, more clearly show the behaviour of the different expansion waves in the system when examined along side the corresponding Schlieren images, shown in figure 3.5. Note that while the shock waves and contact surfaces are clearly visible on the Schlieren images, expansion waves are not, with the exception of the strong expansion wave formed as the shock initially expands around the exit of the tube. Also note the in the graphs of figures 3.3 and 3.4 the vertical dotted line represents the location of the exit plane of the shock tube.

Following the progression of figures 3.3, 3.4 and 3.5, the evolution of the gas dynamic profile in the shock tube can be reconstructed. The arrows in the graphs of figures 3.3 and 3.4 indicate the direction of propagation of the expansion waves in the domain. For instance, in frame (b) of figure 3.3 there are two expansion waves present. The first is attached to the leading shock, attenuating it as it propagates and the second is a rear-facing wave, propagating into the the detonation products of the driver section.

Inspection of figures 3.3 and 3.4 reveals that the first expansion step, labelled *1 in figure 3.2, is the remnant of the original Taylor expansion following the shock as it crosses the exit plane of the shock tube, shown in frame (c) of figure 3.3. A short plateau in pressure is quickly followed by a strong expansion appearing in frame (a) of figure 3.4, caused by the divergence of the flow around the exit of the tube. Note that the arrival of this wave on the center-line profiles is slightly later than its arrival in the profile of figure 3.2. This is due to the angle formed by the expansion as it crosses the width of the tube, illustrated in frame d) of figure 3.5. This second expansion continues to propagate inward until the pressure drop is accelerated by a third expansion wave that has finally reached the exit plane of the tube having reflected off of the back wall. Finally the pressure in the tube is gradually reduced as the remainder of the pressurized gas exits the tube.

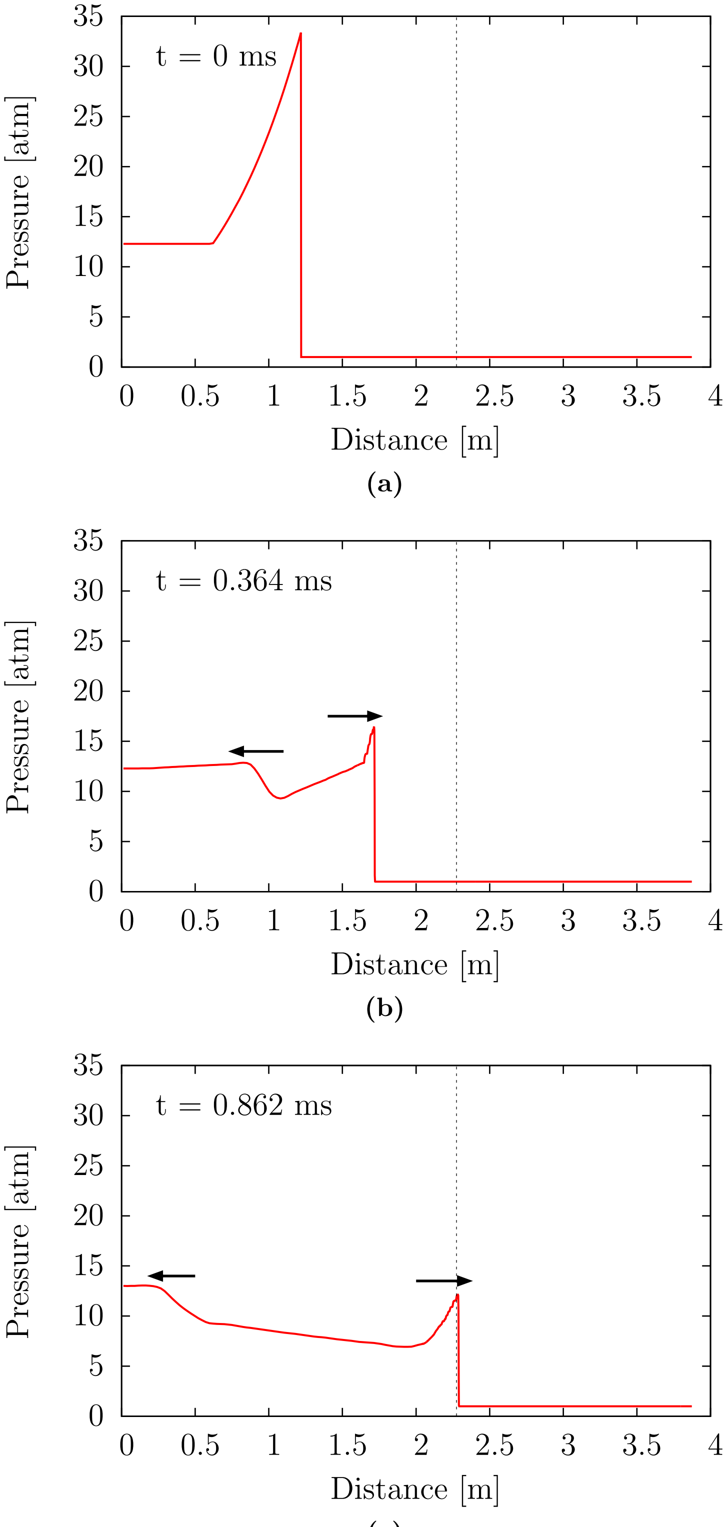

(a)

(b)

(c)

Figure 3.3: Evolution of the centreline pressure profiles with $\frac{l}{r} = 15$ and $L_{driver} = 50\%$.

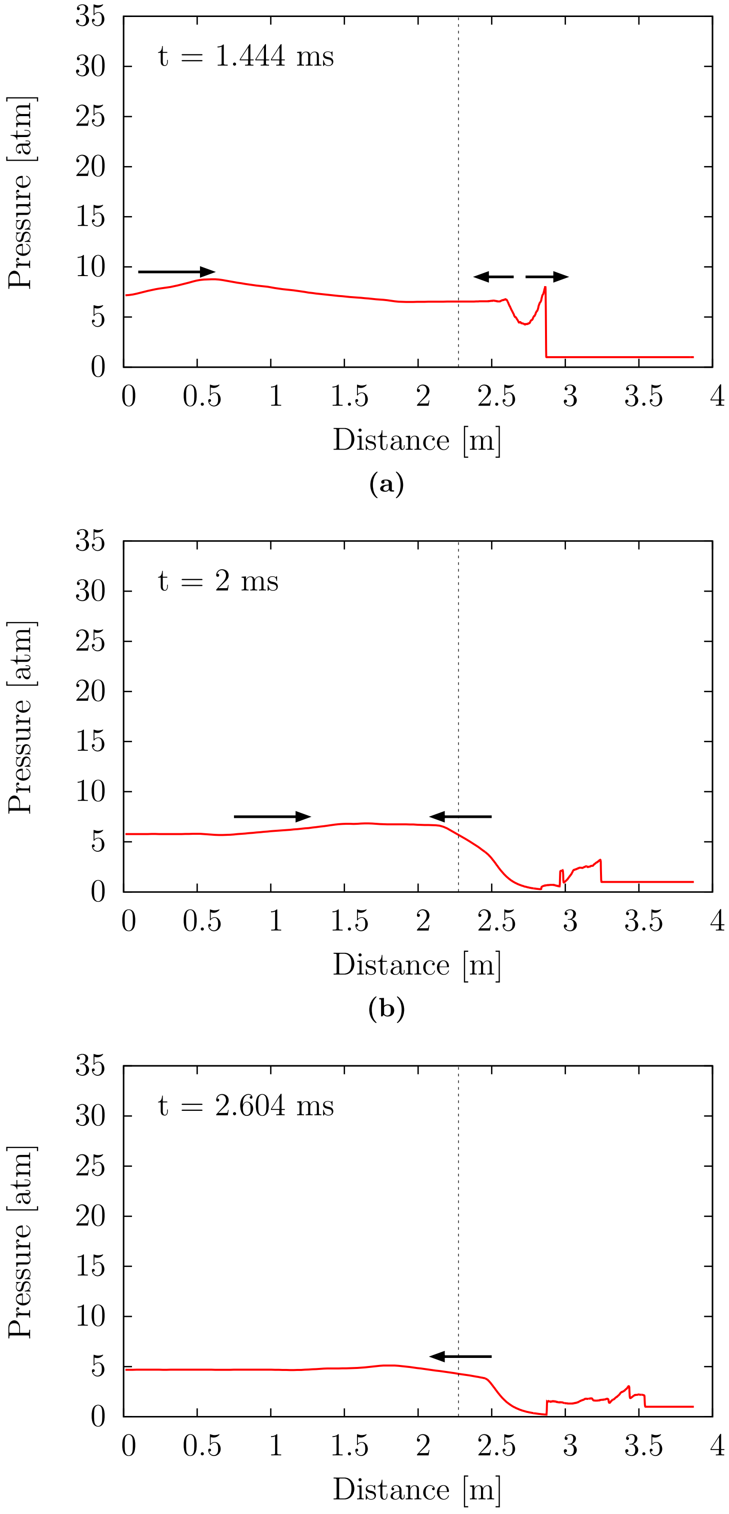

(a)

(b)

(c)

Figure 3.4: Evolution of the centreline pressure profiles with $\frac{l}{r} = 15$ and $L_{driver} = 50\%$. (Continued.)

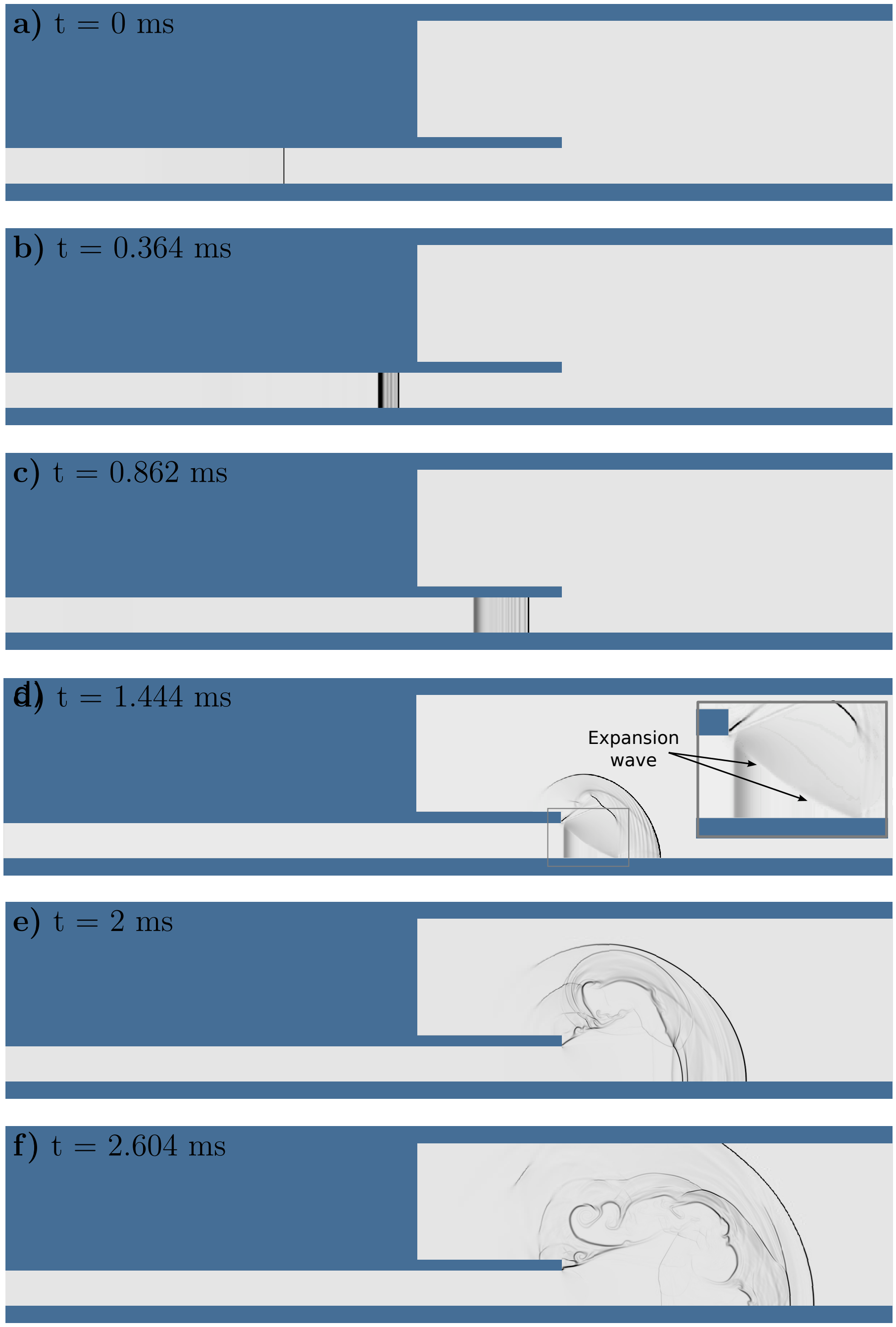

Figure 3.5: Schlieren images illustrating the evolution of the flow in the shock tube. Frame times correspond to those in figure 3.3 and 3.4.

3.2 Obtaining a Friedlander Wave

In essence, the stepped expansion profile is formed because the expansion waves in the system arrive at the exit of the shock tube at different times. Thus, the rear facing expansion wave must be given sufficient time to reach the leading shock. Shortening the length of the driver section, shortens the distance the wave must travel through the driver section before it can reflect and ultimately reach the shock.

Figure 3.6 illustrates the effect of shortening the driver section. Frame (a) shows again the profile for a shock tube fill percentage of 50%, with the stepped expansion profile. When the driver length is dropped to 40% of the tube length, in frame (b), the steps in the expansion profile are closer to the shock and have almost coalesced into one wave. While the profile produced for a fill percentage of 30% produces a smooth expansion profile, the expansion waves have not yet reached the shock, leaving a small plateau in pressure. Finally at a fill percentage of 20% the expansion immediately follows the shock and has a smooth profile. Thus, the shock tube fill percentage must be kept below 20% in order to obtain a smooth expansion profile following the shock.

3.2.1 The Negative Phase

The profile shown in figure 3.6 (d) can be considered as a Friedlander profile. However, no negative phase is present in the profile. In free field blasts, the negative phase is driven by the hemispherically expanding nature of the flow. The rapid increase in volume drives the flow to over expand, dropping the pressure below ambient conditions. As mentioned in the introduction, previous blast simulating shock tube designs have incorporated conically expanding sections to produce negative phases. In this study, the application of annular vents to the shock tube to add volumetric expansion has been investigated. The vents allow for volumetric expansion to occur, while maintaining a simple and flexible mechanical design.

The effect of these vents have also been investigated numerically. Due to the axis-symmetric nature of the computations, annular vents were represented by removing a portion of the top wall, illustrated in figure 3.7. A large number of simulations were conducted to determine the optimal size and location of the vent in order to maintain a Friedlander profile while also producing a negative phase. The parameters that were

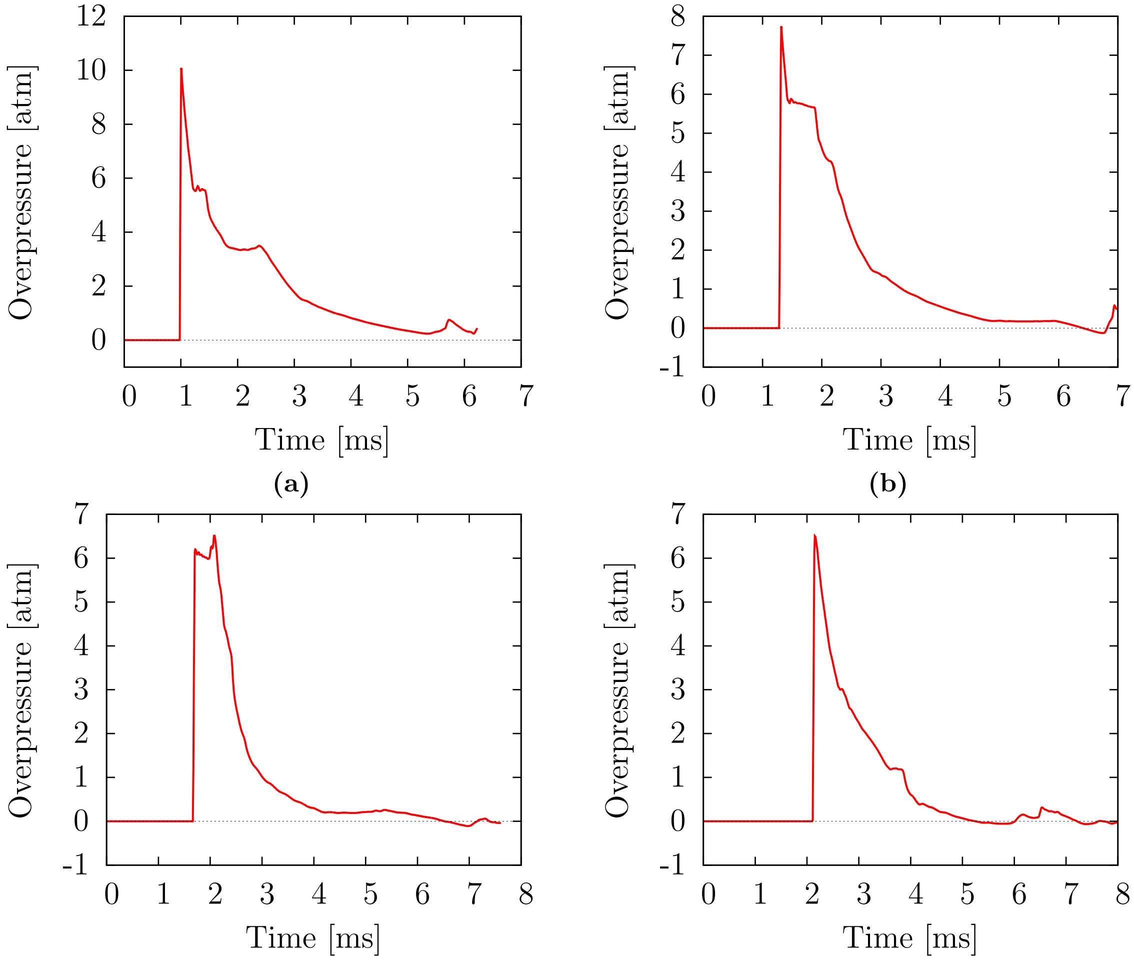

(a) **(b)**

(c) **(d)**

Figure 3.6: Pressure-time history at the exit of the shock tube for different fill percentages. Fill percentages are (a) 50%, (b) 40%, (c) 30% and (d) 20%.

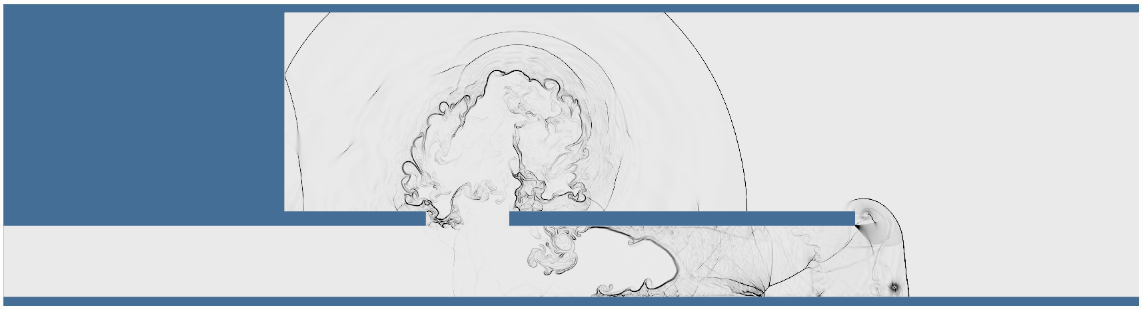

Figure 3.7: Schlieren image from a simulation with the addition of a vent.

varied for the configuration of the vent were the vent length (l_{vent}) expressed as a percentage of the total tube length, and its location along the length of the tube (x_{vent}), also expressed as a percentage of its total length.

Figure 3.8 shows pressure profiles produced by shock tube configurations with different vent geometries, where frame (a) shows the profile created by a shock tube with no vent for comparison. Also included in the graphs of figure 3.8 are the Friedlander curves fitted to each profile, using a least squares fit. These configurations are successful in adding a negative phase while maintaining a Friedlander profile. It has been found that increasing the distance of the vent away from the upstream end of the tube decreases the magnitude of the negative phase produced, illustrated by frames (b) and (c) of figure 3.8. This is due to the decrease in pressure of the shock as it propagates, the weaker pressures lead to weaker expansions into the ambient air. The magnitude of the negative phase has also been observed to be sensitive to the size of the vent. Comparing frames (c) and (d) of figure 3.8, for example, shows that decreasing the vent size from 10% to 5% of the shock tube length also reduces the amplitude of the negative phase.

There are limitations, however, on the extent to which the vent geometry can be modified. Figure 3.9 shows the pressure profiles produced by two unsuccessful vent configurations. Increasing the vent size beyond 15% of the total tube length, for example, leads to significant disturbances to the pressure profile as shown in 3.9 (a). This is caused by the curvature of the shock wave, driven by the expansion of the flow, affecting a larger portion of the shock front that remains in the tube as it strikes the end of the vent, shown in figure 3.10. This increased penetration of the curvature into the shock tube causes a longer lasting shock reflection back into the main flow of the tube resulting in large pressure fluctuations in the pressure profile.

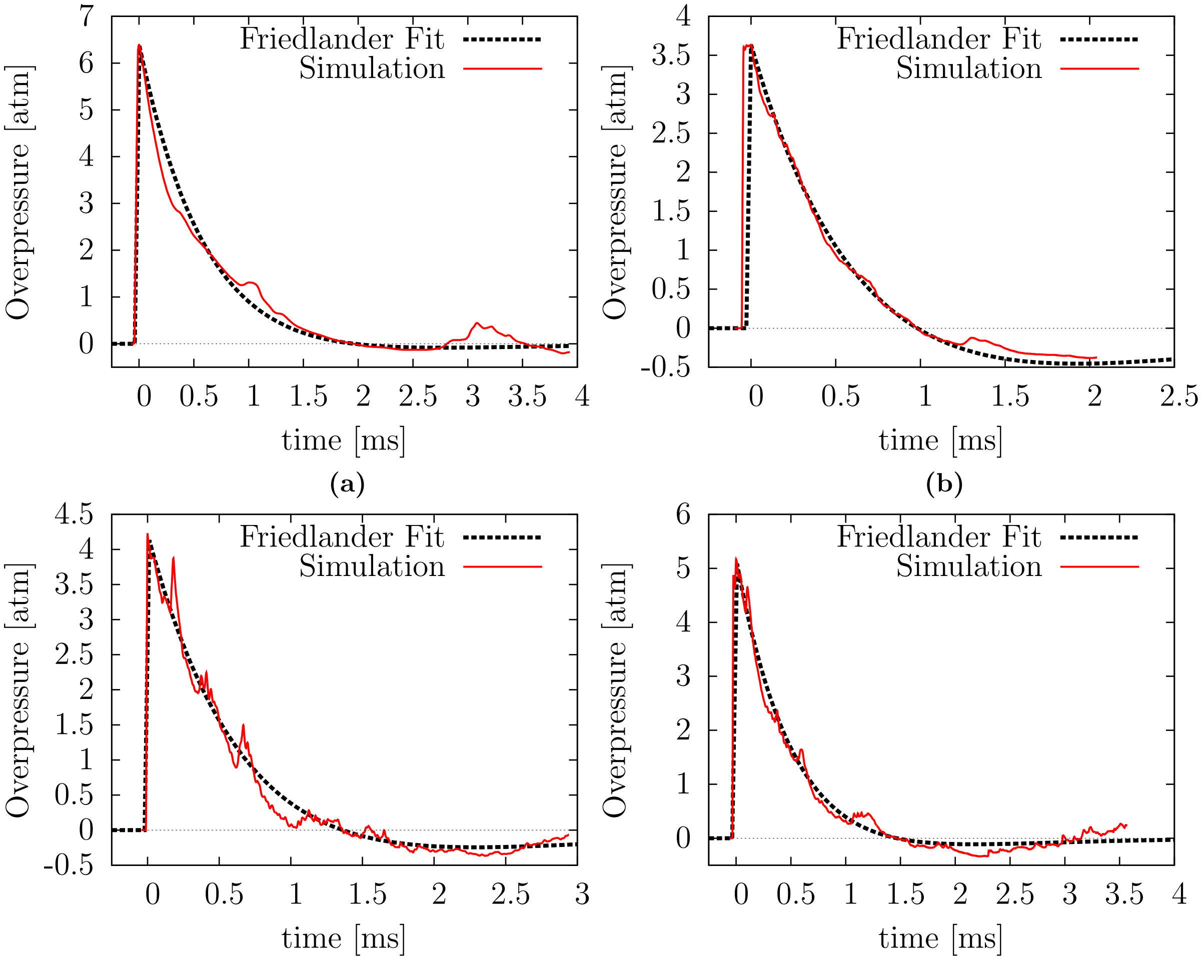

(a)

(b)

(c)

(d)

Figure 3.8: Pressure-time history at the exit of the shock tube illustrating the effect of various vent configurations. Shock tube parameters are $\frac{l}{r} = 10$ and $L_{driver} = 20\%$.
(a) No vent (b) $x_{vent} = 20\%$ and $l_{vent} = 10\%$ (c) $x_{vent} = 50\%$ and $l_{vent} = 10\%$
(d) $x_{vent} = 50\%$ and $l_{vent} = 5\%$.

There is also limitations on the position of the vent. Adding the vent at more than 50% of the length of the tube does not allow enough time for the expansion to significantly affect the profile, as shown in figure 3.9 (b). Additionally, the lower shock pressures observed near the end of the tube contributes to reducing the strength of the induced volumetric expansion.

It should be noted that there is some disturbance of the expansion profile in all profiles generated with vented shock tube configurations. As discussed above, some of these oscillations are caused by the curvature of the wave, generated by the expansion of the flow, reflecting from the inner surface of the shock tube. This effect is also caused, in part, by a limitation of the numerical framework. The thickness of the shock tube wall in the simulations is limited to a relatively large size, due to a limitation in the numerical framework. This thick wall causes increased shock reflections off of the cross section of the wall which add to the pressure disturbances. In an experimental setting this shortcoming can be minimized by the use of a sharp edge or ”cookie cutter” placed at the end of the vent, reducing the strength of this effect.

Consequently, it has been found that to add a negative phase to the pressure profile generated by the shock tube while maintaining a good expansion profile, an annular vent should be placed at less than 50% of the total length of the shock tube and should span no more than 15% of its length.

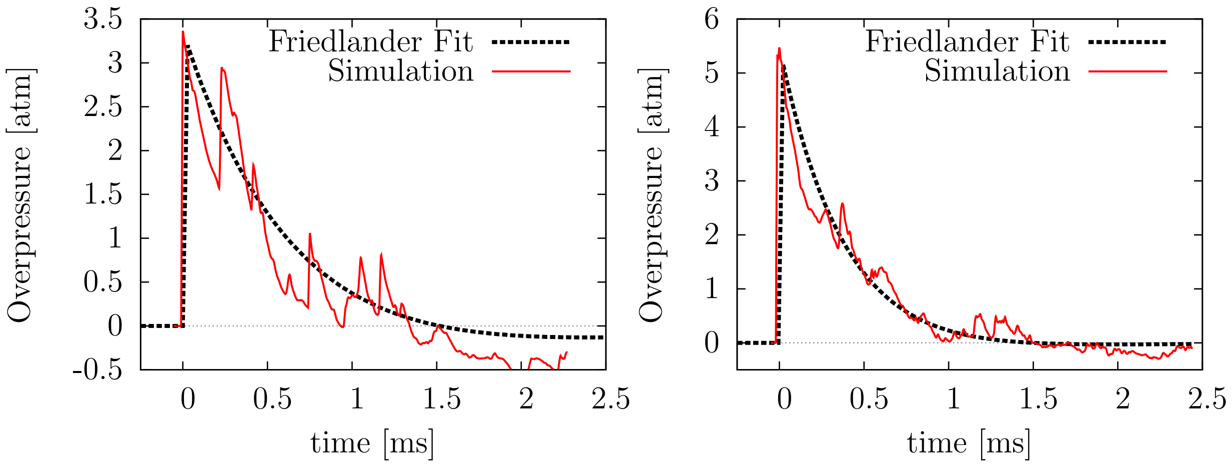

(a) **(b)**

Figure 3.9: Pressure-time history at the exit of the shock tube generated by failed vent configurations. (a) $x_{vent} = 50\%$ and $l_{vent} = 20\%$ (b) $x_{vent} = 60\%$ and $l_{vent} = 10\%$.

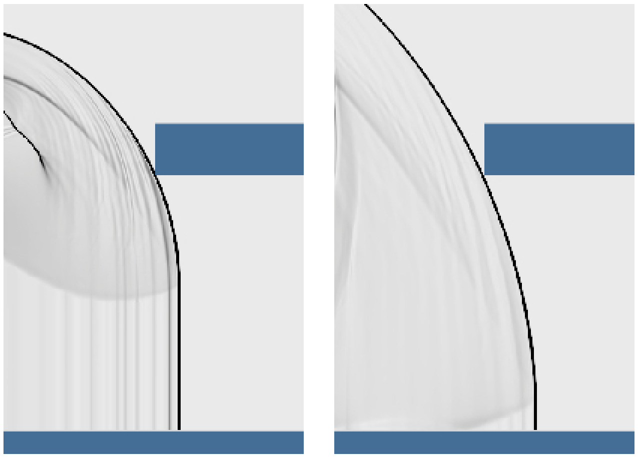

(a) **(b)**

Figure 3.10: Curvature of the shock wave as it reaches the end of the vented section. Vent spans (a) 10% and (b) 20% of the total length of the shock tube.

3.3 Selecting the Shock Tube Configuration

Section 3.2 presents the guidelines for the construction of the tube such that it will be able to produce Friedlander waves. Namely, the driver section length should be kept below 20% of the total length of the shock tube. A negative phase can be produced with the addition of an annular vent placed at less than 50% the length of the shock tube and spanning from less than 15% of its length. The use of annular vents allows for flexibility in the implementation of the design. By constructing the shock tube in multiple segments, a vent can be added or removed by separating or joining sections of the tube. In this way the user can adjust the parameters of the tube to obtain the desired pressure profile at the exit of the tube. In order to select the optimal range of shock tube lengths, the pressure profiles obtained from the numerical simulations must be compared to those created in free field applications.

A standard measure for the force of a blast wave is the mass of TNT, in kilograms, required to obtain an equivalent wave. This quantity paired with a distance away from the blast center is sufficient to describe a Friedlander blast wave [32]. By applying the blast scaling laws, an equivalent charge mass and distance away from the blast center of a TNT explosion can be calculated for the blast profiles generated by each simulated configuration. The methodology for finding equivalent TNT charge masses is outlined in appendix B.

While appendix C contains a complete list of the shock tube configurations that were investigated numerically in the context of this thesis, only those that meet the criteria discussed above have been reproduced in table 3.1. For each shock tube configuration the resulting Friedlander parameters and equivalent blast parameters are also shown.

As shown in table 3.1, the calculated equivalent mass of TNT varies greatly. It is important to note, however, that the energy contained in the driver section of the shock tube does not vary so greatly. In a hemispherical blast, the energy of the blast wave drops very rapidly in the early times of the volumetric expansion. By contrast, the energy in a shock tube is contained and focused. Thus, for a given increase in driver size, a seemingly disproportionate change in the equivalent charge mass is, in reality, counteracted by a smaller increase of the equivalent distance away from the blast center.

In order to maintain the ability to cover the largest possible range of equivalent TNT charges, a shock tube configuration consisting of four sections, each with a length to radius ratio of $l/r = 6$ has been selected. This way, using a different number of sections will allow for different overall shock tube lengths. The addition of the vent, can be accomplished by simply separating two section of the shock tube. In table 3.1, each row marked with a bold-font number represents a possible configuration using the chosen dimensions. This allows for a large range of equivalent TNT charges, ranging from 200 g of TNT at 1.2 meters up to over 145 kg of TNT at a distance of approximately 8 meters.

Table 3.1: Subset of the numerical results presented in table C.1 limited to the simulations that produced the best Friedlander profiles.

	Shock Tube Parameters				Friedlander Equation Parameters			Equivalent Blast Parameters.	
#	l/r	Fill %	x_{vent}	l_{vent}	α	t^+ [sec]	P_s [atm]	W_{equiv} [kg]	d_{equiv} [m]
1	3	0.10	n/a	n/a	1495.39	1.02E-003	3.18	0.52	1.69
2	3	0.20	n/a	n/a	2130.79	7.55E-004	5.70	0.22	1.01
3	5	0.10	n/a	n/a	1162.73	1.23E-003	3.30	0.96	2.04
4	6	0.10	0.50	0.10	1682.09	7.39E-004	3.13	0.20	1.23
5	6	0.20	0.50	0.10	2868.63	8.74E-004	5.46	0.33	1.18
6	7	0.10	n/a	n/a	941.47	1.56E-003	3.35	2.02	2.60
7	7	0.20	n/a	n/a	1588.15	1.42E-003	6.29	2.05	2.03
8	8	0.20	0.50	0.10	1798.02	1.17E-003	5.00	1.79	2.15
9	10	0.10	n/a	n/a	724.90	2.11E-003	3.40	5.12	3.52
10	10	0.15	0.30	0.10	1202.88	1.16E-003	3.62	1.41	2.22
12	10	0.15	0.50	0.10	1209.22	1.51E-003	3.69	3.27	2.92
12	10	0.15	n/a	n/a	419.24	4.21E-003	4.54	73.04	7.59
13	10	0.20	0.30	0.10	1181.07	1.04E-003	4.65	1.15	1.89
14	10	0.20	0.50	0.05	1426.46	1.46E-003	5.17	0.7	1.94
15	10	0.20	0.50	0.10	1075.97	1.36E-003	4.23	2.28	2.43
16	10	0.20	0.50	0.10	1075.97	1.36E-003	4.23	2.28	2.43
17	10	0.20	0.50	0.15	1214.75	9.30E-004	3.72	0.78	1.80
18	10	0.20	n/a	n/a	1247.14	1.96E-003	6.41	5.41	2.79
19	12	0.10	n/a	n/a	582.49	2.55E-003	3.41	9.11	4.27
20	12	0.15	0.50	0.10	1419.69	1.38E-003	4.14	0.74	1.69
21	12	0.15	n/a	n/a	686.97	2.48E-003	4.93	16.73	4.54

Table 3.1: continued.

	Shock Tube Parameters				Friedlander Equation Parameters			Equivalent Blast Parameters.	
#	l/r	Fill %	x_{vent}	l_{vent}	α	t^+ [sec]	P_s [atm]	W_{equiv} [kg]	d_{equiv} [m]
22	12	0.20	0.50	0.10	1403.92	1.42E-003	4.88	3.09	2.59
23	12	0.20	n/a	n/a	965.62	2.56E-003	6.51	12.18	3.63
24	14	0.15	0.50	0.10	1512.47	1.82E-003	4.08	1.71	2.25
25	14	0.20	0.50	0.10	992.79	1.41E-003	4.39	2.62	2.53
26	15	0.15	n/a	n/a	597.02	2.99E-003	4.94	29.47	5.48
27	15	0.20	n/a	n/a	839.98	3.10E-003	6.50	21.80	4.41
28	18	0.10	n/a	n/a	456.73	3.40E-003	3.38	21.33	5.69
29	18	0.15	n/a	n/a	535.15	3.46E-003	5.03	46.56	6.35
30	18	0.20	n/a	n/a	735.35	3.72E-003	6.51	37.65	5.29
31	24	0.04	n/a	n/a	394.44	2.69E-003	1.76	3.20	3.97
32	24	0.05	n/a	n/a	350.77	3.27E-003	2.02	5.38	4.48
33	24	0.09	n/a	n/a	366.08	4.10E-003	3.09	33.32	6.80
34	24	0.10	n/a	n/a	360.27	4.45E-003	3.35	46.82	7.42
35	24	0.15	n/a	n/a	424.21	4.58E-003	5.11	110.11	8.43
36	24	0.20	n/a	n/a	629.88	5.86E-003	6.48	146.23	8.33

Chapter 4

Mechanical Design

As described in the previous chapter, the chosen shock tube configuration consists of four sections, each with a length of $l/r = 6$. Given that the diameter of the shock tube is set to 30.5 cm by the length scale of the test objects of future studies, the tube section length is then set to 91 cm yielding total tube length of 3.7 m. Figure 4.1 shows an illustration of the chosen shock tube configuration. The upstream extremity of the tube is closed by an end plate which incorporates the gas injection port and the ignition system terminal. The downstream end of the shock tube is terminated by a large expansion chamber to disperse the energy of the generated shock waves. Each shock tube segment is supported independently by an adjustable frame. Each of these main features is illustrated in figure 4.1. The driver section of the shock tube is separated from the driven section by a bag type diaphragm, which is attached to the back plate of the shock tube. During a test, an empty diaphragm is attached to the back plate which is then closed and secured to the shock tube. The diaphragm is inflated with the reactive mixture which is then ignited via a high voltage ignition system (HVI). The detonation and resulting shock wave propagate through the tube and eventually into the expansion chamber that dissipates the energy. Once the test is complete the combustion products and remaining pressure in the tube are removed by an evacuation duct system.

The loading condition used to design the shock tube was that of a reflected detonation wave impinging on the back wall, generated by a stoichiometric oxy-acetylene mixture initially at atmospheric pressures and temperatures. This gas mixture has been chosen for its high CJ detonation pressure, which is on the order of 35 atm. Given that the peak pressure of a normal detonation reflection is approximately 2.5 times [33], the design pressure of the shock tube was set to 87.5 atm. However, at the time of writing it was

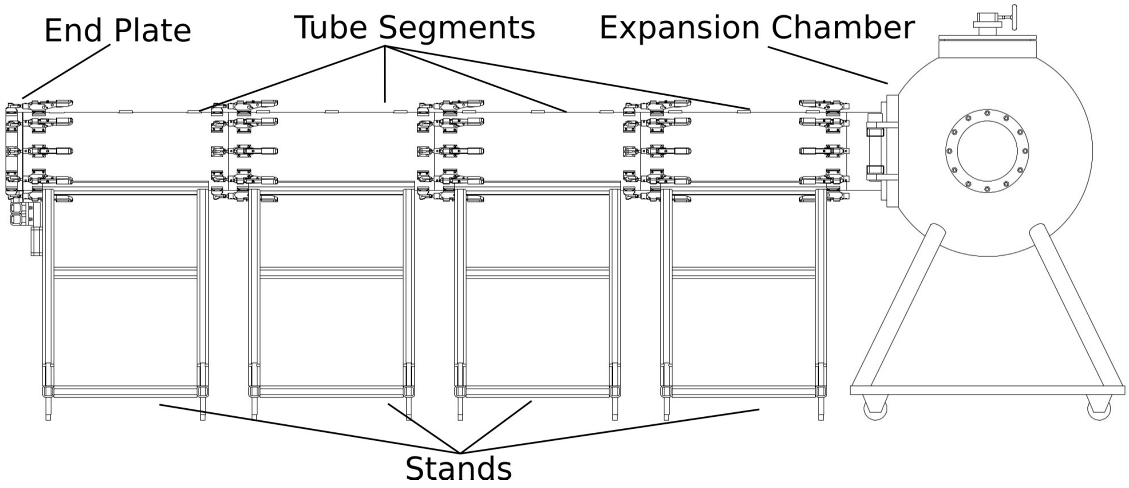

Figure 4.1: Schematic representation of the shock tube configuration. Consisting of four independent sections, an upstream back plate (left) and a downstream expansion chamber (right).

discovered that the manufacturer of the clamps used in the design, had committed an error by over-representing their strength. This has required that the design pressure be lowered. The design pressure loading of the shock tube is therefore set to 75.8 atm to accommodate the implementation of the replacement clamps. This pressure loading corresponds to a fully reflected, acetylene-oxygen detonation wave with an initial pressure of 0.6 atm.

The remainder of this chapter will focus on the various mechanical components of the tube and the design elements of each. The design parameters and strength values discussed in the present chapter will be in reference to the sample calculations included in appendix D.

4.1 Design Components

4.1.1 Tubes

The main body of the shock tube has been constructed from four 91.4 cm long sections of ASTM A519 pipe constructed from AISI 1020 steel. The pipe has an inner diameter of 30.5 cm and a wall thickness of 2.54 cm. Three flattened areas have been machined into the outer surface of the pipes to allow for the mounting of the pressure sensors. These flat areas are equipped with the necessary bolt holes to properly mount the plugs that support the pressure sensors. The flat faces on either end of each tube segment have been machined smooth and an o-ring groove has been added to one of the faces to create a seal at the interface. The large thickness of the tube allows these faces to act as sealing surfaces for the shock tube, eliminating the need for additional flanges.

4.1.2 Retention System

The separate sections of the shock tube are secured to each other by a series of latch clamps located at each interface. Ten clamps are used per interface. Each clamp is bolted to a steel plate that has been welded to the body of the tube. The latch clamps and respective hooks, shown in figure 4.2, have been purchased from Elesa[1], and were selected for their ability to withstand 75 kN of force each. However as mentioned above, this value does not represent the true strength of these clamps. In fact, the true strength of the original clamps is 7.5 kN, which would result in a maximum operating pressure of 10 atm.

Replacements clamps have been found and will replace the original clamps, though they have a rated load of 40 kN each. The number of clamps will be increased to 14 per interface between the tube sections. As mentioned previously, with the replacement clamps, the maximum operating condition of the shock tube will be a pressure of 75.8 atm. At these pressures the shock tube will be able to withstand a fully reflected detonation with an initial pressure of 0.6 atm, impinging on the back plate with a safety factor of 1.5. The remainder of this chapter will, nonetheless, present the design of the tube incorporating the original clamps in order to represent the work accomplished.

4.1.3 Supports

Each tube segment is supported by a separate stand, shown in figure 4.3. The stands consist of welded A-frames constructed from 2x2x0.25” square steel tubing. Each stand is equipped with four adjustable feet in order to properly align the sealing surfaces of the tubes. Each stand has incorporated sufficient ground clearance to allow its transportation by a standard pallet truck, simplifying the procedure for reconfiguring the shock tube.

---

[1] www.elesa.com

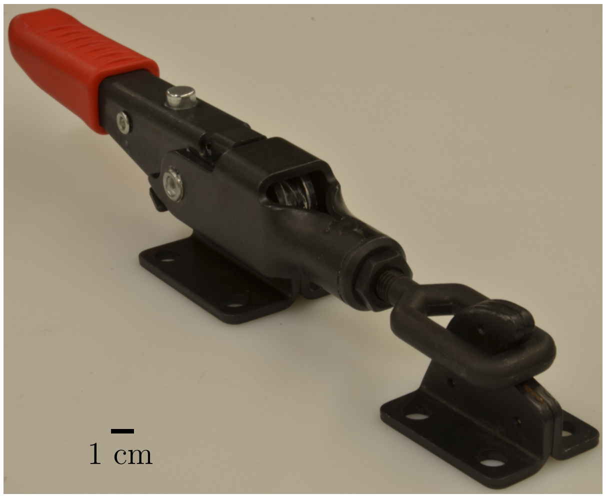

Figure 4.2: Retaining clamp purchased from Elesa.

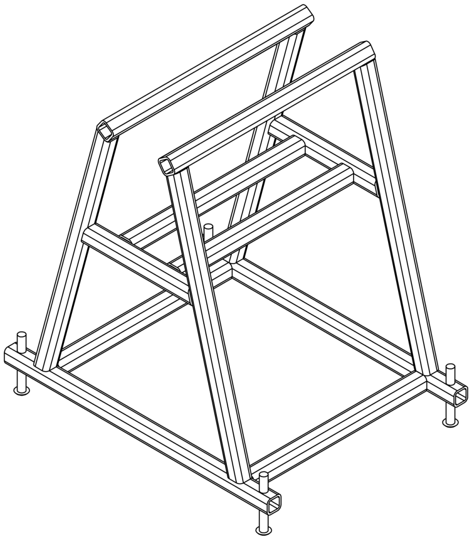

Figure 4.3: Illustration of shock tube section support.

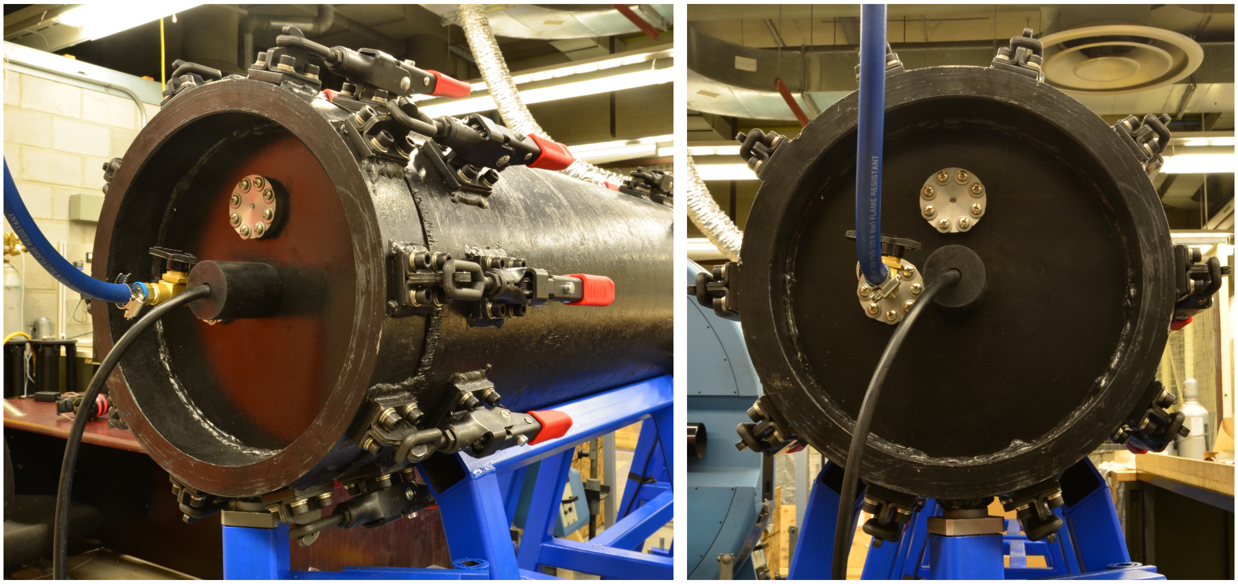

(a) (b)

Figure 4.4: View of the end plate; illustrating the placement of the gas injection port, the HVI and optional pressure port.

While three of the stands are identical, the support for the first, most upstream, tube section incorporates an extra section of square tubing which supports the swing arm mechanism for the end plate.

4.1.4 The End Plate

The end plate is located at the upstream end of the shock tube and is constructed from 2.54 cm thick steel plate. A short section of tube cut from the same stock as the shock tube sections is welded to the outside of the plate to allow enough space for the latch clamp hooks to be mounted, as is illustrated in figure 4.4. The back plate is also equipped with three different mounting ports. The mounting port for the HVI is located in the center of the end plate, with a gas injection port located just to its left. There is also an optional pressure sensor port located above the ignition plug.

The end plate is supported by a pivoting arm. The configuration of this arm are shown in figure 4.5. The overall length and height of the swing arm is adjustable to ensure the alignment of the back plate with the main body of the tube.

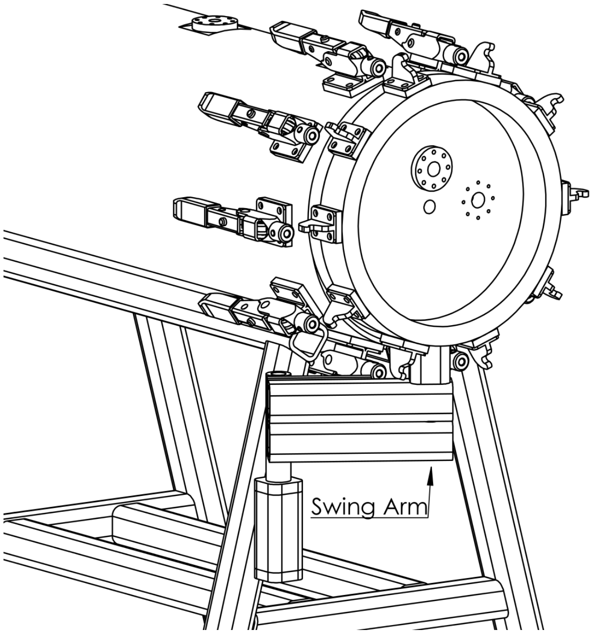

Figure 4.5: Illustration of end plate swing arm support.

4.1.5 Diaphragm Retention System

Figure 4.7 shows the inside of the end plate, which incorporates the diaphragm retention system. In preparation for a test, a sheet of thin plastic is formed into a cylindrical shape around the retaining ring as illustrated in figure 4.6. An adjustable stand used to shape the diaphragms. The stand supports a retaining ring, comprised of a large diameter hose clamp, through which the plastic sheet and a forming disc are stretched. The height of the bottom plate of the stand ensures that the length of the diaphragm conforms to the required dimension for the test, while the forming disc maintains a flat profile at the end of the diaphragm. A silicone coated, steel diaphragm ring is then inserted on the inner surface of the diaphragm against which the hose clamp is secured. The diaphragm assembly is deflated and flattened before being secured to the back plate of the shock tube with tabs that are mounted on the inner steel ring. Constructing the diaphragm in this way ensures that, when inflated in the tube, it will retain a flat surface at its end.

The mounting ring is then secured to the end plate by inserting the tabs on the diaphragm ring into the anchor blocks show in figure 4.7. The ring of red high-temperature silicone shown in figure 4.7 aids in maintaining a seal between the back plate and the

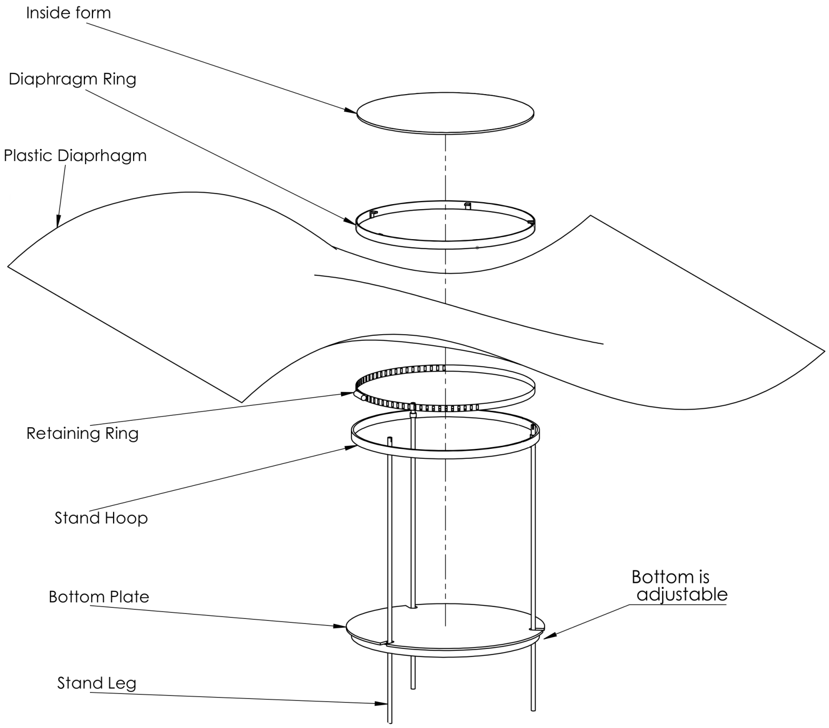

Figure 4.6: Illustration of diaphragm unit assembly.

diaphragm. The diaphragm is flattened before installation, and becomes inflated when the reactive gas is added. Note that the amount of gas added to the diaphragm is controlled by the gas handling system, therefore, eliminating the risk of over inflating the diaphragm.

4.1.6 Gas Handling

Gasses used in the driver section of the shock tube are pre-mixed and left to diffuse for a 12 hour period to ensure uniform properties. While the diaphragm maintains a sharp boundary between the driver and driven sections, the amount of gas injected into the shock tube is controlled trough a pressurized gas injection system. It is assumed that the driver section filling process is accomplished slowly, such that the gas mixture has sufficient time to return to ambient temperatures after expanding from the injection tank. Therefore, a simple isothermal expansion calculation is used to determine the required pressure in the injection tank, such that when expanded to atmospheric pressure, its volume encompasses the injection tank, the hose leading to the shock tube and the volume of the driver section.

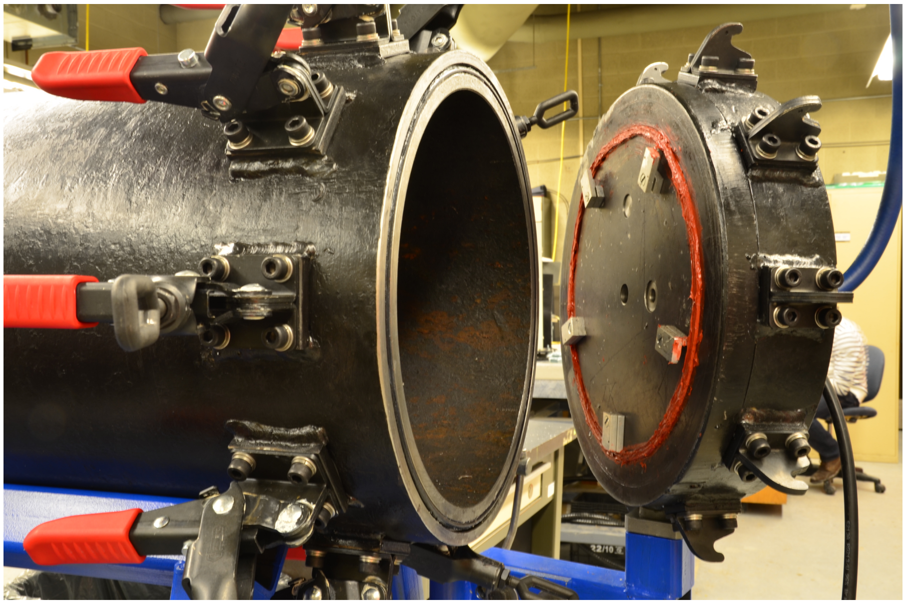

Figure 4.7: View of inside of the end plate. Also shown, anchoring blocs and red sealant ring of the diaphragm system.

4.1.7 Ignition System

To ensure direct initiation of a detonation in the driver section, a high voltage ignition system is used. A capacitor bank charged to 20 kV delivers an estimated 5 joules directly to the gas surrounding the HVI electrodes. For many fuel-oxygen gas mixtures at ambient temperatures and pressures, this is sufficient to induce detonation directly [34].

4.1.8 Data Acquisition

As previously mentioned, each shock tube segment is equipped with three pressure measuring ports, spaced at 30.5 cm intervals. Pressure signals are recorded using piezoelectric sensors, shown in figure 4.8 (a). A sampling rate of 1 Mhz per channel has been selected in order to sufficiently resolve the arrival of the shock wave and the following expansion. Each sensor is supported by and sealed into a pressure sensor plug which is mounted onto the shock tube. An o-ring groove has been added to each plug to maintain a seal with the main body of the shock tube.

(a) **(b)**

Figure 4.8: Pressure sensor and mounting plug.

4.1.9 Expansion Chamber

The expansion chamber located at the downstream end of the shock tube, illustrated in figure 4.9 (a), consists of a 90 cm diameter hollow steel sphere. This volume is sufficiently large to lower the final pressure of the expanding driver gasses to slightly above ambient pressure as well as housing any future test objects. There is a valve located on the top of the chamber to allow the combustion products to be vented into an exhaust ventilation system after each test. Attached to the front opening of the chamber is a coupler, shown in figure 4.9 (b) which connects the shock tube to the expansion camber. The coupler is also equipped with an o-ring groove to ensure a proper seal with the shock tube and is equipped with a silicone gasket at the interface with the expansion chamber.

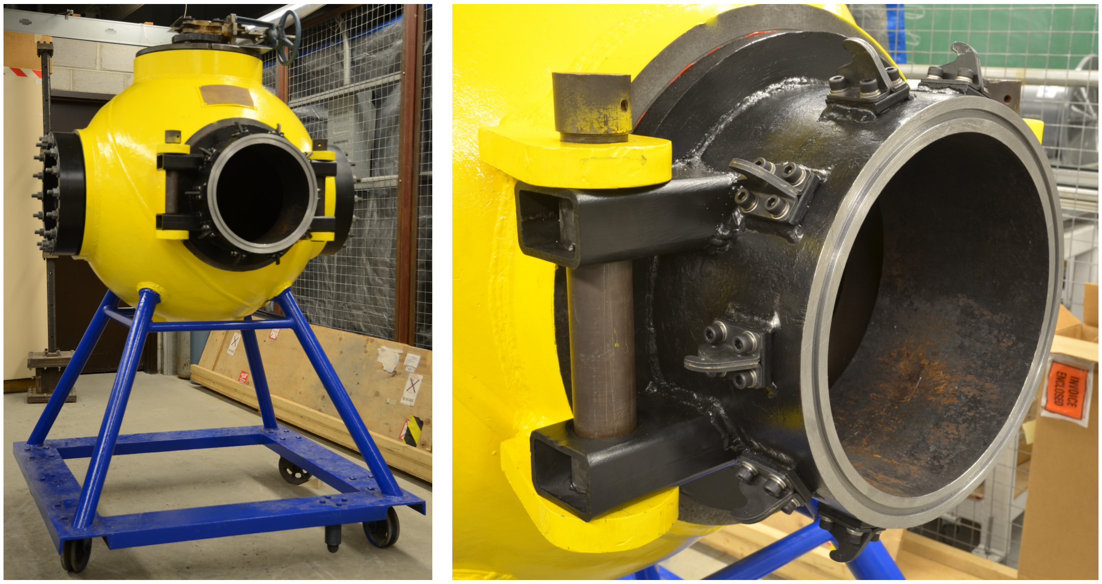

(a) **(b)**

Figure 4.9: Expansion chamber and attached coupler.

Chapter 5

Experimental Results

A series of experimental tests have been conducted to validate the shock tube design and to ensure its operation as predicted by the numerical simulations. For each test, the pressure history was recorded at four locations along the tube. The locations of each pressure sensor is listed in table 5.1, where the port number is the number of the pressure sensor port counting away from the back plate. All tests were accomplished with the shock tube at its full length of 3.7 m (12 ft), using all four sections. The driver section length was varied between tests within the range of 20% and 4% of the total length of the shock tube. All tests implemented a driver mixture of stoichiometric ethylene oxygen at atmospheric temperature and pressure.

Table 5.1: Location of pressure sensors for experiments.

Sensor #	Port #	Distance from back plate [m]
1	1	0.15
2	5	1.37
3	8	2.29
4	12	3.51

The list of conducted tests and their corresponding fill percentages are shown in table 5.2. Also included in the table is the average time of arrival difference between the experiment and a corresponding simulation ($\overline{\Delta t}$). This value is found by calculating the average of the differences between the measured shock time of arrival at each sensor location and the time of arrival value predicted for that sensor by simulation. The collection of all pressure sensor profiles recorded during the experiments is included in appendix F. These profiles show the pressure history recorded at each of the sensor locations. The types of sensors used for all tests were piezo-electric, which tend to produce noisy signals caused by ringing. Therefore, tests with higher fill percentages, which produced stronger shock waves, generated a significant amount of noise in the pressure profile, as illustrated in figure 5.1 (d).

Table 5.2: Experiment parameter table, indicating the driver size expressed as a percentage of the shock tube length and the average time of arrival difference with simulation ($\overline{\Delta t}$).

Test #	Fill %	$\overline{\Delta t}$ [ms]
1	0.10	0.28
2	0.05	0.09
3	0.05	0.13
4	0.06	0.31
5	0.20	1.43
6	0.15	0.63
7	0.15	0.57
8	0.05	0.08
9	0.20	0.39
10	0.04	0.22

5.1 Pressure Profiles

Figure 5.1 shows a representative selection of the pressure profiles recorded closest to the exit of the tube. Despite the inherent noise of Piezoelectric transducers, there is good agreement between the experimental profiles and those obtained from simulation, especially at lower fill percentages. The profiles near the end of the shock tube show the characteristics of a Friedlander wave, with a rapid and steady decrease in pressure behind the shock wave. The shock tube is therefore verified in its ability to produce Friedlander like blast waves.

Due to the large diameter of the shock tube, there may also be fluctuations in the velocity of the wave across the area of the tube as it propagates. Any deviation from a planar wave would cause pressure and velocity fluctuations across the shock front until it eventually comes to equilibrium. Such deviations may be caused by bulge in the end of the diaphragm, for example. A smaller driver section allows for more distance over which the shock front can even out any fluctuations, further explaining the better agreement of the pressure profiles produced by smaller driver sections.

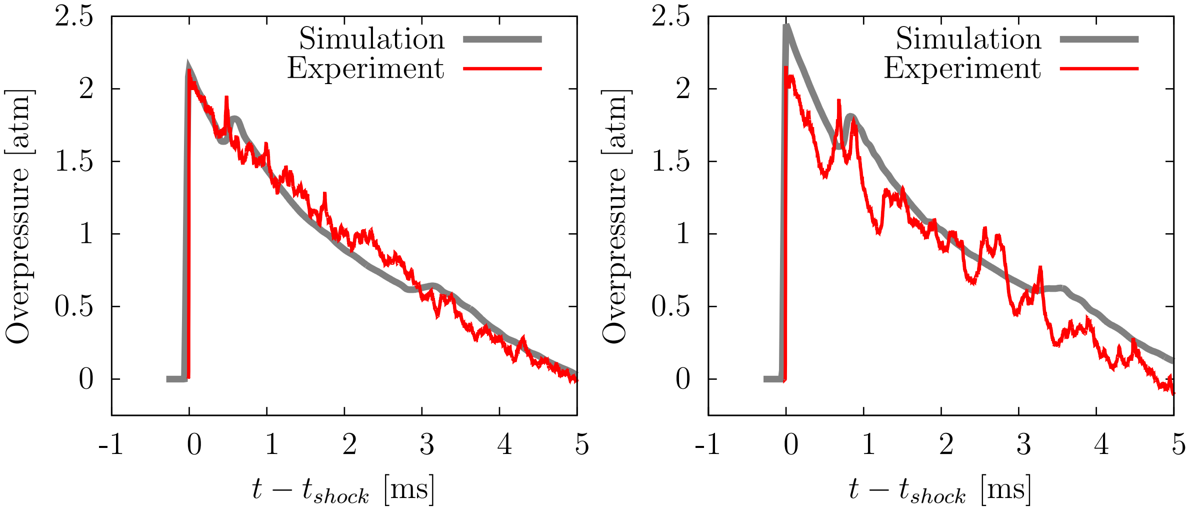

(a) Test 8 - 5% fill. **(b)** Test 4 - 6% fill.

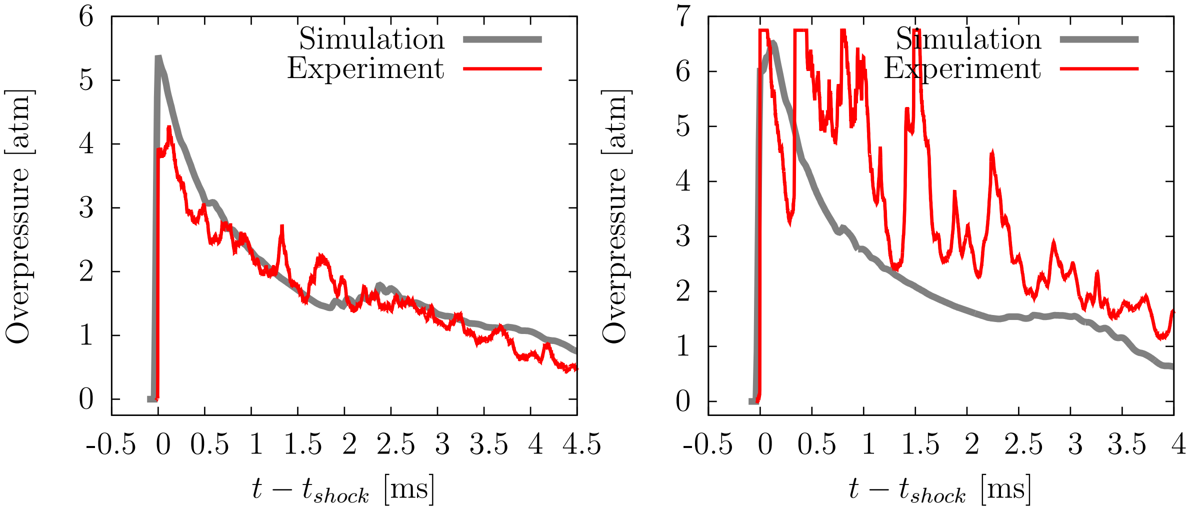

(c) Test 7 - 15% fill. **(d)** Test 9 - 20% fill.

Figure 5.1: Selection of experimental pressure profiles recorded at sensor location #4, compared to numerical simulation.

5.2 Position-Time Results

The comparison between the simulations and the conducted experiments is most clearly accomplished with the position-time (x-t) diagrams. The ability of the sensors to accurately detect the time of arrival of the shock wave is not affected by noise as is their ability to measure the strength of the shock. Therefore, these results may be analysed in a more quantitative manner.

Figures 5.2 and 5.3 show the x-t data obtained from simulation and experiment; there is good agreement between all tests and simulations, with the sole exception of test 5. Table 5.2 shows the difference of time of arrival of the shock wave between each experiment and the corresponding simulation, averaged over each sensor location. The difference between simulation and experiment remains within 1 millisecond. During test 5, shown in figure 5.3 (c), the gas mixture in the driver section failed to sustain a full detonation and the produced shock wave fell behind the path predicted by the numerical simulation.

5.3 Experimental Result Summary

Over all, the experimental results are found to validate the shock tube design. Some differences in the produced pressure profiles are found, particularly at higher shock wave pressures, which may be attributed to sensor noise. Nonetheless, the main Friedlander wave characteristics have been observed in the experimental profiles. Additionally, the shock wave x-t results agree well with the conducted simulations, further validating the shock tube design. Through out all experiments the results have been shown to be very repeatable, with the sole exception of test 5. During test five, the detonation wave in the driver section failed to initiate completely, leading to the large deviation in the arrival times of the shock wave.

Due to restrictions on the location of the shock tube, vented tests could not be conducted due to safety concerns. In order to conduct vented test, a more protected and separated location for the shock tube would need to be procured. Alternatively a protective enclosure could be constructed around the vented section of the shock tube.

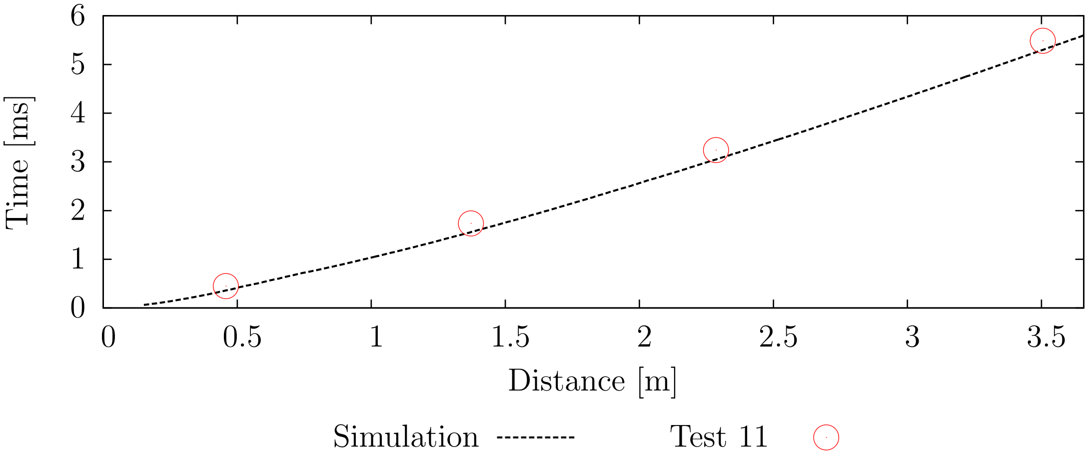

(a) 4% fill.

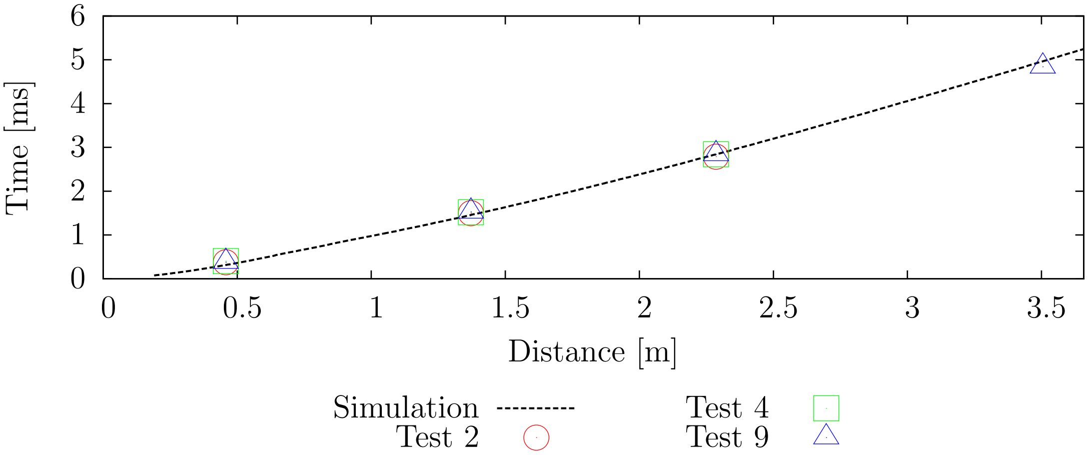

(b) 5% fill.

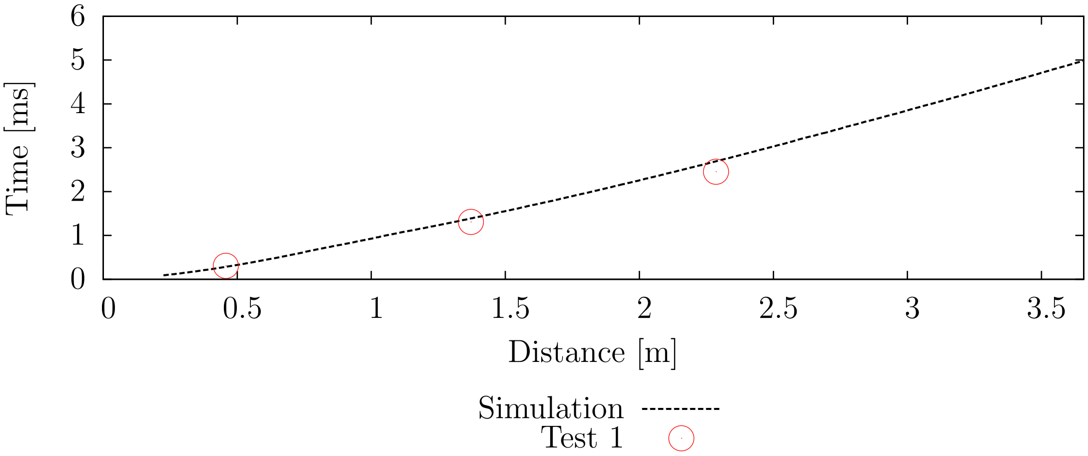

(c) 6% fill.

Figure 5.2: Comparison of experimental and numerical shock wave x-t diagrams.

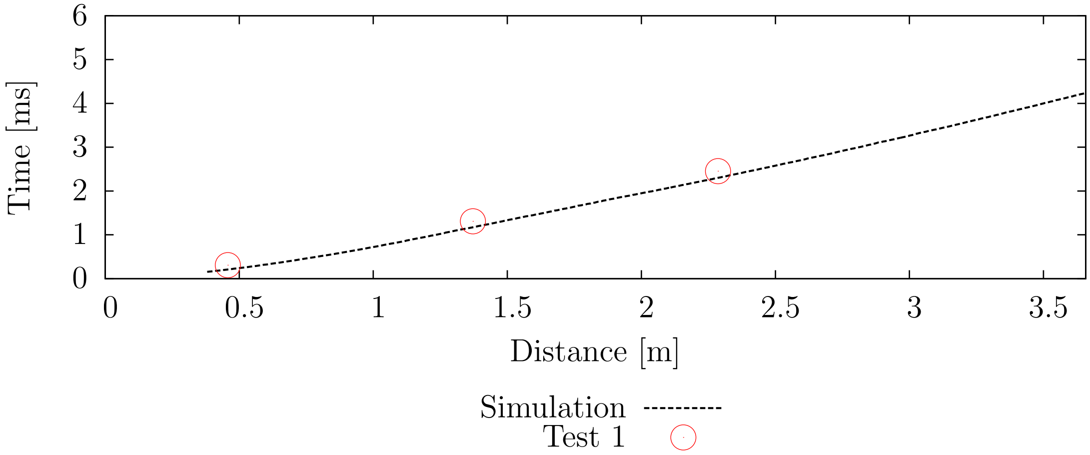

(a) 10% fill.

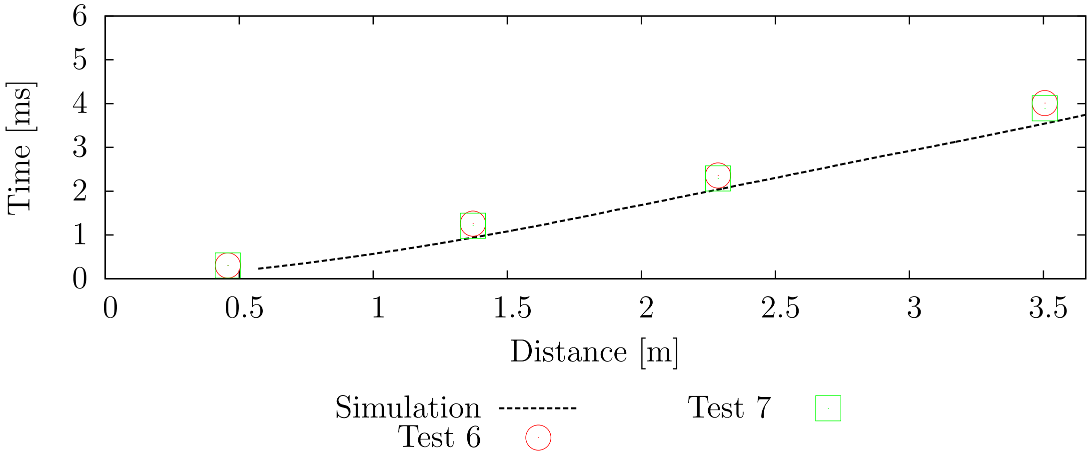

(b) 15% fill.

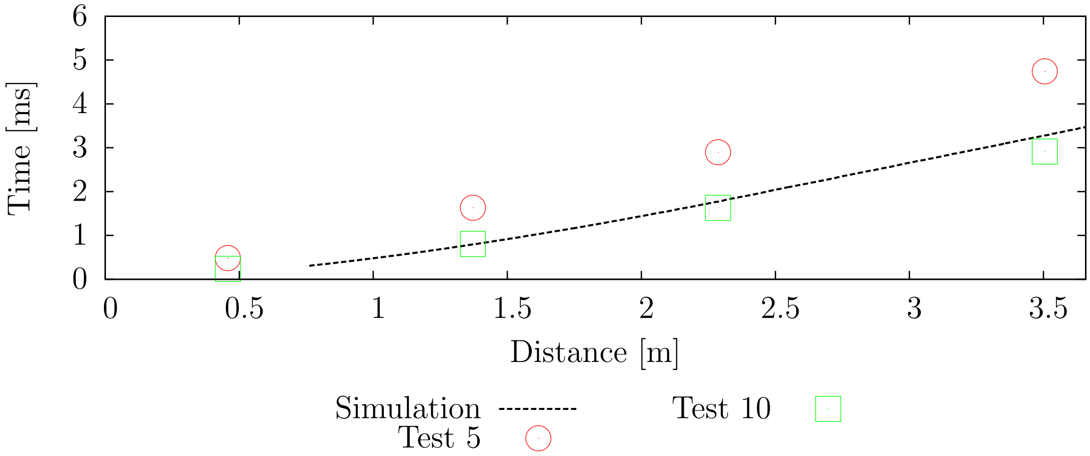

(c) 20% fill.

Figure 5.3: Comparison of experimental and numerical shock wave x-t diagrams. (Continued.)

Chapter 6

Conclusion

A 30.5 cm diameter shock tube facility has been constructed that is capable of generating pressure profiles similar to those created by free field explosions. Through numerical simulation the optimal shock tube configurations have been identified. For the generation of Friedlander wave profiles, the driver section must have a length of less than 20% of the total length of the shock tube. Additionally it has been found that a more pronounced negative phase can be obtained with the addition of an annular vent placed at or below 50% of the length of the shock tube and spanning up to 15% of its length.

The shock tube has been constructed from four section of steel pipe terminated by a back plate and an expansion chamber on the upstream and downstream sides, respectively. Shock waves are generated by a driver section filled with a detonable gas mixture. The length of this driver section is adjustable through the use of a bag type diaphragm that separates the driver and driven sections. Ignition of the mixture is accomplished by a high voltage ignition system. Finally an expansion chamber contains the generated shock wave and the combustion products for safe evacuation.

Certain limitations have required a re-evaluation of the design parameters of the shock tube. Firstly, due to manufacturer error, the clamps holding the shock tube sections together must be replaced with alternative clamps that are able to hold 40 kN of force each. Thus, the operating conditions of the shock tube must be changed to a maximum operating pressure of 75.8 atm accounting for a safety factor of 1.5. This corresponds to withstanding a fully reflected detonation with an initial pressure of 0.6 atm. Secondly, vented tests could not be conducted due to safety concerns given the location of the shock tube.

The numerical results obtained agree well with the measured values obtained from experiments. Experimental position-time histories of the generated shock wave agree particularly well with simulation, due to their insensitivity to sensor noise. Generated pressure profiles also agree with simulation results, exhibiting the characteristics of a Friedlander wave, despite their susceptibility to noise. Sources of experimental error include deviations in the diaphragm from a purely cylindrical shape as well as ringing in the piezoelectric sensors.

Future work on the shock tube will require the installation of the obtained replacement clamps. Additionally, in order to conduct vented experiments with the shock tube some modifications must be made. For example, a second expansion chamber can be constructed and secured around the vent area. In this way the escaping shock waves and burned gasses can be contained and alleviate any safety concerns.

Appendix A

AMRITA Scripts

Listing A.1: AMRITA script for shock tube simulations.

```
fold::amrita { define array sizes
        ArraySizes {
                NGIxJ   = 5000000
                NGD     = 10000
        }
}
fold::amrita { get paramater inputs for BASH scripting
   if(token(amrita::arg1)) then
      set lwR = $amrita::arg1 #Shock Tube length to radius
         ratio.
   else
      set lwR = 24
   endif

   if(token(amrita::arg2)) then
      set prcnt = $amrita::arg2  #Driver section fill
         percentage
   else
      set prcnt = 0.2
   endif
}
```

```
fold::amrita { magic constants
    set lmax   = 4                # Maximum refinement level
    set r      = 2                # Refinement Ratio
    set ls     = 1                # Length Scale
    set radius = 6                # tube radius

    set rhoStar =  1.1839   # Density of air at 25C
    set pStar   =  101300   # Atmospheric Pressure
    set lStar   =  0.0254   # 1 inch in meters

}
fold::amrita { domain geometry
    set it    #= $lwR*$radius+6    # Length of tube
    set jt    #= $radius           # Height of tube
    set ie    #= floor($it*0.6)    # Length of expansion area
    set je    #=  floor($it*0.3)   # Height of expansion area
    set xe2   #= floor(3*$it/4)    # start x-position of area around tube (to save memeory)
    set ye2   #= ($jt+3)           # start y-position of area around tube
    set ie2   #= ($it-$xe2+1)      # leght of area around tube
    set je2   #= ($je-$ye2+1)      # height of area around tube

    set loc   #= $it*$prcnt        # Location of gas interface
}
fold::amrita { ScanLine, for generating xt diagrams in 1D geometry simulations
    proc ScanLine {
        exposure [0:1]       = 0.9  # darkness of image
        amplification [0:?]= 50   # magnification of weak features
        grid                 = {G}  # select grid
        min                  = 0.0
        max                  = 10.0
```

```
      }
      DrhoDx       ::= (RHO[+i]-RHO[-i])/(X[+i]-X[-i])
      schlieren    ::= sqrt(DrhoDx[]**2)
      wt           ::= (schlieren[]-$min)/($max-$min)
      greyshading  ::= $exposure*exp(-$amplification*wt[])
      plot image $grid m<greyshading[]>
   end proc
}
fold::amrita{ define DensityGradientPlot
   proc DensityGradientPlot {
        exposure [0:1]     = 0.9  # darkness of image
        grid               = {G}  # select grid
        max                = 2.
        min                = 0.
     }
     DrhoDx        ::= (RHO[+i]-RHO[-i])/(X[+i]-X[-i])
     DrhoDy        ::= (RHO[+j]-RHO[-j])/(Y[+j]-Y[-j])
     schlieren     ::= sqrt(DrhoDx[]**2+DrhoDy[]**2)
     wt            ::= 1-((schlieren[]-$min)/($max-$min))
     wt            ::= wt[]>0 ? wt[] : 0
     greyshading   ::= $exposure*wt[]
     plot image $grid m<greyshading[]>
  end proc
}
plugin amr_sol
EulerEquations { Euler eqution parameters
   gamma = 1.15
   space = 2D
   symmetry = cylindrical
}
fold::amrita { get solver
   BasicCodeGenerator {
      scheme = kappa-muscl'operator-split
      solver = hlle_km
      flux = bcg/hlle
```

```
    }
    solver code/hlle_km
}
fold::amrita { Define Mesh Patches
    fold::amr_sol'Domain {
        lscale $ls
        #origin 0,0
        patch <+,1,w$it,h$jt>
        patch <+,1,w$ie,h$je>
        patch <$xe2,$ye2,w$ie2,h$je2>
    }
    fold::amr_sol'BoundaryConditions { Domain Boundary Conditions
        Nbdy domain:  extrapolate
        Nbdy default: reflect
        Sbdy domain:  reflect
        Sbdy default: reflect
        Ebdy domain:  extrapolate
        Wbdy domain:  reflect
        Wbdy default: reflect
    }
    fold::amr_sol'SolutionField { Initial conditons

        W'still  ::= <RHO=1,U=0,V=0,P=1>

        GasProperties loc=$loc, ls=$ls #Get Detonation Properties


        #Set TaylorWave expantion profile behind fill percentage in shock tube.
        setfield W'still
        if ($prcnt>=0.5) then
            setfield W'profile  X[]<$loc*$ls && Y[]<$jt*$ls
        else
```

```
            setfield W' profile  X[]<$loc*$ls
        endif
    }
    fold::amrita { Mesh Adaption
        def MeshAdaption
            adaption   on
            lmax       $lmax
            r          $r
        end def
    }
    fold::amrita { Mesh Refinement Criteria
        def RefinementCriteria
            DensityGradient
            ContactSurface
        end def
    }
    #Refine starting mesh
    makefield
    do l=1, $lmax
        adapt
        makefield
    end do
}

fold::amrita { march
    set Xfront = $jt*$prcnt    #Leading Shock Wave Position
    set n=1                    #Time step counter
    set flag = 0               #Flag to turn on setting itteration limit
    set xend #= ($it-1)        #Location of end of shock tube probe
    set nMax = 1000            #Preliminary time step limit

    # March and make postcript files for expansion
    while ($n < $nMax)
```

```

    #find shock position
    along y = 1 locate last P[]>1.1 -> Xfront

    #Set itteration limit
    if ($Xfront >= $it+$ie-3 && $flag==0)then
        set nMax = 2*$n
        set flag = 1
    endif

    #Make postscript files
    if ($Xfront > $it-6) then
        postscript on
        plotfile ./Schlieren/$lwR-$prcnt/sch$n.ps
            PlotDomain
            DensityGradientPlot
            AmritaBlue
        plotfile
    endif

    fold::amrita { Probe pressure at end of tube on top wall
        probe P[] at $xend*$ls,$ls*$jt-0.1 -> pval
        time -> t
        fold::amrita { Redimensionalize The values
            #Dimensionalize Pressure and time
            set pD #= $pval*$pStar
            set tD #= $t*$lStar*($rhoStar/$pStar)**0.5
            fold::print{ save to file
                fold> file.=./Probes/Probe1/Dim_$lwR-$prcnt.csv
                $tD $pD
            }
        }
    }
```

```

    fold::amrita { Get pressure profiles along top of shock tube
      set xprobe = 1
      while ($xprobe <= $lwR)
          probe P[] at $xprobe*$radius*$ls,$ls*$jt-0.1 -> pval
          time -> t
          fold::amrita { Redimensionalize The values
             #Dimensionalize Pressure and time
             set pD #= $pval*$pStar
             set tD #= $t*$lStar*($rhoStar/$pStar)**0.5
             fold::print{ save to file
                fold> file.=./Probes/ProbePorts/Dim_$lwR-$prcnt/$xend.csv
                $tD $pD
             }
          }
          set xprobe+=2
       end while
    }

    fold::amrita { print Profiles along axis
       set ytop = 1
       foreach Q (U,P,RHO)
          printfile ./Profiles/$lwR-$prcnt/$Q/$Q$n
          along y=$ytop print X[],$Q[]
       end foreach
    }

    march 1 steps with cfl=0.8
    set n+=1

  echo $n
  end while
```

```
    echo OK!
}
```

Listing A.2: AMRITA subroutine to define gas mixuture detonation properties.

```
# Ethylene−Oxygen Detonation Properties
proc GasProperties loc=1, ls=1
  TaylorWave2D Xs #= $loc*$ls , Pr=33.426, Rr=1.8517, DCr=1.8516, Cr=3.9169, state1=still state2=profile
end proc

# Pr = Detonation over−pressure
# Rr = Density ratio (pre/post cumbustion)
# DCr = Detonation velocity / Burned sound speed
# Cr = Sound speed ratio (post/pre cumbustion)
```

Listing A.3: AMRITA subroutine to define Taylor wave profile for initial conditions.

```
#
# Compute a taylor expansion wave behind the shock
#  Jonathan Armstrong, 2011.
#
proc TaylorWave2D Xs=10, Pr=33.864, Rr=1.8418, DCr=1.841, Cr=3.993, state1=quiescent, state2=profile
```

```

   g           ::= GAMMA'$state1

   u_int  ::=  $Cr * g[]**0.5 * ( $DCr/(g[]+1) *(2*X[]/$Xs + (g[]-1))-1)

   u      ::=  u_int[] > 0 ? u_int[] : 0

   xvar   ::=  ((g[]+1)/$DCr - (g[]-1)   )*$Xs/2

   p      ::=  X[] > xvar[] ? \
               $Pr*( ((g[]-1)/(g[]+1)) * $DCr * (X[]/$Xs - 1) + 1 )**(2*g[]/(g[]-1)) : \
               $Pr*( ((g[]-1)/(g[]+1)) * $DCr * (xvar[]/$Xs - 1) + 1 )**(2*g[]/(g[]-1))

   rho    ::=  X[] > xvar[] ? \
               $Rr *( ((g[]-1)/(g[]+1)) * $DCr * (X[]/$Xs - 1) + 1 )**(2/(g[]-1)) : \
               $Rr*( ((g[]-1)/(g[]+1)) * $DCr * (xvar[]/$Xs - 1) + 1 )**(2/(g[]-1))

  W'$state2  ::= <RHO=rho[],U=u[], V=0, P=p[]>

end proc
```

Appendix B

Blast Scaling - TNT Equivalence

A standard reference for the explosive energy of a blast wave is the required weight of TNT needed to produce a blast of equivalent strength. Any blast wave can be characterized by this value when combined with an equivalent distance away from the blast center. In the context of shock tube tests, this allows any produced blast profile to be compared to an equivalent TNT charge mass and distance form the blast center.

Equations (B.1)-(B.3) describe the equivalent TNT charge mass and distance away from the blast for any blast profile given its peak shock pressure and positive pressure phase duration. In order to obtain these equivalent blast parameters, however, a reference set of blast parameters is required. Figure B.1 shows experimentally obtained blast wave characteristics from the detonation of 1 kg charges of TNT, which can be used as a reference set. To find the equivalent charge mass and distance, denoted W_{TNT} and d_{eq} respectively, two steps must be followed. First, the given blast profile's peak pressure (P_{pr}) is matched to a pressure in the reference state on figure B.1, such that $P_{ref} = P_{pr}$. This yields the positive pressure duration and distance from the blast center at the reference state (t^+_{ref} and d_{ref}). Lastly the equivalent TNT charge mass and distance from the blast center are calculated using equations (B.1) to (B.3), which take into account the hemispherical expansion of the flow and two atmospheric transmission factors (f_t and f_d) to relate the reference and equivalent states. Note that the transimission factors are derived from the sounds speeds of the reference and equivalent states (C_{ref} and C_{eq}).

$$W_{TNT} = \left(\frac{t^+_{pr} \cdot f_t}{t^+_{ref}} \right)^3 \tag{B.1}$$

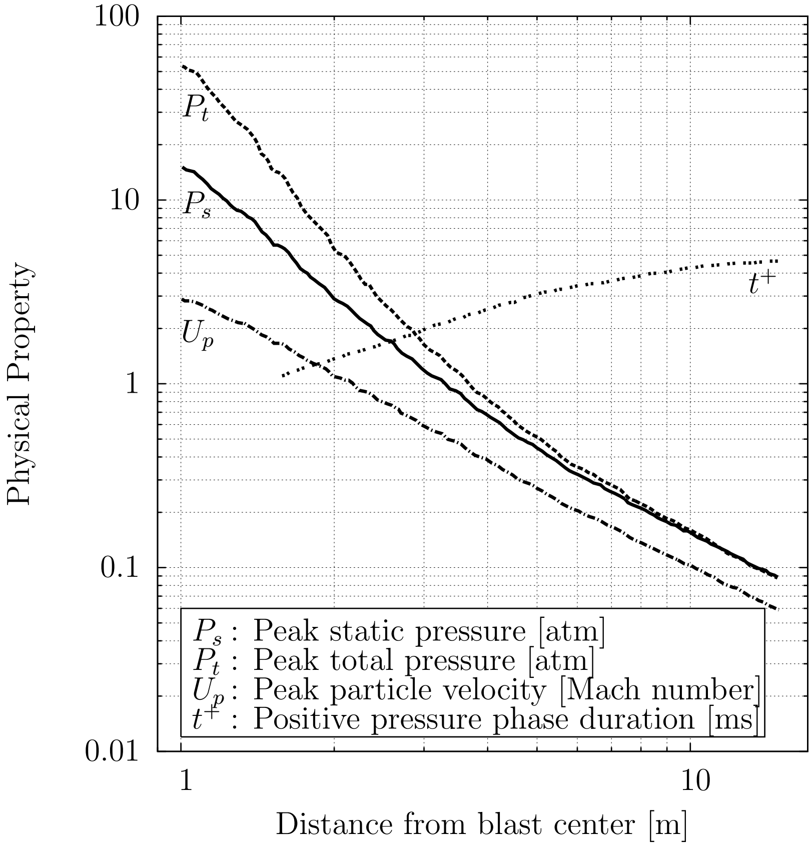

Figure B.1: Experimentally measured parameters of a blast generated by a 1 kg charge of TNT at 1 atm and 20°C. (Reproduced from Igra et. al. [32])

$$d_{eq} = \frac{d_{ref} \cdot W_{TNT}^{\frac{1}{3}}}{f_d} \tag{B.2}$$

$$f_t = f_d \left(\frac{C_{pr}}{C_{ref}} \right) = \left(\frac{P_{pr}}{P_{ref}} \right)^{\frac{1}{3}} \left(\frac{T_{pr}}{T_{ref}} \right)^{\frac{1}{3}} \tag{B.3}$$

Appendix C

Numerical Results

Below is a table containing the sum of all of the numerical results obtained. Contained is the numerical parameters, the fitted Friedlander equation parameters as well as the TNT charge equivalences. Additionally the final two columns contain the χ^2 parameter from the fitting of the Friedlander equation and whether the configuration was found to be successful in creating a Friedlander wave, indicated with a pass or fail.

Table C.1: Tabulated numerical results.

l/r	Fill %	x_{vent}	l_{vent}	α	t^+	P_s	W_{equiv} [kg]	d_{equiv} [m]	χ^2	P/F
3	0.10	n/a	n/a	1495.39	1.02E-003	3.18	0.52	1.69	92.59	P
3	0.20	n/a	n/a	2130.79	7.55E-004	5.70	0.22	1.01	254.83	P
3	0.30	n/a	n/a	2290.74	9.28E-004	6.18	0.56	1.32	400.96	F
3	0.40	n/a	n/a	1887.99	1.03E-003	6.76	0.83	1.46	204.45	F
3	0.50	n/a	n/a	2342.80	1.17E-003	8.88	1.67	1.64	280.64	F
3	0.60	n/a	n/a	2864.00	1.27E-003	10.92	3.35	1.90	407.77	F
3	0.70	n/a	n/a	3172.29	1.71E-003	12.26	9.63	2.58	645.23	F
5	0.10	n/a	n/a	1162.73	1.23E-003	3.30	0.96	2.04	122.60	P
5	0.30	n/a	n/a	1846.51	1.47E-003	6.27	2.23	2.09	544.87	F
5	0.40	n/a	n/a	1501.86	1.66E-003	7.20	3.60	2.34	249.23	F
5	0.50	n/a	n/a	1738.94	1.87E-003	9.13	7.10	2.62	265.66	F
5	0.60	n/a	n/a	2035.08	1.84E-003	11.16	10.54	2.75	640.52	F
6	0.10	0.50	0.10	1682.09	7.39E-004	3.13	0.20	1.23	170.61	P
6	0.20	0.50	0.10	2868.63	8.74E-004	5.46	0.33	1.18	348.83	P
7	0.10	n/a	n/a	941.47	1.56E-003	3.35	2.02	2.60	136.21	P
7	0.20	n/a	n/a	1588.15	1.42E-003	6.29	2.05	2.03	273.00	P
7	0.30	n/a	n/a	1542.56	1.99E-003	6.38	5.68	2.83	722.59	F

Table C.1: Continued.

l/r	Fill %	x_{vent}	l_{vent}	α	t^+	P_s	W_{equiv} [kg]	d_{equiv} [m]	χ^2	P/F
7	0.40	n/a	n/a	1200.62	2.28E-003	7.28	9.44	3.22	273.76	F
7	0.50	n/a	n/a	1442.10	2.41E-003	9.83	13.67	3.18	412.77	F
7	0.60	n/a	n/a	1762.08	2.54E-003	11.84	30.28	3.82	996.30	F
8	0.20	0.50	0.10	1798.02	1.17E-003	5.00	1.79	2.15	789.13	P
10	0.10	n/a	n/a	724.90	2.11E-003	3.40	5.12	3.52	126.22	P
10	0.15	0.30	0.10	1202.88	1.16E-003	3.62	1.41	2.22	168.37	P
10	0.15	0.50	0.10	1209.22	1.51E-003	3.69	3.27	2.92	505.33	P
10	0.15	n/a	n/a	419.24	4.21E-003	4.54	73.04	7.59	139.87	P
10	0.20	0.20	0.10	1059.21	9.81E-004	3.64	0.22	1.48	2671.81	F
10	0.20	0.20	0.20	343.15	8.37E-004	2.34	0.15	1.26	515.95	F
10	0.20	0.30	0.05	1037.23	1.21E-003	5.43	0.86	1.64	764.40	P
10	0.20	0.30	0.10	1181.07	1.04E-003	4.65	1.15	1.89	497.39	P
10	0.20	0.30	0.10	845.45	9.60E-004	4.65	0.90	1.74	480.52	F
10	0.20	0.35	0.20	3378.86	1.21E-003	4.60	1.76	2.18	612.54	F
10	0.20	0.35	0.25	264.20	4.30E-004	3.35	0.04	0.72	152.90	F
10	0.20	0.50	0.05	1426.46	1.46E-003	5.17	0.7	1.94	4404.87	P
10	0.20	0.50	0.10	1075.97	1.36E-003	4.23	2.28	2.43	538.70	P
10	0.20	0.50	0.10	1075.97	1.36E-003	4.23	2.28	2.43	538.70	P
10	0.20	0.50	0.15	1214.75	9.30E-004	3.72	0.78	1.80	671.82	F
10	0.20	0.50	0.20	1124.76	9.34E-004	3.36	0.44	1.56	599.34	F
10	0.20	0.55	0.05	1535.16	1.52E-003	5.60	1.81	2.04	825.97	P
10	0.20	0.55	0.10	1530.02	1.36E-003	4.94	2.79	2.50	794.27	P
10	0.20	0.55	0.15	1509.75	1.02E-003	4.46	1.01	1.83	798.91	F
10	0.20	0.55	0.20	2138.44	1.38E-003	4.14	0.75	1.70	768.14	F
10	0.20	0.60	0.05	1724.61	1.53E-003	5.89	1.94	2.05	1114.24	P
10	0.20	0.60	0.10	2075.17	1.50E-003	5.47	1.66	2.03	1007.42	P
10	0.20	0.60	0.15	2173.84	9.87E-004	5.02	1.08	1.81	1006.30	F
10	0.20	0.60	0.20	3422.44	1.55E-003	4.76	3.90	2.82	680.96	F
10	0.20	0.65	0.05	1857.86	1.57E-003	6.05	2.67	2.24	1091.46	F
10	0.20	0.65	0.10	2436.74	1.50E-003	5.73	1.76	2.01	747.67	F
10	0.20	0.65	0.15	2935.66	1.08E-003	5.40	0.61	1.46	492.98	F
10	0.20	0.65	0.20	3515.90	7.28E-004	5.26	0.46	1.35	628.38	F
10	0.20	0.70	0.05	1919.99	1.43E-003	6.15	2.06	2.04	648.89	P
10	0.20	0.70	0.10	2548.66	1.34E-003	5.91	1.30	1.79	486.35	F
10	0.20	0.70	0.15	2965.69	8.10E-004	5.67	0.28	1.08	535.00	F
10	0.20	0.70	0.20	4172.27	4.32E-004	5.59	0.04	0.58	723.09	F
10	0.20	n/a	n/a	1247.14	1.96E-003	6.41	5.41	2.79	255.26	P

Table C.1: Continued.

l/r	Fill %	x_{vent}	l_{vent}	α	t^+	P_s	W_{equiv} [kg]	d_{equiv} [m]	χ^2	P/F
10	0.25	0.50	0.10	1145.28	1.19E-003	5.73	0.88	1.59	2870.33	F
10	0.30	0.50	0.10	1068.79	1.13E-003	5.74	0.75	1.51	2671.81	F
10	0.30	n/a	n/a	1394.64	2.81E-003	6.46	15.98	3.99	647.23	F
10	0.35	0.50	0.10	-37.49	8.67E-004	6.41	0.47	1.23	1691.45	F
10	0.40	0.50	0.10	-1123.15	3.68E-004	8.00	0.03	0.48	1701.92	F
10	0.40	n/a	n/a	-511.36	9.76E-004	7.56	0.76	1.38	276.05	F
10	0.50	n/a	n/a	1086.04	3.47E-003	9.73	40.40	4.57	491.04	F
10	0.60	n/a	n/a	1465.19	3.54E-003	12.42	87.14	5.35	11624.84	F
12	0.10	n/a	n/a	582.49	2.55E-003	3.41	9.11	4.27	209.93	P
12	0.15	0.50	0.10	1419.69	1.38E-003	4.14	0.74	1.69	471.72	P
12	0.15	n/a	n/a	686.97	2.48E-003	4.93	16.73	4.54	288.81	P
12	0.20	0.50	0.10	1403.92	1.42E-003	4.88	3.09	2.59	701.59	P
12	0.20	n/a	n/a	965.62	2.56E-003	6.51	12.18	3.63	540.87	P
14	0.15	0.50	0.10	1512.47	1.82E-003	4.08	1.71	2.25	249.23	P
14	0.20	0.50	0.10	992.79	1.41E-003	4.39	2.62	2.53	340.92	P
15	0.15	n/a	n/a	597.02	2.99E-003	4.94	29.47	5.48	298.64	P
15	0.20	n/a	n/a	839.98	3.10E-003	6.50	21.80	4.41	466.09	P
15	0.30	n/a	n/a	806.67	4.44E-003	6.53	64.28	6.31	1878.34	F
15	0.40	n/a	n/a	680.00	5.10E-003	7.74	86.59	6.62	523.73	F
15	0.50	n/a	n/a	768.79	5.21E-003	10.09	140.99	6.83	959.29	F
18	0.10	n/a	n/a	456.73	3.40E-003	3.38	21.33	5.69	222.72	P
18	0.15	n/a	n/a	535.15	3.46E-003	5.03	46.56	6.35	346.77	P
18	0.20	n/a	n/a	735.35	3.72E-003	6.51	37.65	5.29	518.05	P
20	20	0.50	0.10	-2551.89	3.55E-004	3.70	0.04	0.69	436.15	F
24	0.04	n/a	n/a	394.44	2.69E-003	1.76	3.20	3.97	137.37	P
24	0.05	n/a	n/a	350.77	3.27E-003	2.02	5.38	4.48	124.14	P
24	0.09	n/a	n/a	366.08	4.10E-003	3.09	33.32	6.80	216.31	P
24	0.10	n/a	n/a	360.27	4.45E-003	3.35	46.82	7.42	431.05	P
24	0.15	n/a	n/a	424.21	4.58E-003	5.11	110.11	8.43	347.46	P
24	0.20	n/a	n/a	629.88	5.86E-003	6.48	146.23	8.33	484.42	P

Appendix D

Sample Mechanical Calculations

D.1 Hoop Stress

The transverse hoop stress, σ_t, at a given radius r between the inner and outer radii (r_i and r_o) of a vessel with an internal pressure of P_i and an external pressure P_o is described by equation (D.1) [35]. Note that the greatest stress will always be at the minimum radius of curvature, r_i.

$$\sigma_t = \frac{P_i r_i^2 - P_o 0 r_o^2 - \frac{r_i^2 r_i^2 (P_o - P_i)}{r^2}}{r_o^2 - r_i^2} \tag{D.1}$$

Given an internal pressure of 87.5 atmospheres, representing a reflected detonation wave we find that the peak hoop stress in the material of the shock tube is $\sigma_{tmax} = 29.2$ MPa. Given that the shock tube is constructed of AISI 1026 steel tube which has a tensile yield strength of 240 MPa, the factor of safety on the hoop stress of the tube is of $n_{tube} = 8.2$.

D.2 Clamps

The selected clamps have are designed to hold 75 KN of force. With ten clamps per interface and a shock tube design loading P_{load} of 87.5 ATM applied over the shock tube's inner area, A_{st}, we have that the factor of safety on the clamps,n_{clamps}, is given by ;

$$n_{clamps} = \frac{75 \text{ KN } * 10}{P_{load} * A_{st}} = \frac{75 \text{ KN } * 10}{87.5 \text{ ATM } * 0.07296 \text{ m}^2} = 1.16 \tag{D.2}$$

While the safety factor is low, the design assumption are very conservative. Due to the hemispherically expanding nature of the detonation wave after ignition, only a small fraction of the back plate will be loaded with detonation over-pressures at one time. Additionally, reflected detonation pressures will only form at the edge of the plate where the detonation will impinge on the tube wall. Thus this is an acceptable value.

D.3 Pressure Plug Bolt Strength

The tensile stress area for a screw is given by equation D.3 (taken from the ISO 898 standard), where D is the major diameter of the thread and p is the screw pitch. Each pressure sensor port has a loaded area of 106 mm^2 and is exposed to 965 N under the design pressure. Each port is bolted to the shock tube by 8 M5x0.8 bolts made of zinc plated steel, under the given loading conditions the bolts would be subjected to a stress of 8.5 MPA, leading to a safety factor of approximately 16 assuming a conservative yield strength of 140 MPa.

Note that to ensure that the threaded shear area is at least twice that of the tensile area, the bolts must extend 4 mm into the body of the shock tube, as calculated using equation D.4. This ensures that the bolts will not fail by shearing of the threads.

$$A_t = \frac{\pi}{4}(D - 0.938194 \cdot p)^2 \tag{D.3}$$

$$L_{e(min)} = \frac{2A_T}{0.5\pi(D - 0.64952)P} \tag{D.4}$$

D.4 Plate in Bending

The design criteria for the loading of the back plate is not based on the yielding of the material, instead a maximum displacement of 1 mm at the center of the plate is imposed. Note that this criteria is much more stringent and thus the stresses in the back plate are well below yield.

For a flat circular plate loaded with a uniform pressure P in PSI, simply restrained at its edge, the maximum deflection at the center of the plate is given by equation D.5 [36] where r is the radius of the plate, D is the plate constant defined by equation D.6, and ν is the Poisson ratio of the material. Given the chosen chosen material of AISI 1020 steel the back plate of the tube must be 25.4 mm (1 in) thick to undergo at most 1 mm of deflection at its center under the design loading.

$$Y_c = \frac{P \cdot r^4}{64D} \cdot \frac{5+\nu}{1+\nu} \tag{D.5}$$

Where,

$$D = E\frac{t_{plate}^2}{12\left(1-\nu^2\right)} \tag{D.6}$$

D.5 Weld Strength

The support plates to which the clamps are mounted are welded to the shock tube along both sides of the plate that are parallel to the axis of the shock tube, such that the welds are loaded in shear when pressure is applied to the back plate of the shock tube. Each weld is a symmetric fillet weld covering the entire height of the mounting plates (0.375 in). The greatest shear stress in the weld, found at the minimum throat area of the weld, is described by equation D.7, where h is the thickness of the mounting plate and l is the length of the weld.

The shortest welded edges are those on the hook support plates, with a length of 1.97 in (50 mm). Under the loading discussed above and with a total of twenty welds retaining the mounting plates, each weld will be subjected to a shear stress of 96 MPa. This stress value is well below the minimum yield strength for E60 electrodes which is of 345 MPa. Note that for welded joints in shear the stress should be kept below 40% of the yield strength of the base material. Since the shock tube is constructed of AISI 1026 steel with a yield stress of 240 MPa, this criteria is also met. [35]

$$\tau_w = \frac{F}{0.707hl} \tag{D.7}$$

Appendix E

Technical Drawings

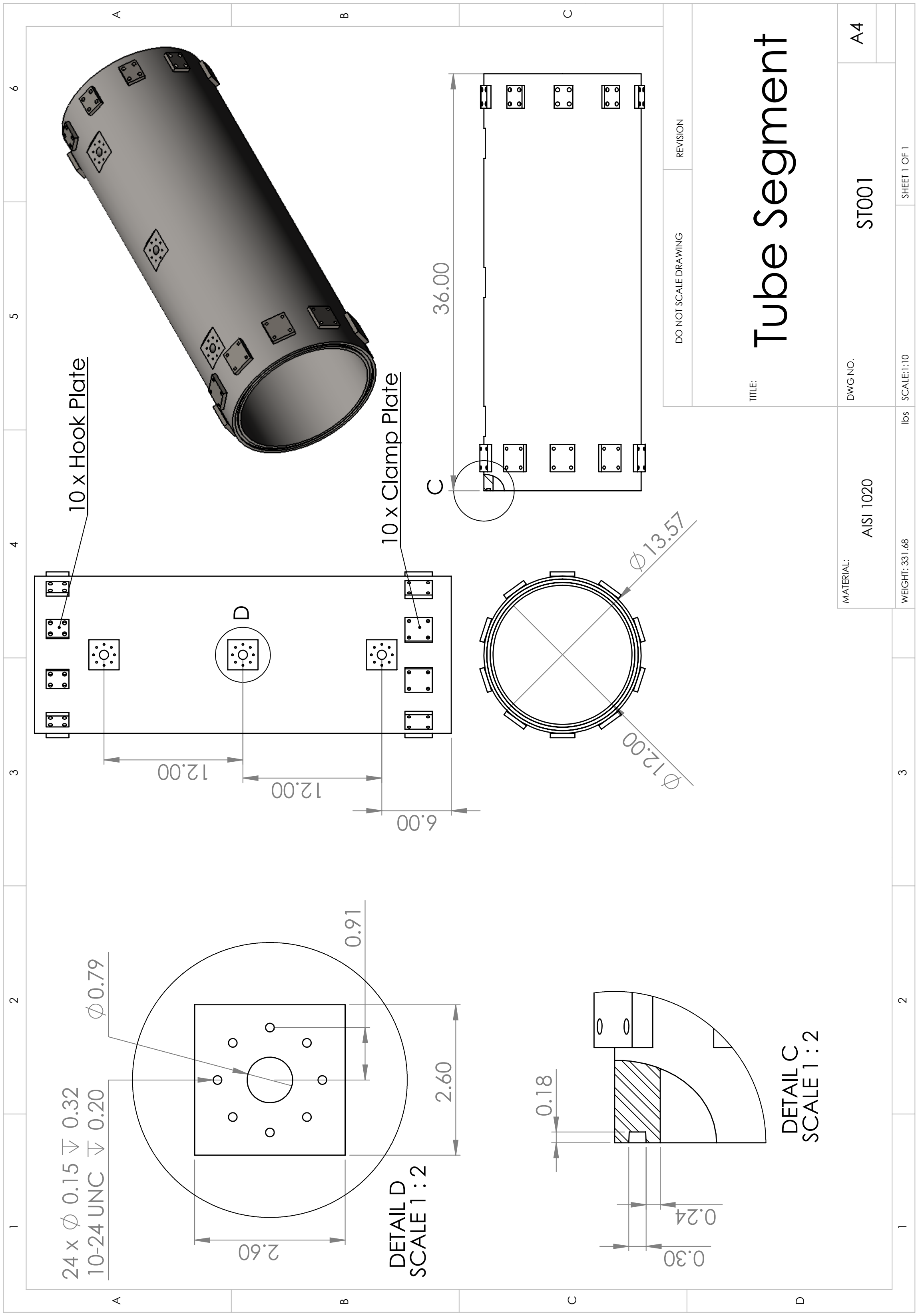
Tube Segment
TITLE:
DO NOT SCALE DRAWING
REVISION
DWG NO.
ST001
A4
MATERIAL:
AISI 1020
WEIGHT: 331.68 lbs
SCALE:1:10
SHEET 1 OF 1
10 x Hook Plate
10 x Clamp Plate
36.00
C
D
Ø13.57
Ø12.00
12.00
12.00
6.00
Ø0.79
0.91
2.60
2.60
24 x Ø 0.15 ↧ 0.32
10-24 UNC ↧ 0.20
DETAIL D
SCALE 1 : 2
0.18
0.24
0.30
DETAIL C
SCALE 1 : 2
A
B
C
D
1
2
3
4
5
6

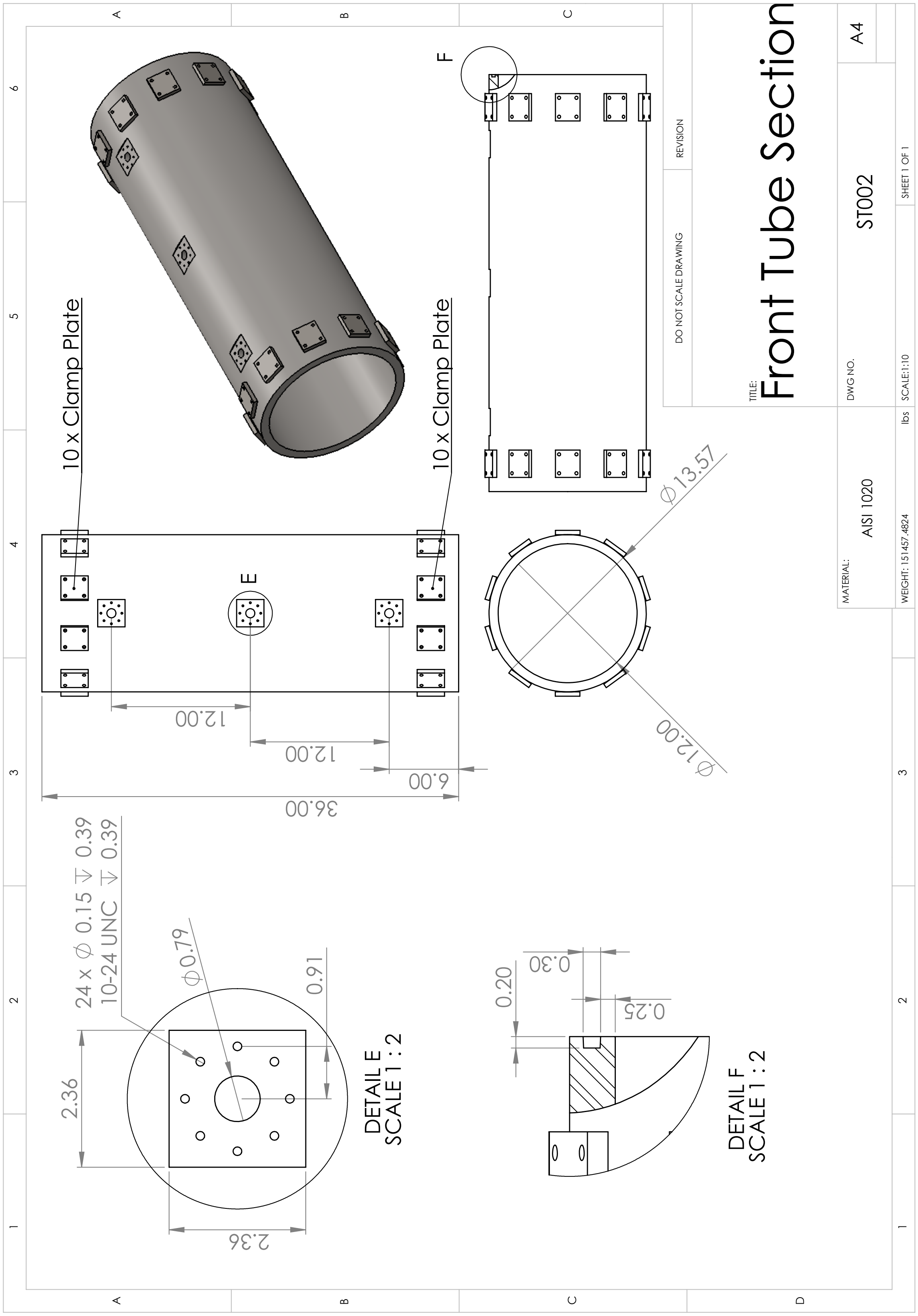
10 x Clamp Plate
10 x Clamp Plate
F
E
12.00
12.00
6.00
36.00
⌀13.57
⌀12.00
24 x ⌀ 0.15 ↧ 0.39
10-24 UNC ↧ 0.39
⌀0.79
0.91
2.36
2.36
DETAIL E
SCALE 1 : 2
0.30
0.20
0.25
DETAIL F
SCALE 1 : 2
DO NOT SCALE DRAWING
REVISION
TITLE:
Front Tube Section
DWG NO.
ST002
A4
MATERIAL:
AISI 1020
WEIGHT: 151457.4824
lbs
SCALE:1:10
SHEET 1 OF 1
A
B
C
D
1
2
3
4
5
6

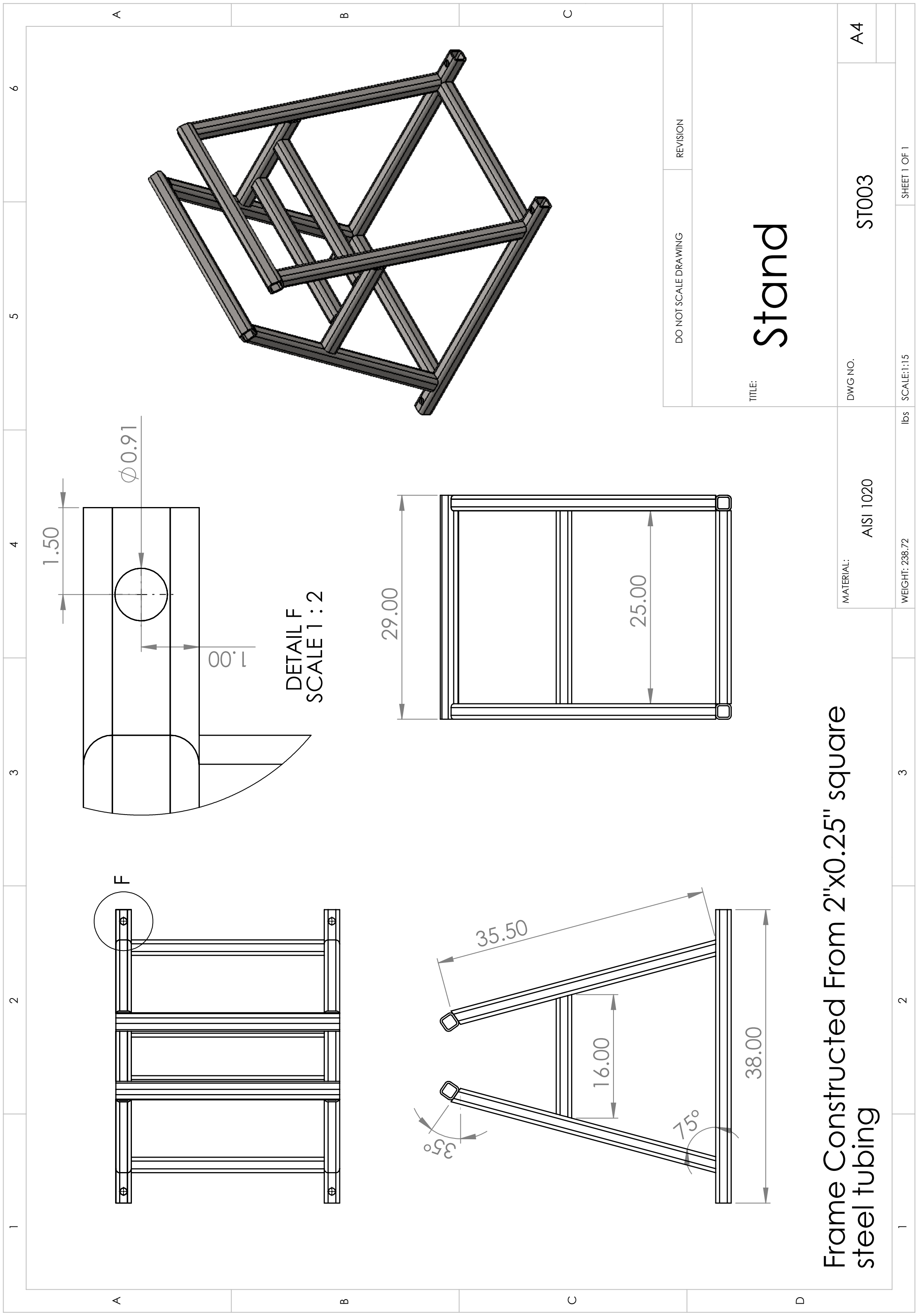
Frame Constructed From 2"x0.25" square steel tubing

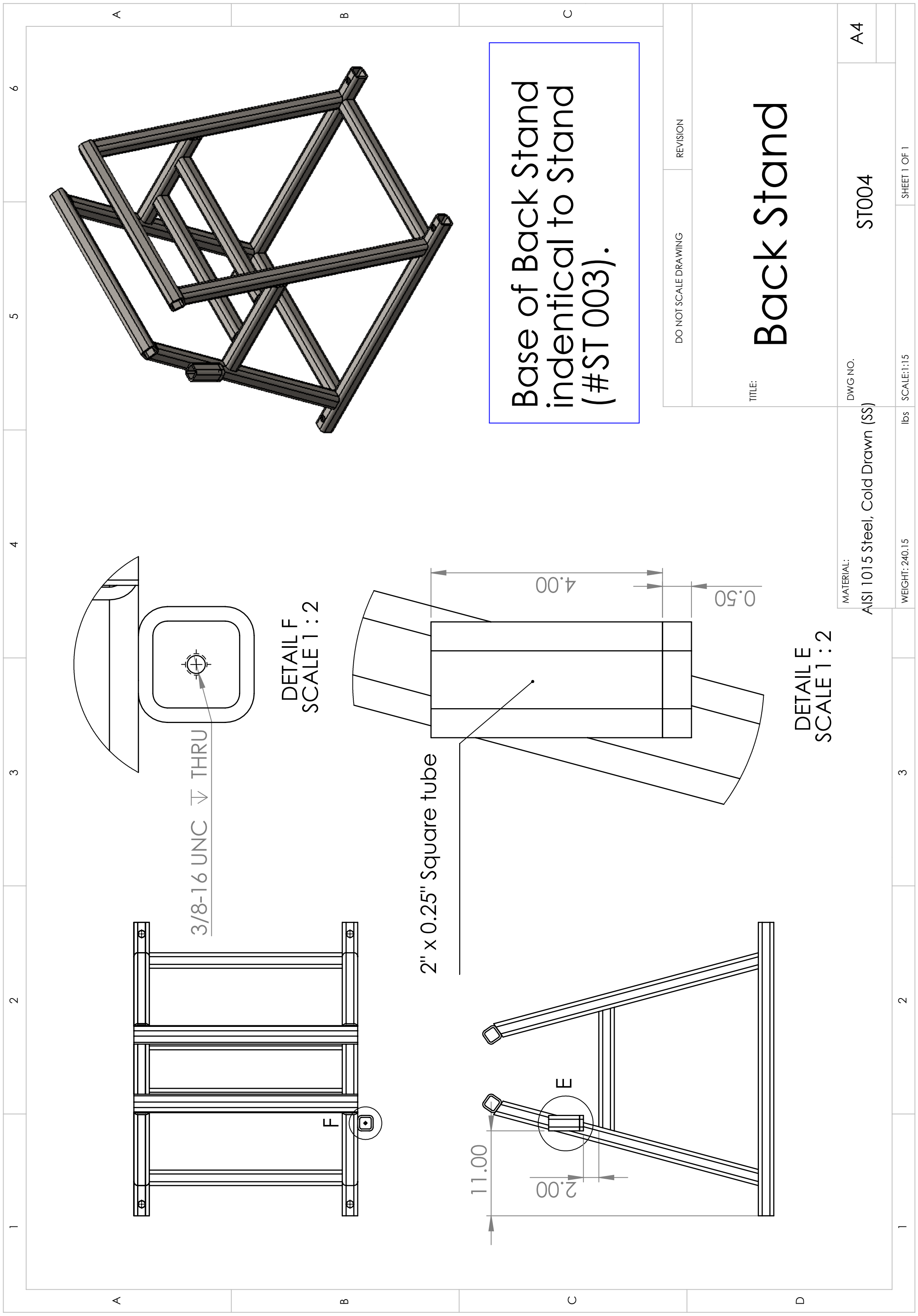
Base of Back Stand
indentical to Stand
(#ST 003).
DETAIL F
SCALE 1 : 2
DETAIL E
SCALE 1 : 2
3/8-16 UNC ⊽ THRU
2" x 0.25" Square tube
4.00
0.50
11.00
2.00
E
F
DO NOT SCALE DRAWING
REVISION
TITLE:
Back Stand
DWG NO.
ST004
A4
MATERIAL:
AISI 1015 Steel, Cold Drawn (SS)
WEIGHT: 240.15
lbs
SCALE:1:15
SHEET 1 OF 1
A
B
C
D
1
2
3
4
5
6

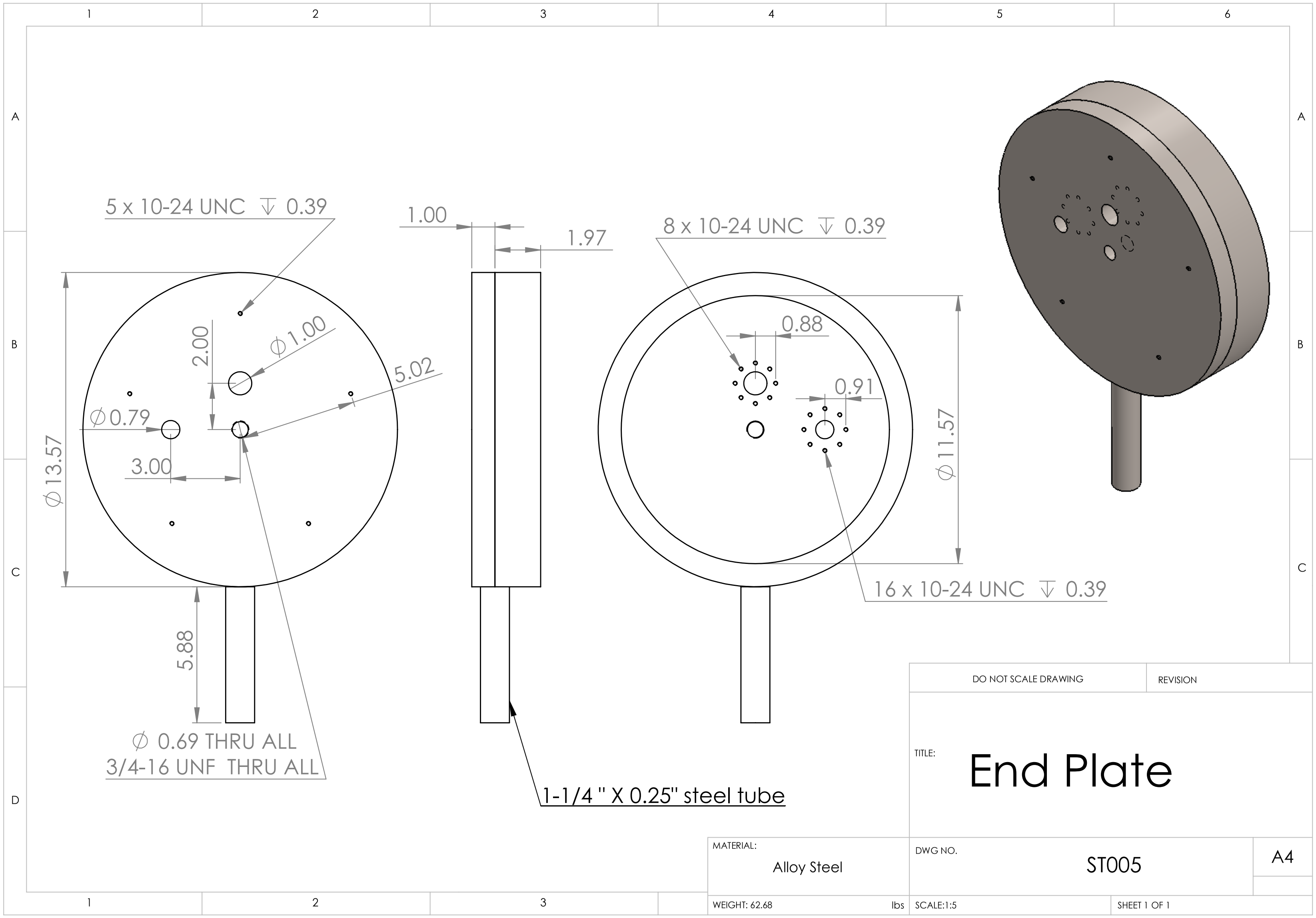
5 x 10-24 UNC ↧ 0.39
1.00
1.97
8 x 10-24 UNC ↧ 0.39
2.00
∅1.00
5.02
0.88
0.91
∅0.79
3.00
∅13.57
∅11.57
16 x 10-24 UNC ↧ 0.39
5.88
∅ 0.69 THRU ALL
3/4-16 UNF THRU ALL
1-1/4 " X 0.25" steel tube
DO NOT SCALE DRAWING
REVISION
TITLE:
End Plate
MATERIAL:
Alloy Steel
DWG NO.
ST005
A4
WEIGHT: 62.68
lbs
SCALE:1:5
SHEET 1 OF 1
1
2
3
4
5
6
A
B
C
D

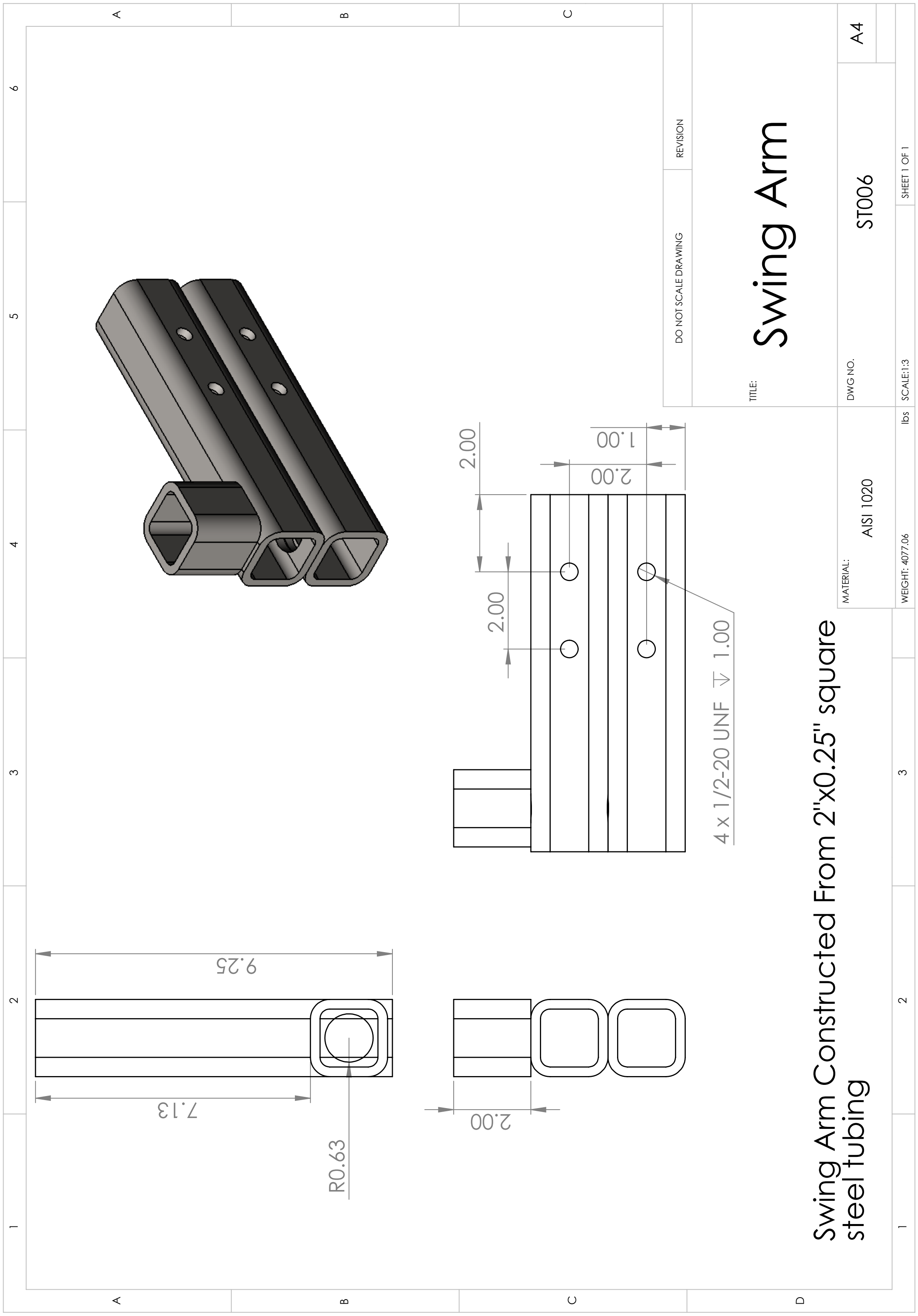
Swing Arm Constructed From 2'x0.25'' square steel tubing
9.25
7.13
R0.63
2.00
2.00
2.00
2.00
1.00
4 x 1/2-20 UNF ↧ 1.00
DO NOT SCALE DRAWING
REVISION
TITLE:
Swing Arm
DWG NO.
ST006
A4
MATERIAL:
AISI 1020
WEIGHT: 4077.06 lbs
SCALE:1:3
SHEET 1 OF 1
A
B
C
D
1
2
3
4
5
6

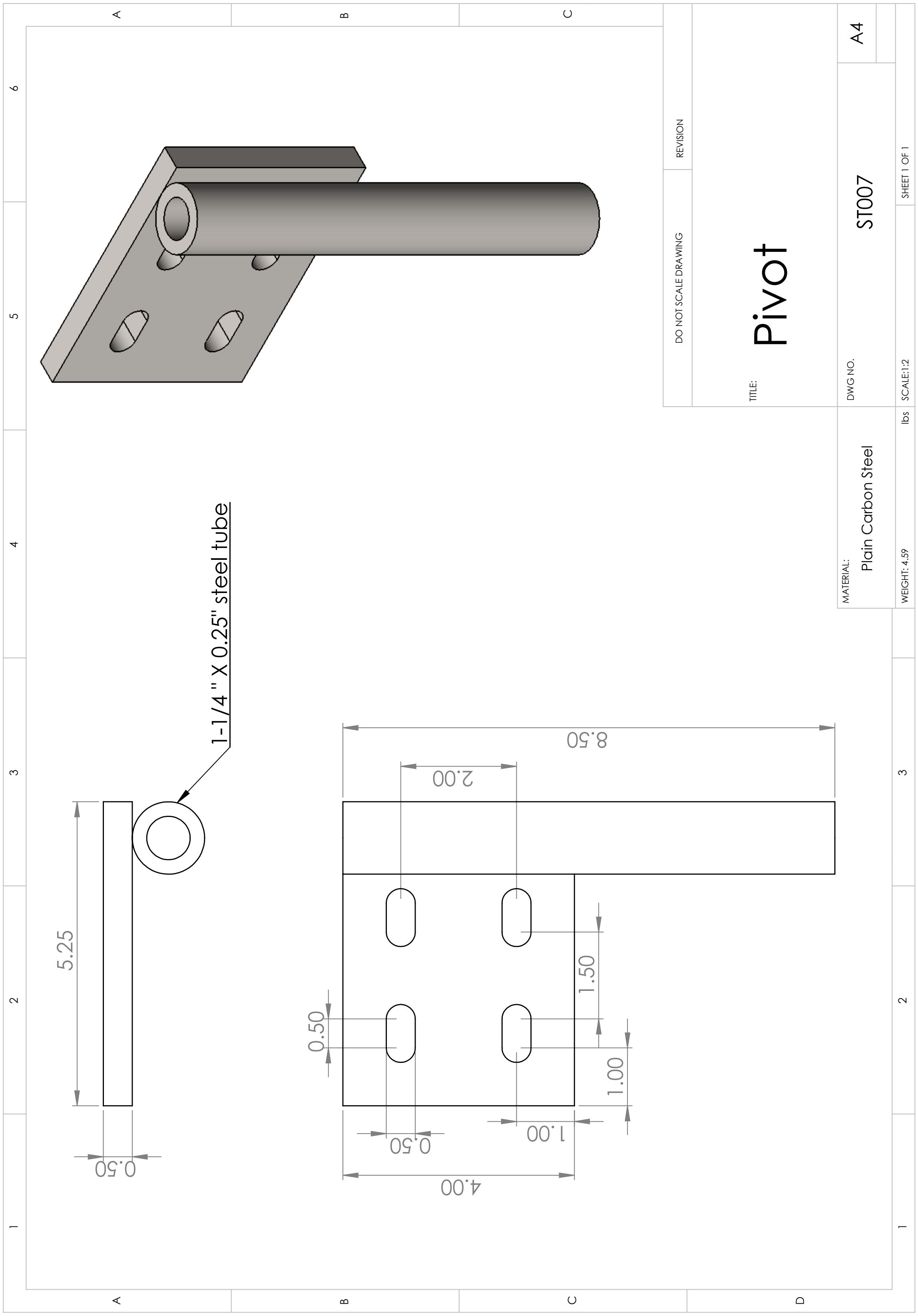
1-1/4 " X 0.25" steel tube
5.25
0.50
8.50
2.00
1.50
0.50
1.00
1.00
0.50
4.00
DO NOT SCALE DRAWING
REVISION
TITLE:
Pivot
DWG NO.
ST007
A4
SCALE:1:2
SHEET 1 OF 1
MATERIAL:
Plain Carbon Steel
WEIGHT: 4.59
lbs

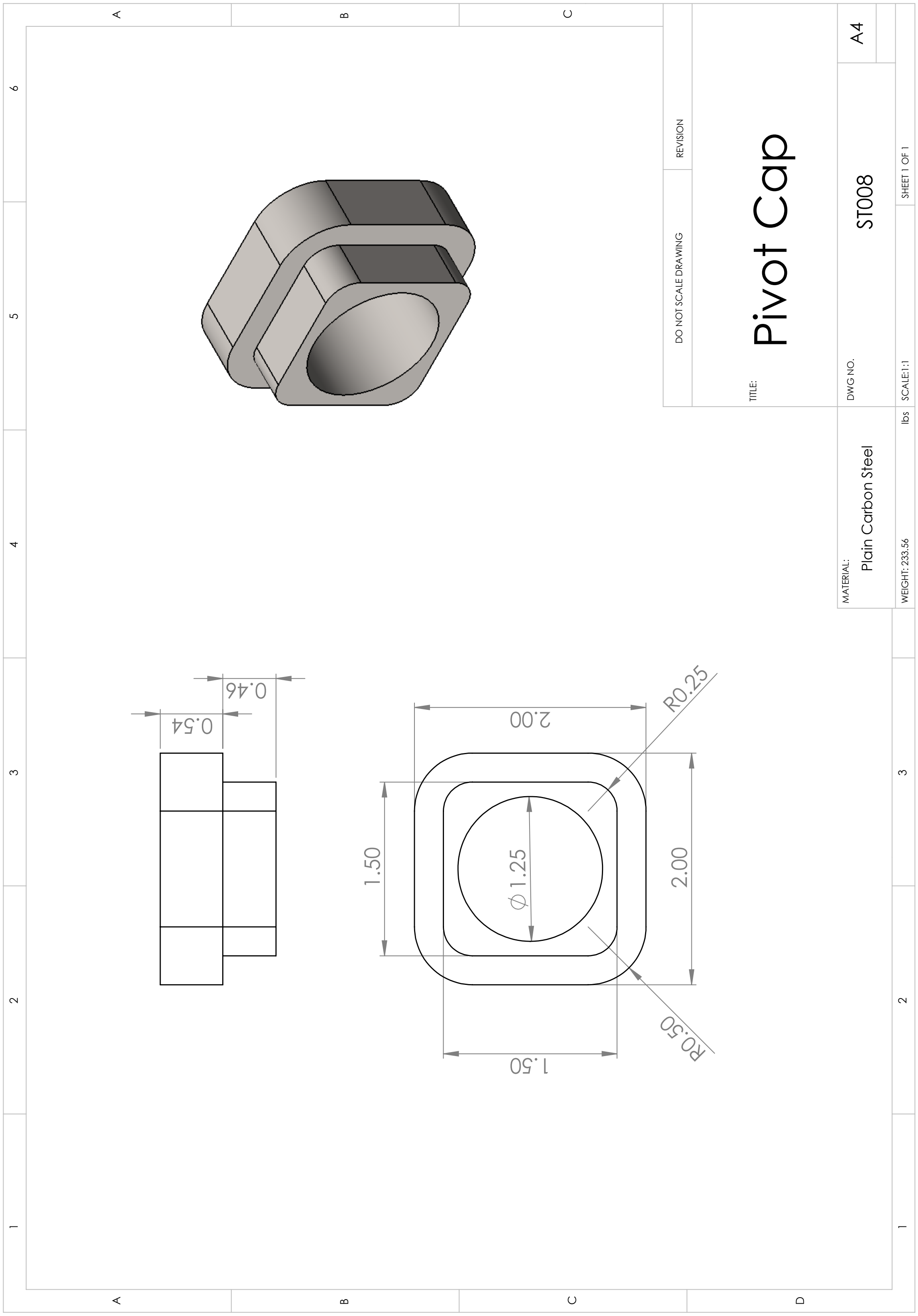

Pivot Cap
ST008
A4
REVISION
DO NOT SCALE DRAWING
TITLE:
DWG NO.
SCALE:1:1
SHEET 1 OF 1
MATERIAL:
Plain Carbon Steel
WEIGHT: 233.56
lbs
0.46
0.54
2.00
R0.25
1.50
⌀1.25
2.00
1.50
R0.50
A
B
C
D
1
2
3
4
5
6

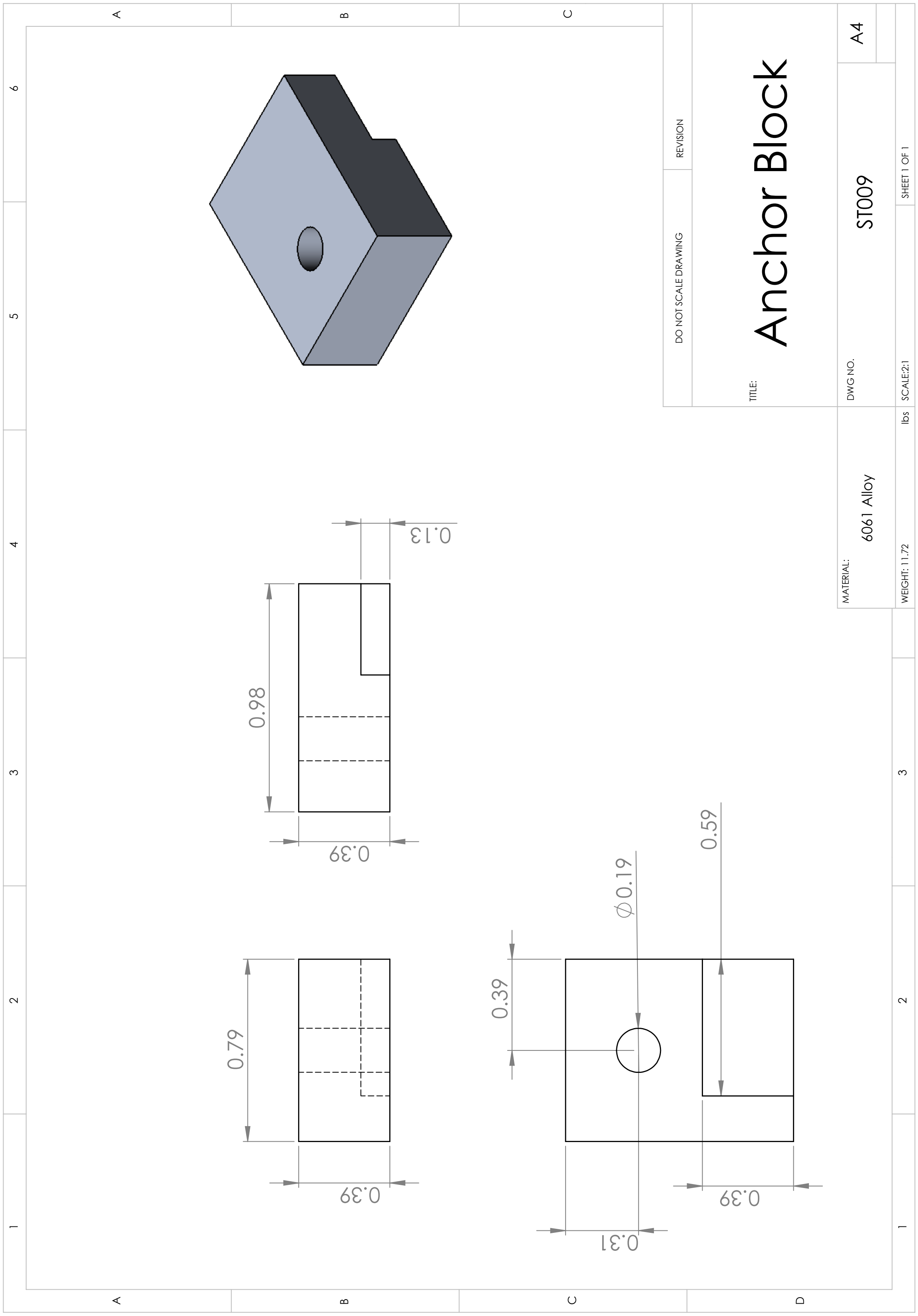
DO NOT SCALE DRAWING
REVISION
TITLE:
Anchor Block
DWG NO.
ST009
A4
SCALE:2:1
SHEET 1 OF 1
MATERIAL:
6061 Alloy
WEIGHT: 11.72
lbs
0.13
0.98
0.39
0.79
0.39
⌀0.19
0.59
0.39
0.39
0.31
A
B
C
D
1
2
3
4
5
6

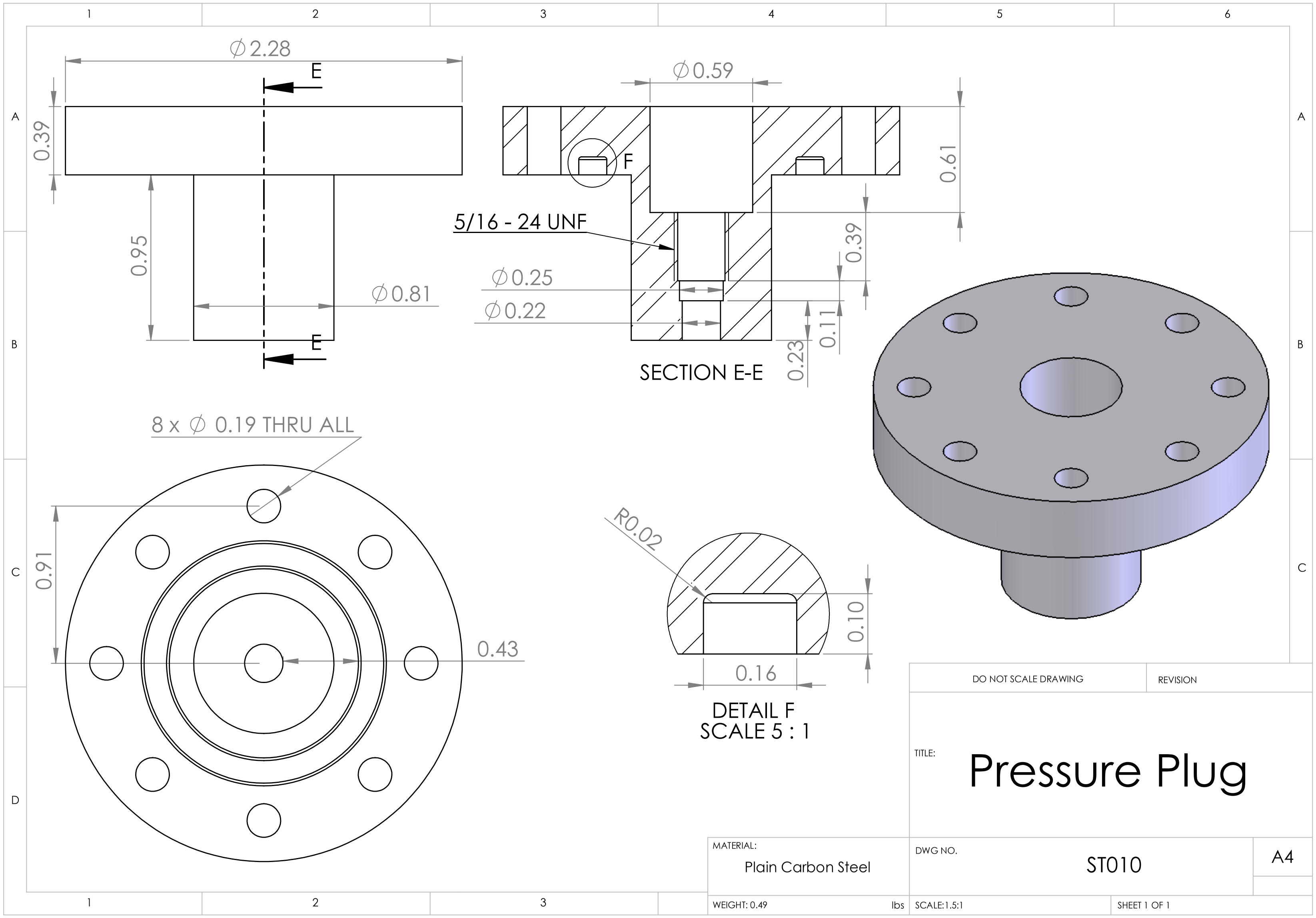
⌀2.28
E
0.39
0.95
⌀0.81
E
⌀0.59
F
0.61
5/16 - 24 UNF
0.39
⌀0.25
⌀0.22
0.11
0.23
SECTION E-E
8 x ⌀ 0.19 THRU ALL
0.91
0.43
R0.02
0.10
0.16
DETAIL F
SCALE 5 : 1
DO NOT SCALE DRAWING
REVISION
TITLE:
Pressure Plug
MATERIAL:
Plain Carbon Steel
DWG NO.
ST010
A4
WEIGHT: 0.49
lbs
SCALE:1.5:1
SHEET 1 OF 1
1
2
3
4
5
6
A
B
C
D

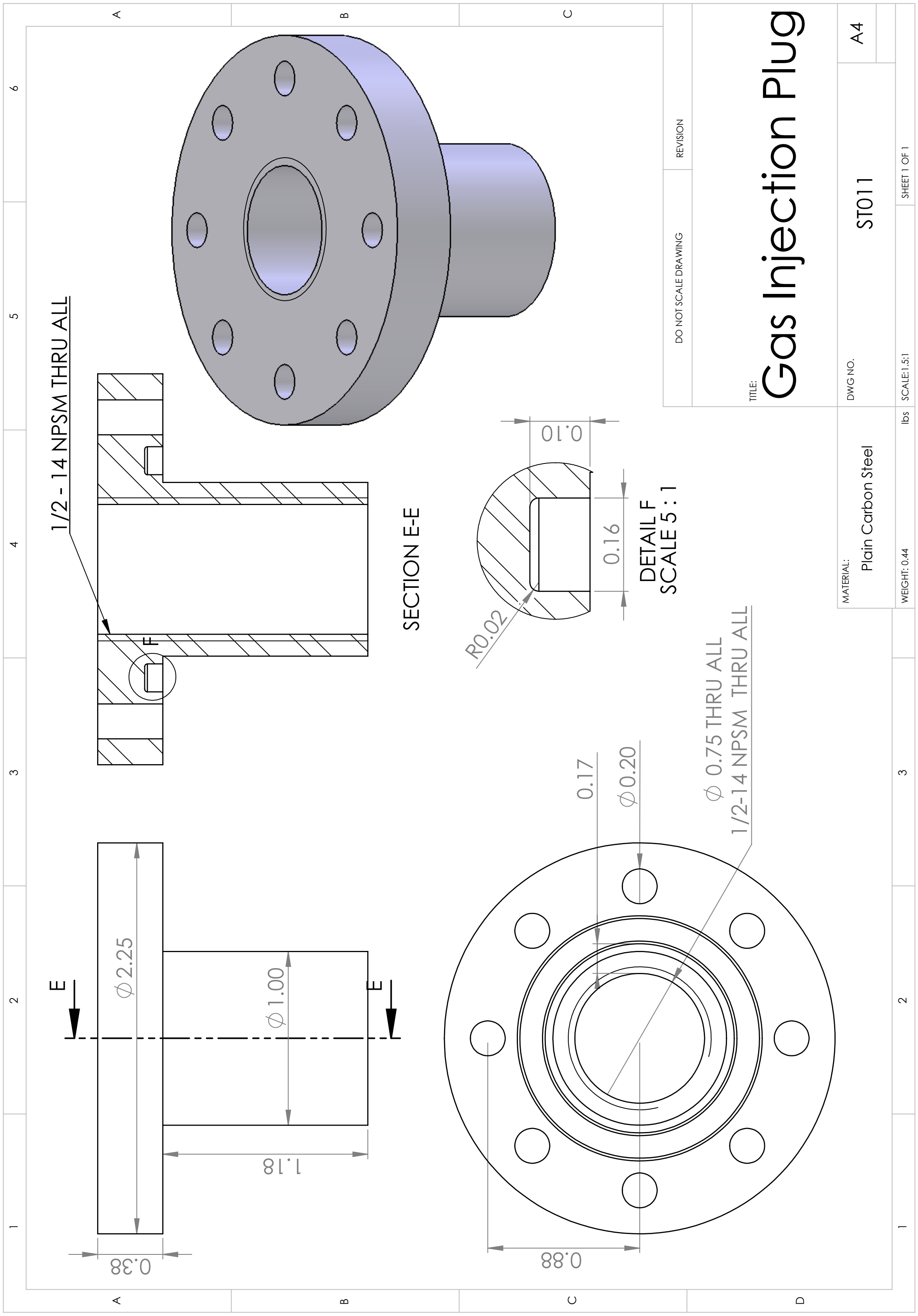
Gas Injection Plug
TITLE:
DO NOT SCALE DRAWING
REVISION
DWG NO.
ST011
A4
MATERIAL:
Plain Carbon Steel
WEIGHT: 0.44
lbs
SCALE:1.5:1
SHEET 1 OF 1
1/2 - 14 NPSM THRU ALL
SECTION E-E
F
E
E
0.10
0.16
R0.02
DETAIL F
SCALE 5 : 1
0.17
⌀0.20
⌀ 0.75 THRU ALL
1/2-14 NPSM THRU ALL
⌀2.25
⌀1.00
1.18
0.38
0.88

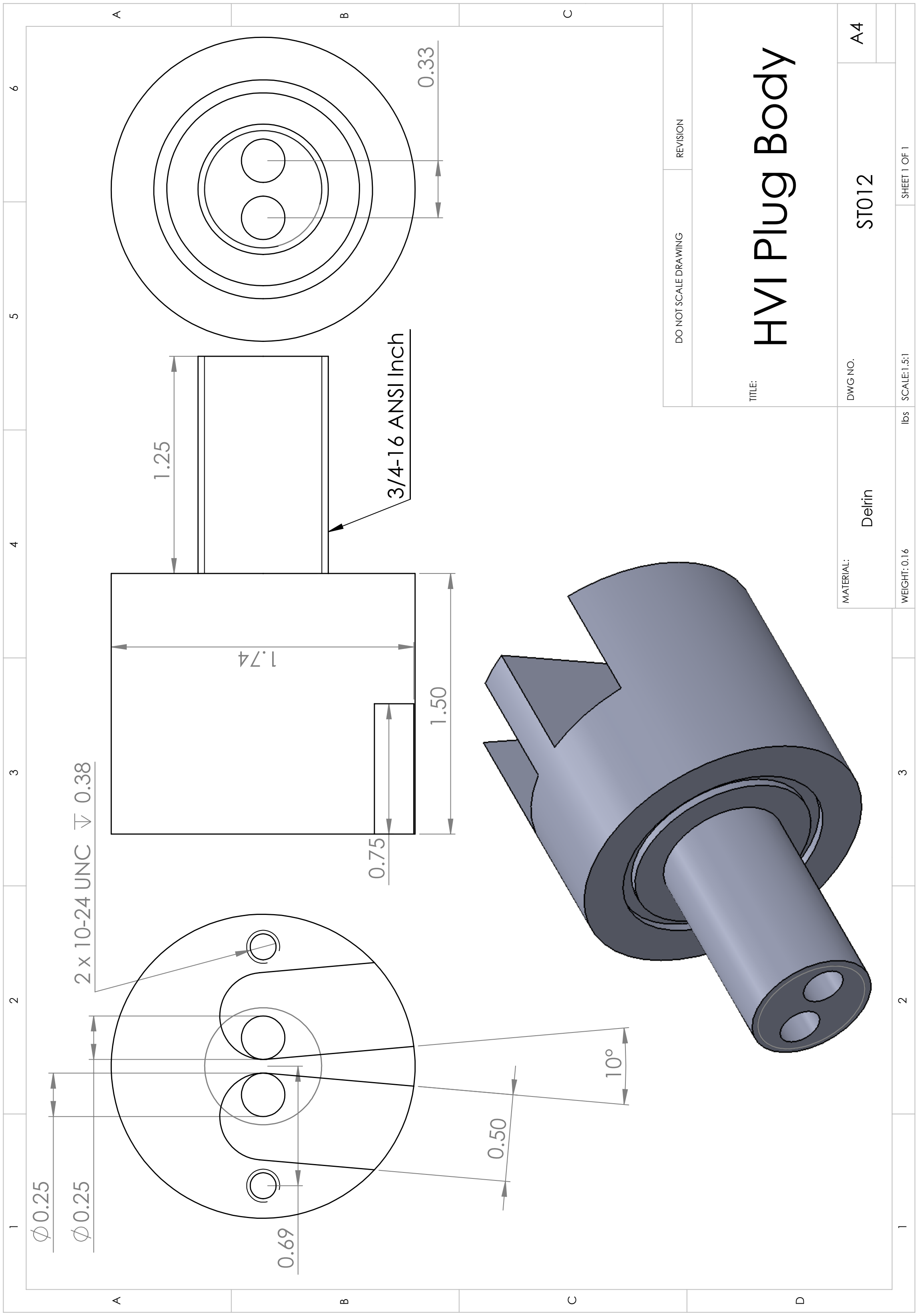
HVI Plug Body
TITLE:
DO NOT SCALE DRAWING
REVISION
DWG NO.
ST012
A4
MATERIAL:
Delrin
WEIGHT: 0.16
lbs
SCALE:1.5:1
SHEET 1 OF 1
0.33
1.25
3/4-16 ANSI Inch
1.74
1.50
0.75
2 x 10-24 UNC ↧ 0.38
10°
0.50
⌀0.25
⌀0.25
0.69
A
B
C
D
1
2
3
4
5
6

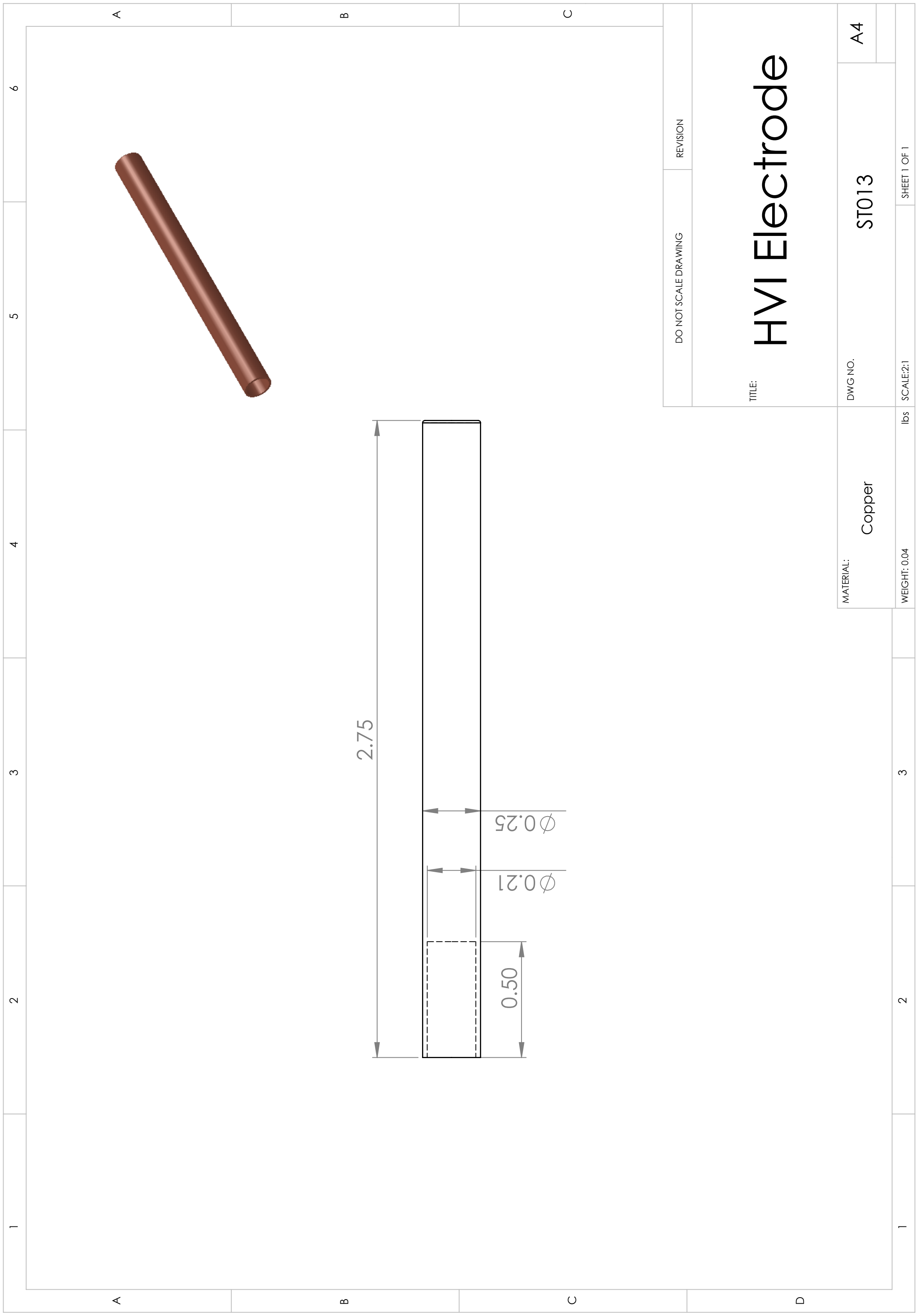
HVI Electrode
TITLE:
DWG NO.
ST013
A4
REVISION
DO NOT SCALE DRAWING
MATERIAL:
Copper
WEIGHT: 0.04 lbs
SCALE:2:1
SHEET 1 OF 1
2.75
Ø0.25
Ø0.21
0.50
A
B
C
D
1
2
3
4
5
6

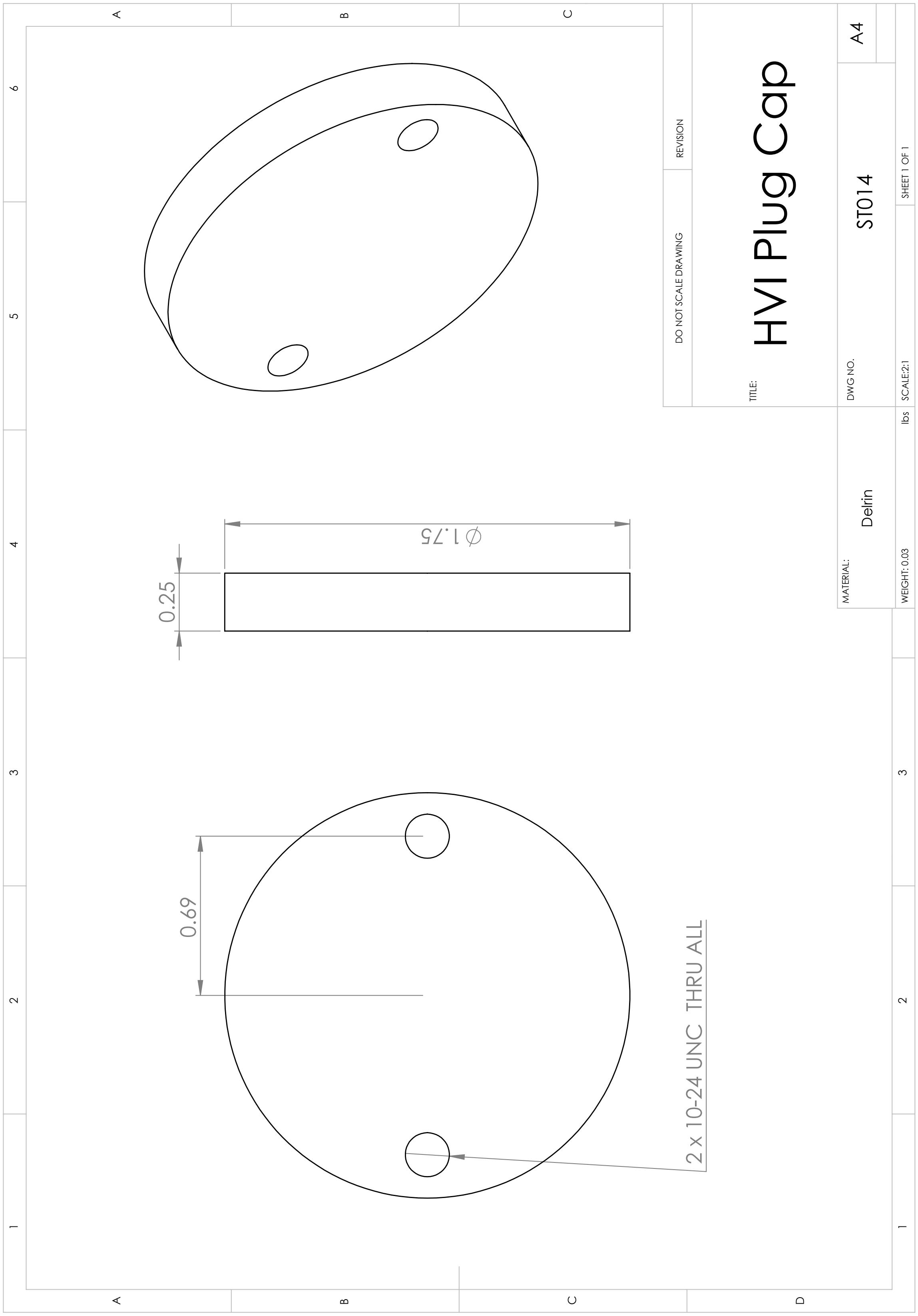
REVISION
DO NOT SCALE DRAWING
TITLE:
HVI Plug Cap
A4
DWG NO.
ST014
SHEET 1 OF 1
SCALE:2:1
MATERIAL:
Delrin
WEIGHT: 0.03
lbs
Ø1.75
0.25
0.69
2 x 10-24 UNC THRU ALL
A
B
C
D
1
2
3
4
5
6

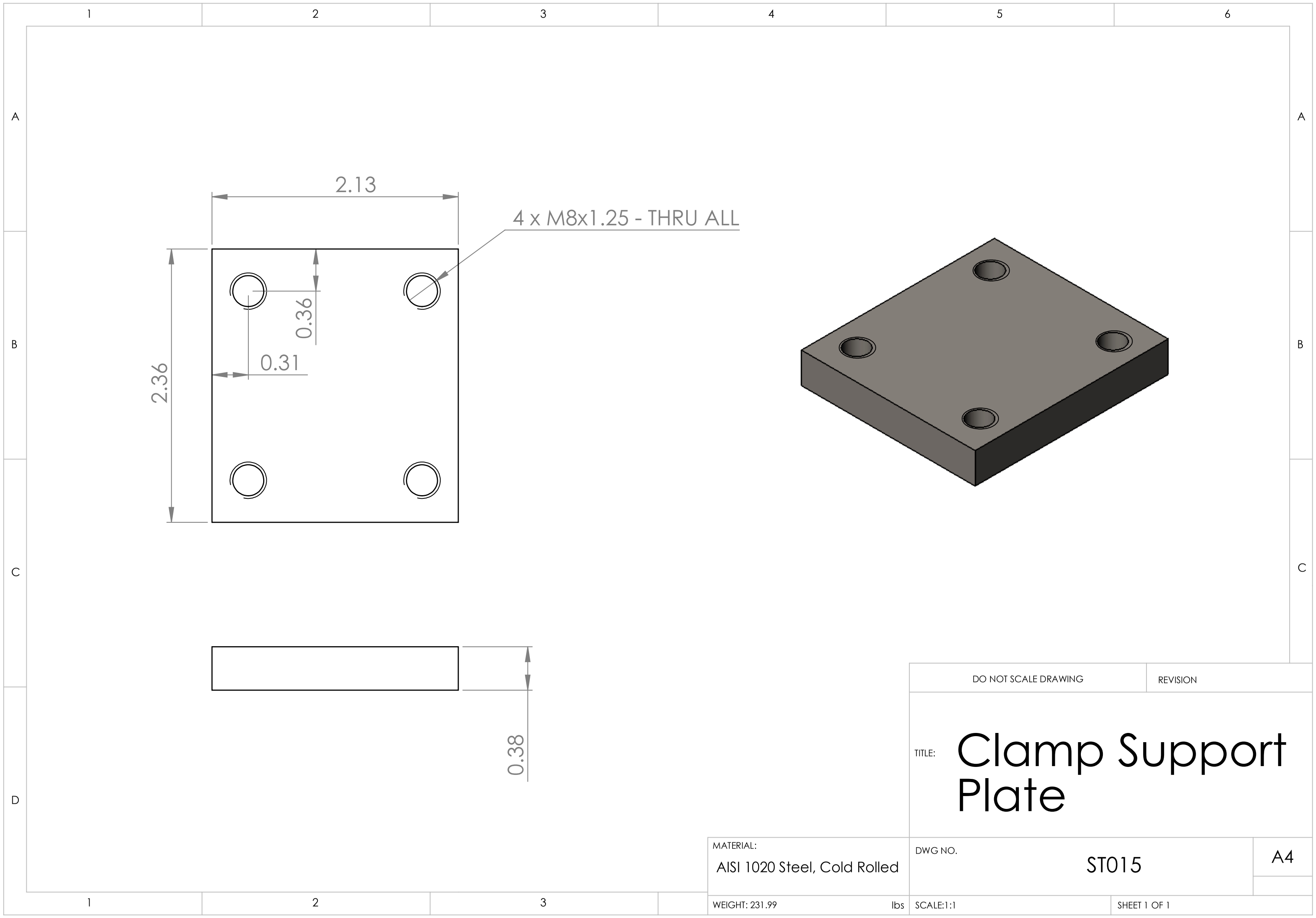

1
2
3
4
5
6
A
B
C
D
2.13
4 x M8x1.25 - THRU ALL
0.36
0.31
2.36
0.38
DO NOT SCALE DRAWING
REVISION
TITLE:
Clamp Support Plate
MATERIAL:
AISI 1020 Steel, Cold Rolled
DWG NO.
ST015
A4
WEIGHT: 231.99
lbs
SCALE:1:1
SHEET 1 OF 1

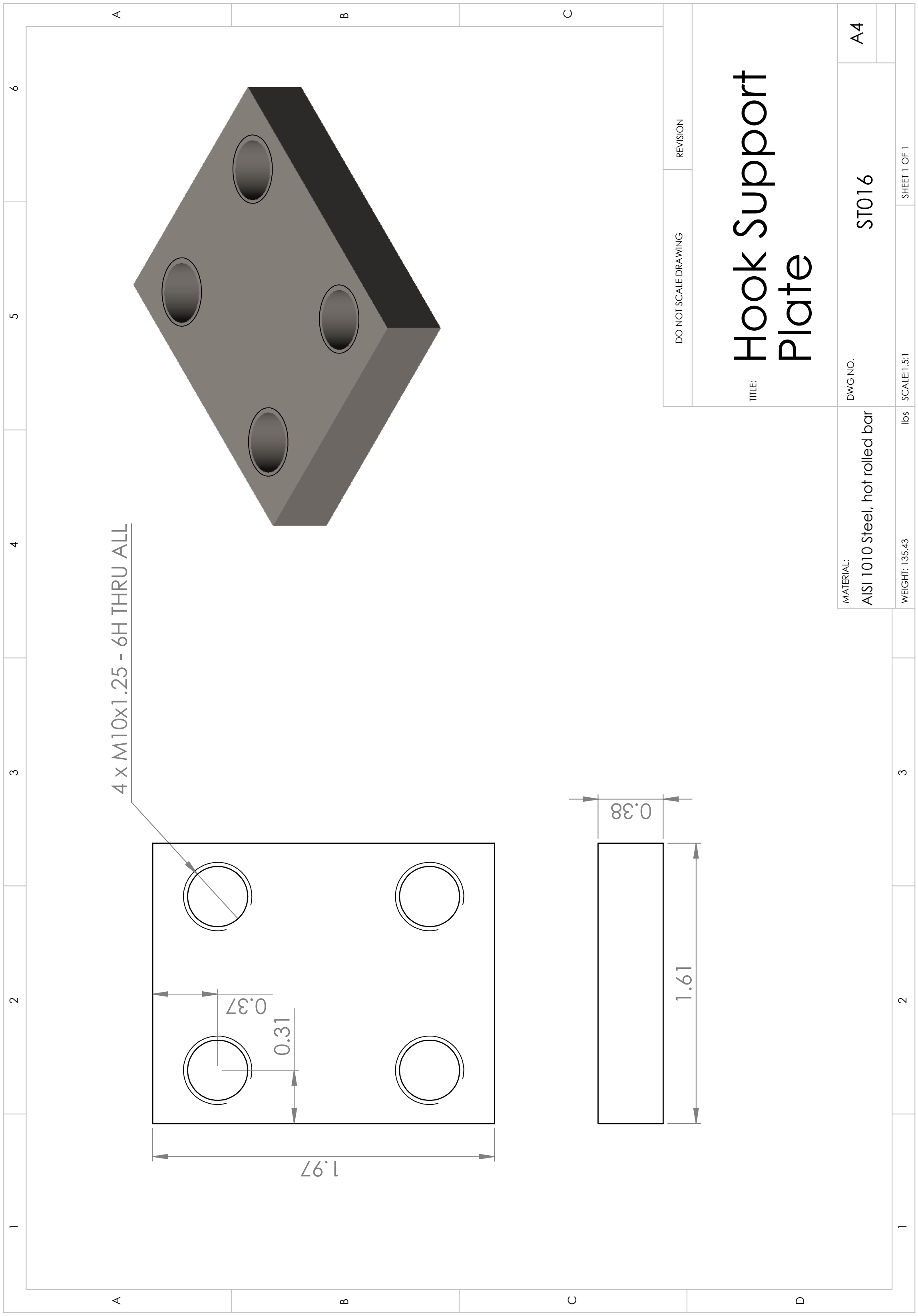
4 x M10x1.25 - 6H THRU ALL
0.38
1.61
0.37
0.31
1.97
DO NOT SCALE DRAWING
REVISION
TITLE:
Hook Support Plate
DWG NO.
ST016
A4
MATERIAL:
AISI 1010 Steel, hot rolled bar
WEIGHT: 135.43 lbs
SCALE:1.5:1
SHEET 1 OF 1

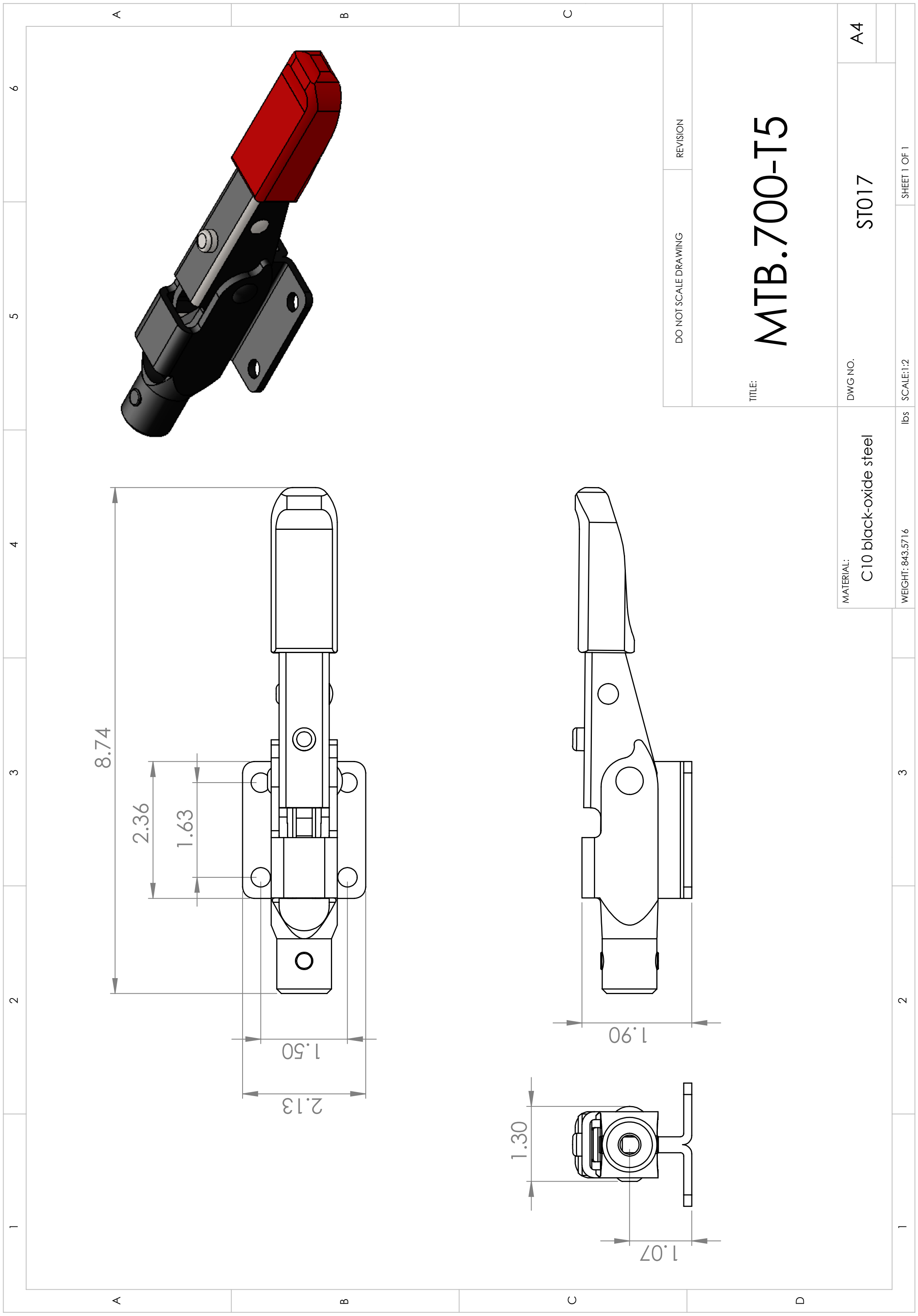
DO NOT SCALE DRAWING
REVISION
TITLE:
MTB.700-T5
DWG NO.
ST017
A4
SCALE:1:2
SHEET 1 OF 1
MATERIAL:
C10 black-oxide steel
WEIGHT: 843.5716
lbs
8.74
2.36
1.63
1.50
2.13
1.90
1.30
1.07

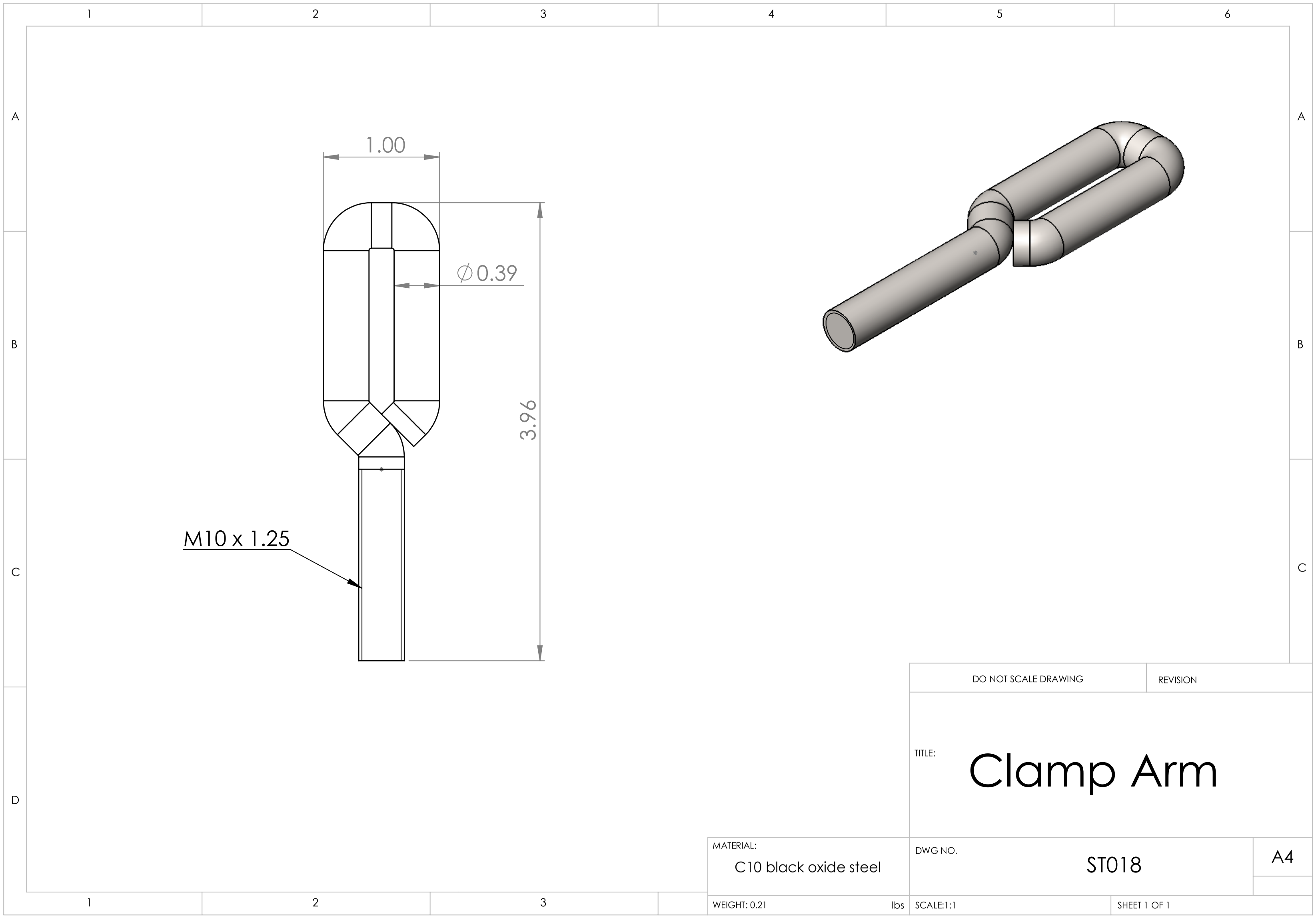

DO NOT SCALE DRAWING
REVISION
TITLE:
Clamp Arm
MATERIAL:
C10 black oxide steel
DWG NO.
ST018
A4
WEIGHT: 0.21 lbs
SCALE:1:1
SHEET 1 OF 1

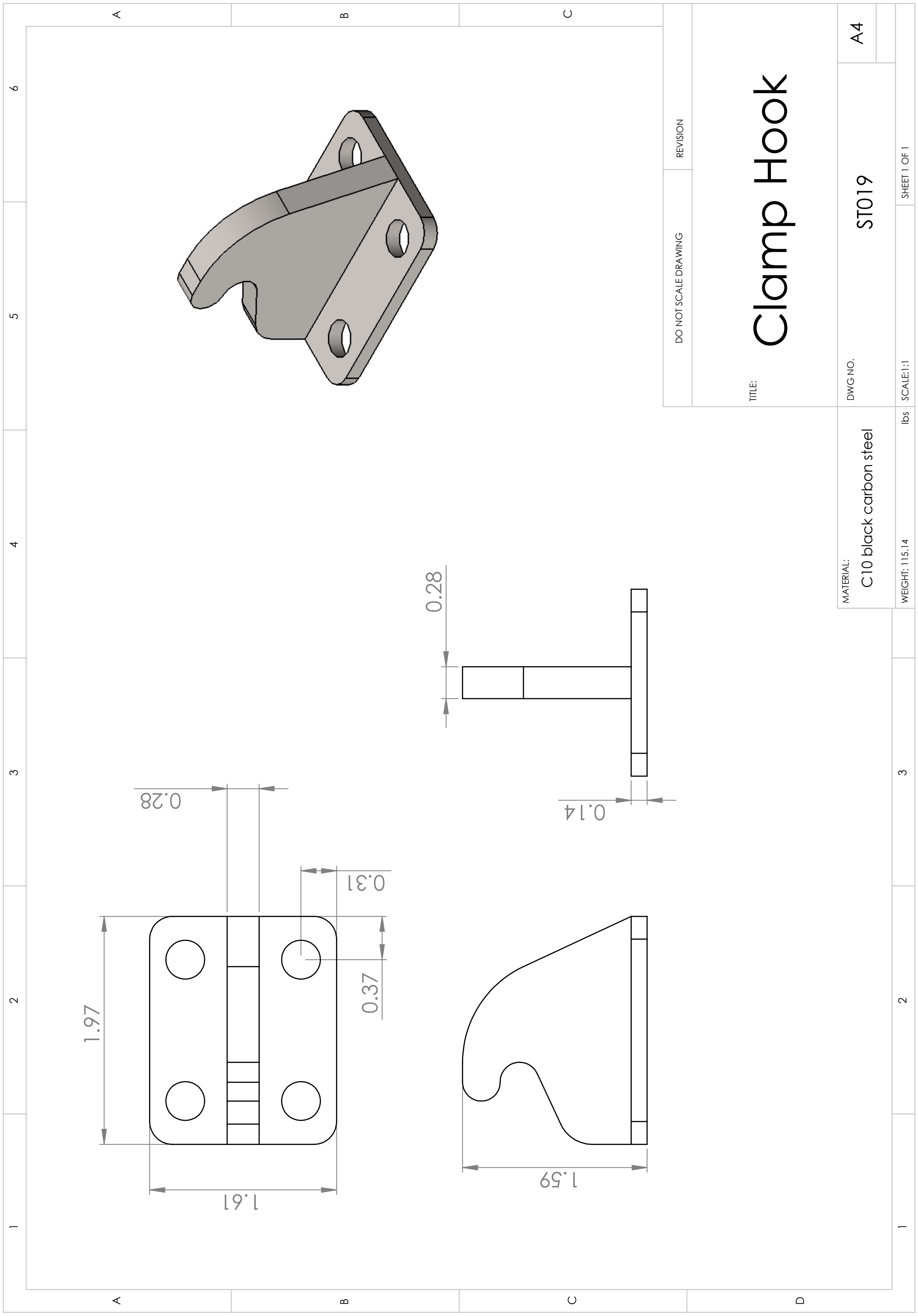
Clamp Hook
TITLE:
DWG NO.
ST019
A4
REVISION
DO NOT SCALE DRAWING
SCALE:1:1
SHEET 1 OF 1
MATERIAL:
C10 black carbon steel
WEIGHT: 115.14
lbs
1.97
1.61
0.37
0.31
0.28
0.28
0.14
1.59
A
B
C
D
1
2
3
4
5
6

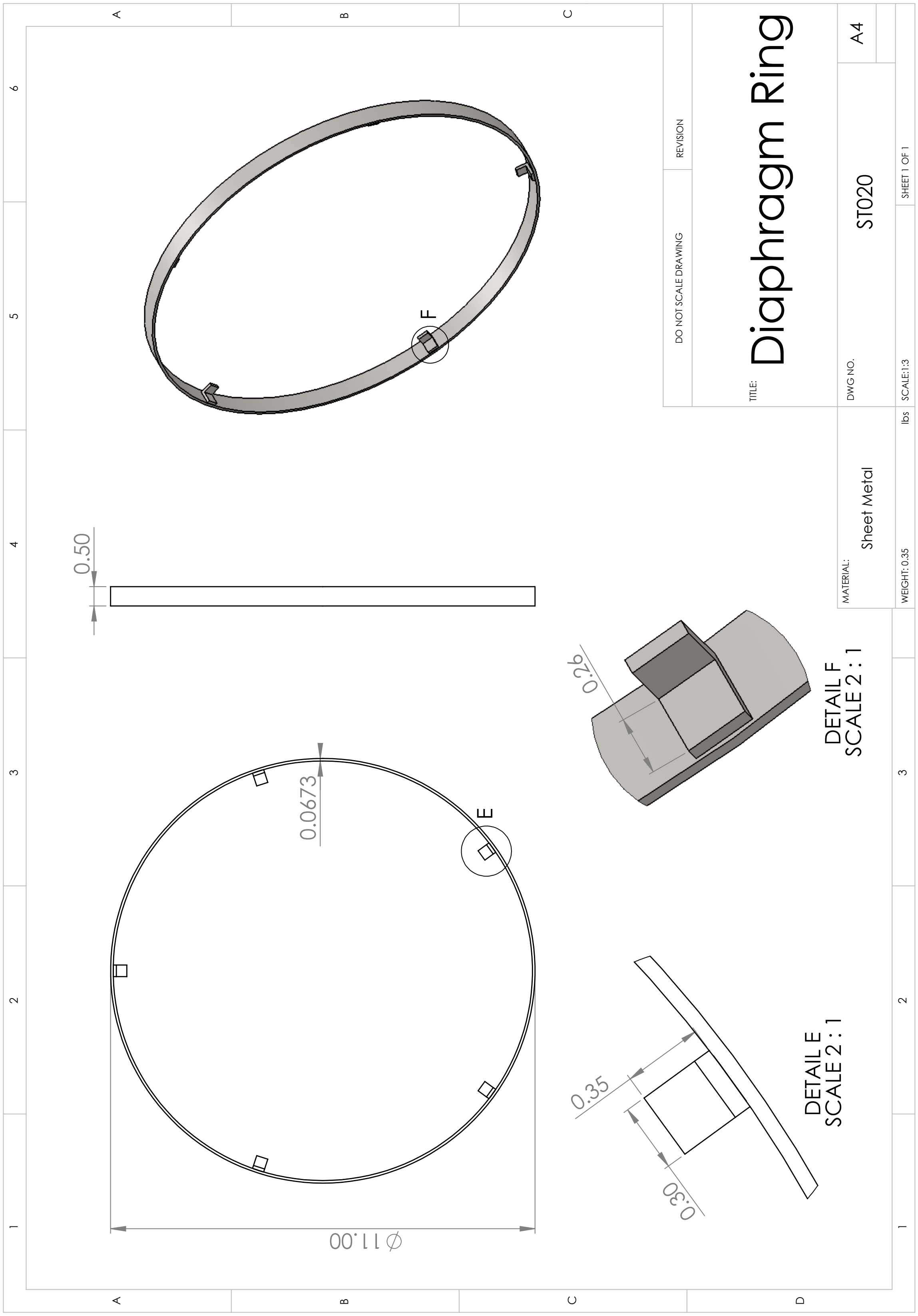
Diaphragm Ring
TITLE:
DO NOT SCALE DRAWING
REVISION
DWG NO.
ST020
A4
SCALE:1:3
SHEET 1 OF 1
MATERIAL:
Sheet Metal
WEIGHT: 0.35
lbs
F
0.50
0.0673
E
⌀11.00
0.26
DETAIL F
SCALE 2 : 1
0.35
0.30
DETAIL E
SCALE 2 : 1
A
B
C
D
1
2
3
4
5
6

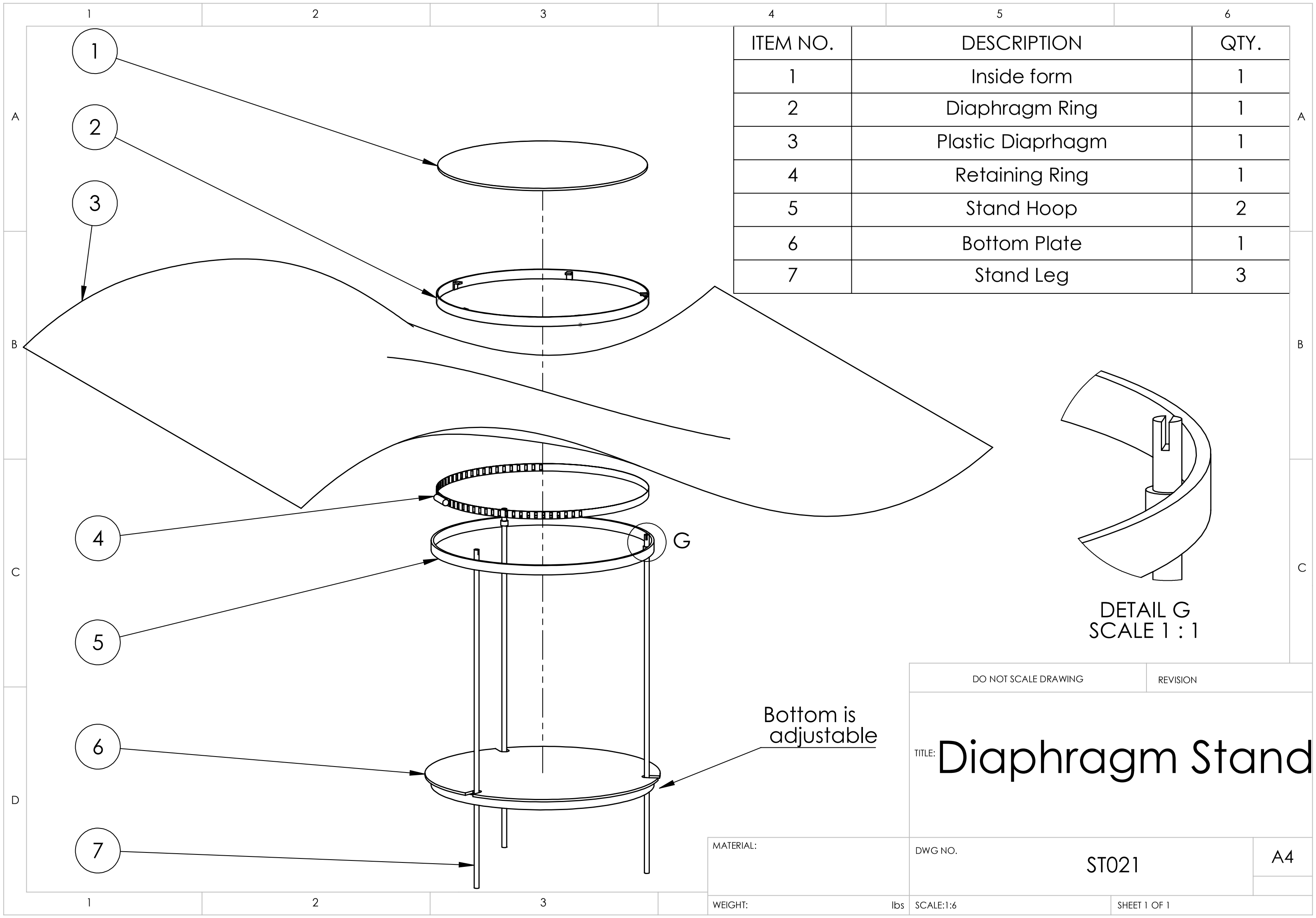

ITEM NO.	DESCRIPTION	QTY.
1	Inside form	1
2	Diaphragm Ring	1
3	Plastic Diaprhagm	1
4	Retaining Ring	1
5	Stand Hoop	2
6	Bottom Plate	1
7	Stand Leg	3

DO NOT SCALE DRAWING
REVISION
TITLE: Diaphragm Stand
MATERIAL:
DWG NO. ST021
A4
WEIGHT: lbs
SCALE:1:6
SHEET 1 OF 1

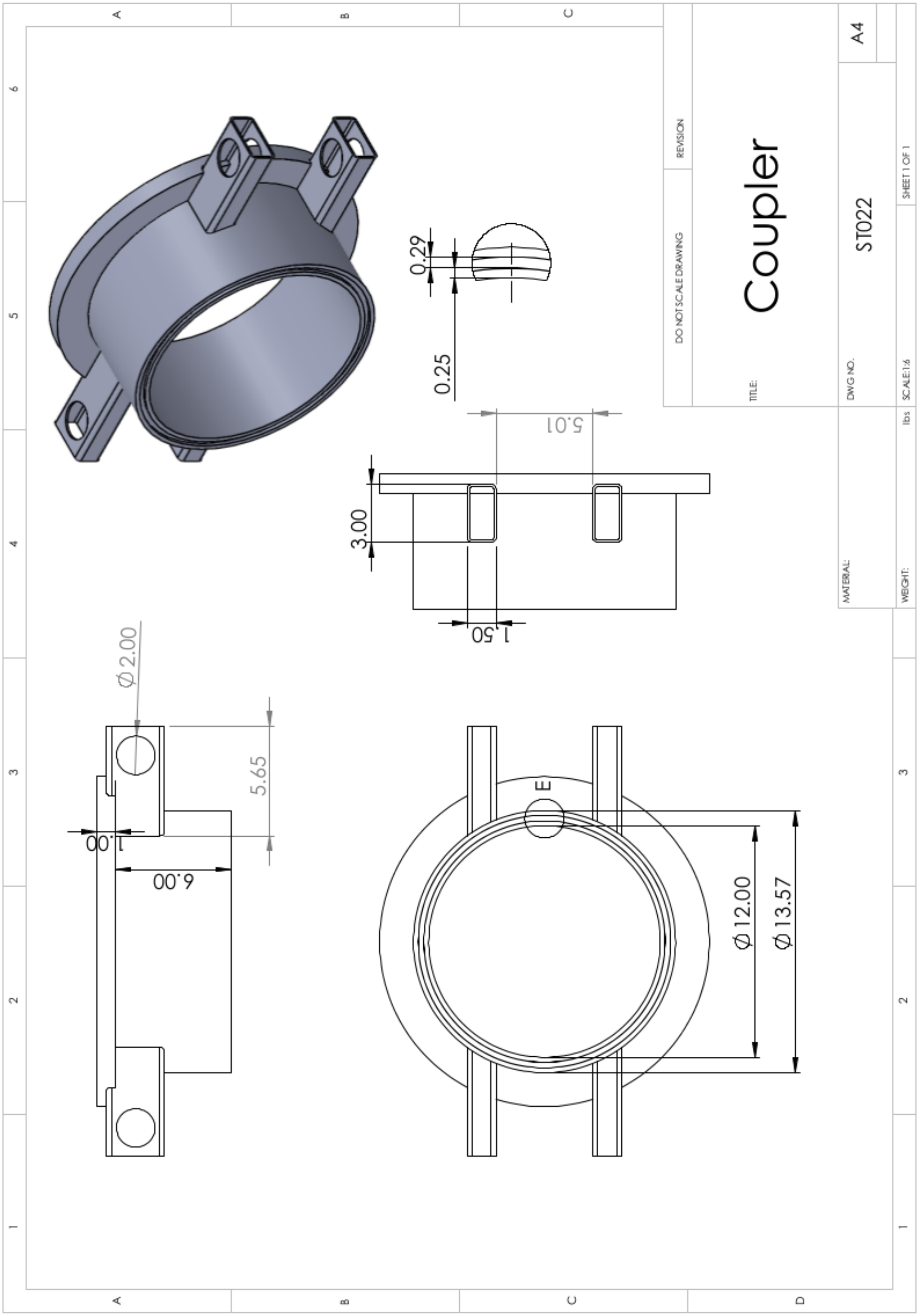
Coupler
ST022
TITLE:
DWG NO.
DO NOT SCALE DRAWING
REVISION
SCALE:1:6
SHEET 1 OF 1
A4
MATERIAL:
WEIGHT:
lbs
0.29
0.25
5.01
3.00
1.50
Ø2.00
5.65
1.00
6.00
Ø12.00
Ø13.57
E
A
B
C
D
1
2
3
4
5
6

Appendix F

Experimental Results - Pressure sensor profiles

Below are the pressure profiles recorded at each sensor location for every test. Note that during some tests, due to a software malfunction the profile of sensor #4 was not recorded.

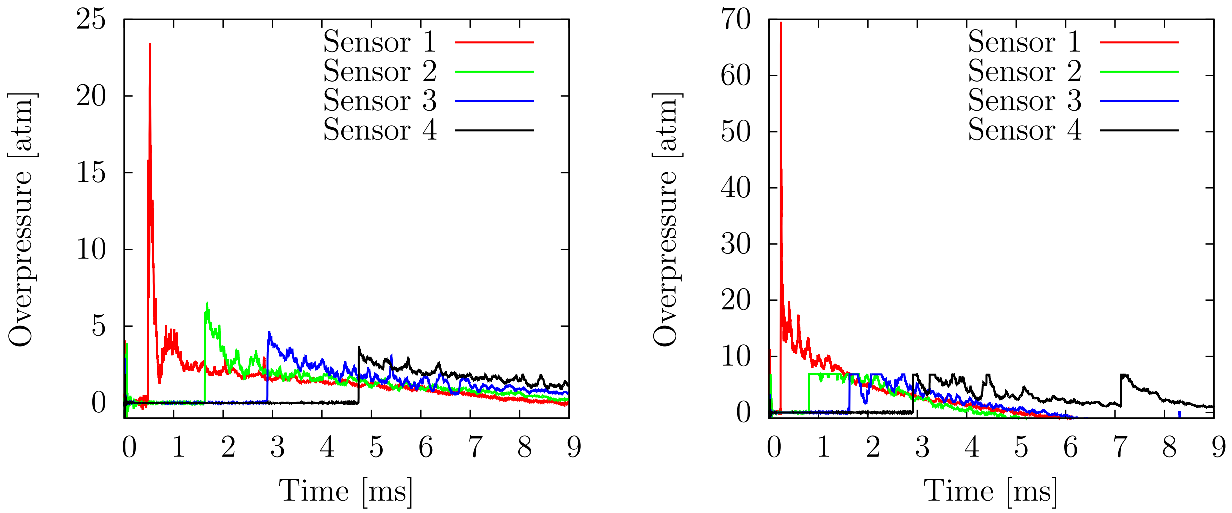

(a) Test 5 - 20% fill.

(b) Test 9 - 20% fill.

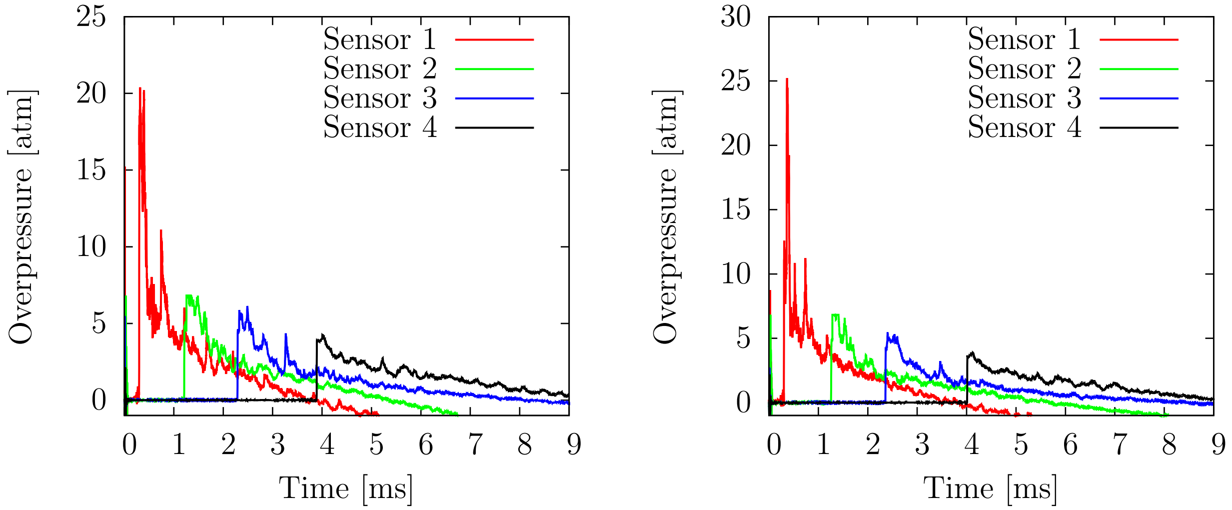

(c) Test 7 - 15% fill.

(d) Test 6 - 15% fill.

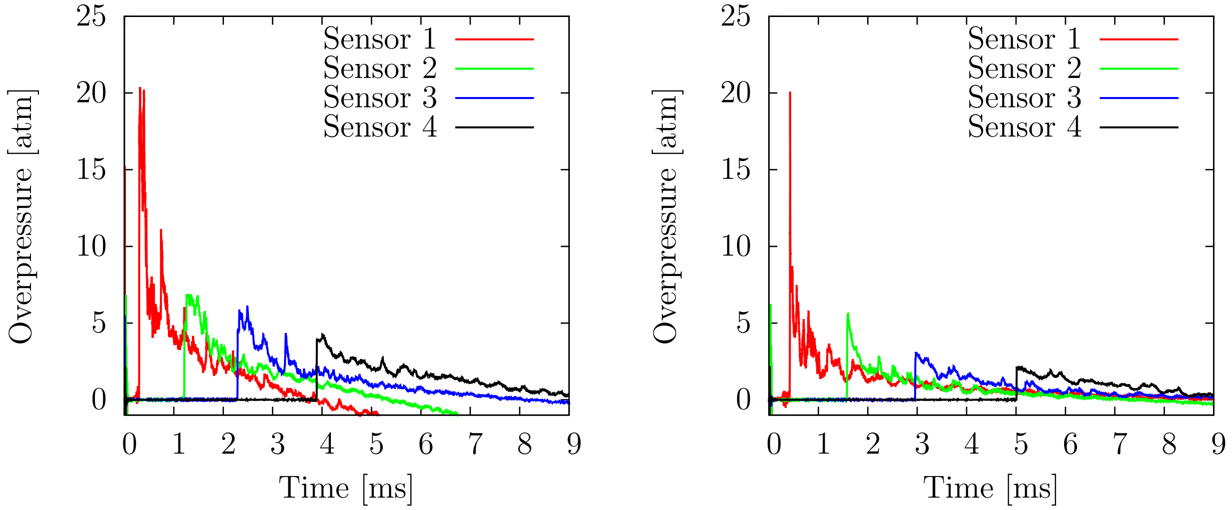

(e) Test 1 - 10% fill.

(f) Test 4 - 6% fill.

Figure F.1: Experimental Results. Pressure profiles recorded at pressure sensor locations.

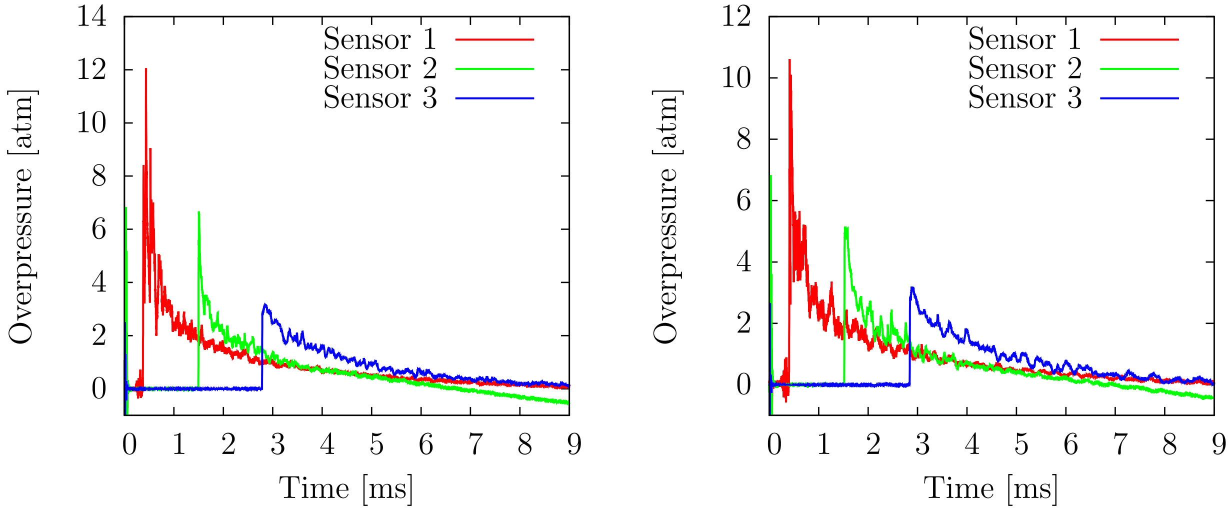

(a) Test 2 - 5% fill.

(b) Test 3 - 5% fill.

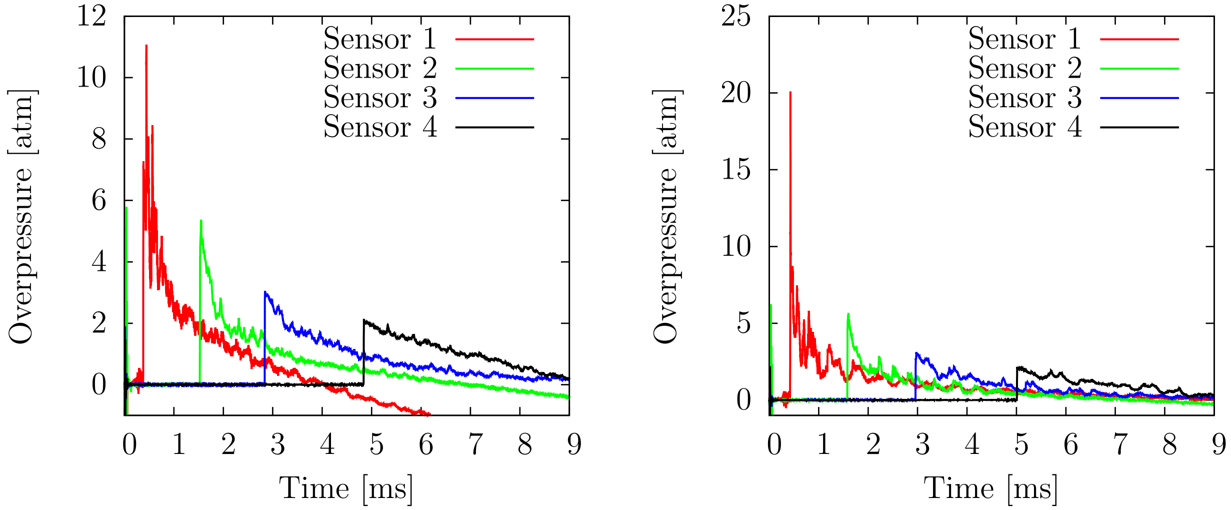

(c) Test 8 - 5% fill.

(d) Test 4 - 5.9% fill.

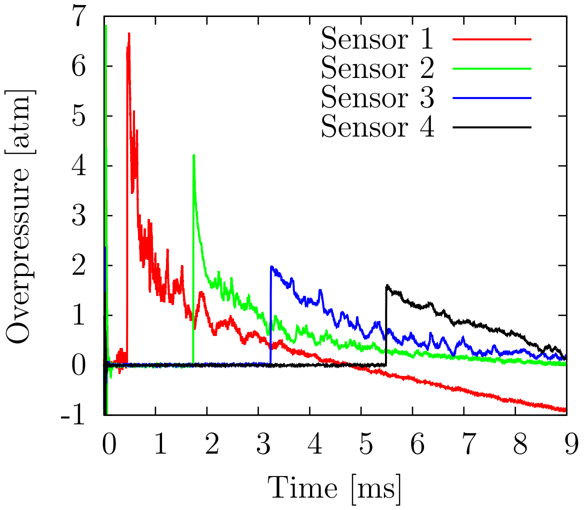

(e) Test 10 - 4% fill.

Figure F.2: Experimental Results. Pressure profiles Recorded at pressure sensor locations. (Continued.)

References

[1] J. M. Dewey, “The air velocity in blast waves from t.n.t. explosions,” *Proc. R. Soc. Lond. A*, vol. 279, no. 1378, pp. 366–385, 1964.

[2] D. V. Ritzel, S. A. Parks, J. Roseveare, G. Rude, and T. W. Sawyer, “Experimental blast simulation for injury studies,” in *Proceedings of RTO-MP-HFM-207.*, (Halifax, NB.), pp. 11–1–11–20, 2011.

[3] F. G. Friedlander, “The diffraction of sound pulses. i. Diffraction by a semi-infinite plane,” *Proc. R. Soc. Lond. A*, vol. 186, no. 1006, pp. 322–344, 1946.

[4] J. M. Dewey, “The shape of the blast wave: Studies of the friedlander equation,” in *Proceedings of the 20th Military Aspects of Blast and Shock.*, (Oslow, Norway), 2008.

[5] L. Houas, L. Biamino, C. Mariani, O. Igra, G. Jourdan, and A. Massol, “The effects that changes in the diaphragm aperture have on the resulting shock tube flow,” *Shock Waves*, vol. 22, no. 4, pp. 287–293, 2012.

[6] S. Golovastov and V. Bocharnikov, “The influence of diaphragm rupture rate on spontaneous self-ignition of pressurized hydrogen: Experimental investigation,” *International Journal of Hydrogen Energy*, vol. 37, no. 14, pp. 10956–10962, 2012.

[7] P. A. Thompson, *Compressible Fluid Dynamics.* McGraw-Hill, 1972.

[8] H. Celander, C. J. Clemedson, U. A. Ericsson, and H. I. Hultman, “The use of a compressed air operated shock tube for physiological blast research,” *Acta Physiologica Scandinavica*, vol. 33, no. 1, pp. 6–13, 1955.

[9] D. R. Richmond, R. V. Taborelli, F. Sherping, M. B. Wetherbe, R. T. Sanchez, V. C. Goldizen, and C. S. White, “Shock tube studies of the effects of sharp-rising, long-duration overpressures on biological systems,” tech. rep., Lovelace Foundation for Medical Education and Research, 1959.

[10] D. R. Richmond, V. R. Clare, V. C. Goldizen, D. E. Pratt, R. T. Sanchez, and C. S. White, "A shock tube utilized to produce sharprising overpressures of 400 milliseconds duration and its employment in biomedical experimentation," tech. rep., Lovelace Foundation, United States Defense Atomic Support Agency, 1961.

[11] N. M. Elsayed, "Toxicology of blast overpressure," *Toxicology*, vol. 121, no. 1, pp. 1–15, 1997.

[12] A. Holmberg, *Development and Characterization of Shock Tubes For Laboratory Scale Blast Wave Simulation.* phdthesis, University of Nebraska-Lincoln, 2010.

[13] N. Kleinschmit, *A Shock Tube Technique for Blast Wave Simulation and Studies of Flow Structure Interaction in Shock Tube Blast Experiments.* Ph.d. thesis, University of Nebraska-Lincoln, 2011.

[14] B. Zhang and C. Bai, "Critical energy of direct detonation initiation in gaseous fuel oxygen mixtures," *Safety Science*, vol. 53, pp. 153–159, 2013.

[15] T. Obara, T. Kobayashi, and S. Ohyagi, "Mechanism of deflagration-to-detonation transitions above repeated obstacles," *Shock Waves*, vol. 22, no. 6, pp. 627–639, 2012.

[16] C. Law, *Combustion Physics.* Cambridge University Press, 2006.

[17] B. H. K. Lee, "Detonation-driven shocks in a shock tube.," *AIAA Journal*, vol. 5, no. 4, pp. 791–792, 1967.

[18] H. R. Yu, B. Esser, M. Lenartz, and H. Grnig, "Gaseous detonation driver for a shock tunnel," *Shock Waves*, vol. 2, no. 4, pp. 245–254, 1992.

[19] W. Zhao, Z. Jiang, T. Saito, J. M. Lin, H. R. Yu, and K. Takayama, "Performance of the detonation driven shock tunnel," in *Shock Waves* (P. Z. Jiang, ed.), pp. 313–318, Springer Berlin Heidelberg, 2005.

[20] J. Li, H. Chen, and H. Yu, "A chemical shock tube driven by detonation," *Shock Waves*, vol. 22, no. 4, pp. 351–362, 2012.

[21] K. Bhaskaran and P. Roth, "The shock tube as wave reactor for kinetic studies and material systems," *Progress in Energy and Combustion Science*, vol. 28, no. 2, pp. 151–192, 2002.

[22] S. Guzik, P. Harris, and A. D. Champlain, "An investigation of pulse detonation engine configurations using the method of characteristics," in *38th AIAA/ASME/SAE/ASEE Joint Propulsion Conference and Exhibit*, American Institute of Aeronautics and Astronautics, 2002.

[23] Q. Zhang, C. Yan, W. Fan, and Q. Li, “Experimental investigation of effect of partial filling on the impulse of pulse detonation engine,” *Chinese Science Bulletin*, vol. 52, no. 20, pp. 2859–2865, 2007.

[24] S. Ohyagi, T. Yoshihashi, and Y. Harigaya, “A study on planar blast waves initiated by gaseous detonations. i - estimation of initiation energy,” *Japan Society for Aeronautical and Space Sciences*, vol. 33, pp. 649–657, 1985.

[25] P. A. Thibault, J. E. Shepherd, W. B. Benedick, and D. V. Ritzel, “Blast waves generated by planar detonations,” *Proc. 16th Int. Symp. Shock Tubes and Waves*, pp. 765–771, 1987.

[26] D. V. Ritzel and Dyn-Fx Consulting Limited, “Upgrade of the DRDC suffield blast tube facility,” tech. rep., Defence Research and Development Canada, 2007.

[27] S. Gordon and B. J. McBride, “Computer program for calculation of complex chemical equilibrium compositions and applications,” Tech. Rep. 1311, NASA, 1994.

[28] J. J. Quirk, “A parallel adaptive grid algorithm for computational shock hydrodynamics.,” 1991.

[29] I. Sochet, “Critical tube diameter for detonation transmission and critical initiation energy of spherical detonation,” *Shock Waves*, vol. 9, no. 2, pp. 113–123, 1999.

[30] S. Kato, S. Hashimoto, A. Uemichi, J. Kasahara, and A. Matsuo, “Propagation characteristics of shock waves driven by gaseous detonation waves,” *Shock Waves*, vol. 20, no. 6, pp. 479–489, 2010.

[31] G. S. Settles, *Schlieren and Shadowgraph Techniques: Visualizing Phenomena in Transparent Media.* Springer, 2001.

[32] O. Igra, G. Ben-Dor, T. Elperin, and A. Lifshitz, *Handbook of Shock Waves.* Academic Press, 2001.

[33] J. E. Shepherd, A. Teodorczyk, R. Knystautas, and J. H. S. Lee, “Shock waves produced by reflected detonations,” in *Proceedings of the 12th International Colloquium on Dynamics of Explosions and Reactive Systems*, vol. 1, (Ann Arbor, MI.), pp. 244–264, 1991.

[34] H. Matsui and J. H. Lee, “On the measure of the relative detonation hazards of gaseous fuel-oxygen and air mixtures,” *Symposium (International) on Combustion*, vol. 17, no. 1, pp. 1269–1280, 1979.

[35] R. G. Budynas, J. K. Nisbett, and J. E. Shigley, *Shigley’s mechanical engineering design.* McGraw-Hill, 2008.

[36] E. Avallone, T. Baumeister, and A. Sadegh, *Marks’ Standard Handbook for Mechanical Engineers.* McGraw Hill Professional, 2006.